

NORTHWESTERN UNIVERSITY

Material Interfaces Inspired by Catch Bond Adhesins

A DISSERTATION

SUBMITTED TO THE GRADUATE SCHOOL
IN PARTIAL FULFILMENT OF THE REQUIREMENTS

for the degree

DOCTOR OF PHILOSOPHY

Field of Mechanical Engineering

By

Kerim C. Dansuk

EVANSTON, ILLINOIS

September 2021

ABSTRACT

Over the last few years, there has been a transition away from traditional engineering materials to new advanced materials that exhibit complex architectures with improved mechanical properties. Most of the inspiration for these new materials comes from nature, where organisms have evolved an immense variety of macro and nanoscale shapes and structures with clever mechanisms. Adhesion proteins are particularly inspiring for novel materials because they exhibit conformational dynamics that enables them to form special non-covalent interactions called ‘catch bonds’ with their ligand, where dissociation lifetime of ligand-protein complexes is enhanced by mechanical force. Intuition suggests that application of a tensile force on a chemical bond should tend to shorten the bond’s lifetime, making it more likely to break, but catch bonds defy this notion. If implemented in material systems, catch bonds are predicted to address trade-offs between strength and reconfiguration, two diametric material properties that are primarily governed by the strength of intermolecular interactions. One specific approach to developing this bioinspired material is biomimicry, replicating what nature does well in terms of structure, however; to date, the physical principles underlying catch bond phenomena have remained disputed among scientists, hampering efforts to make synthetic catch bonds. This work is a multifaceted approach combining molecular simulations and adhesion theory to establish strategies for designing material interfaces that incorporates catch bond features.

A better understanding of catch bond physics would enable synthetic materials systems with catch bond linkages; hence, we begin with investigating chaperone-usher (CU) pilus—a bacterial adhesive protein with catch bond properties. By outlining adhesin properties determined by previous experimental investigations, we modeled the protein and systematically vary its catch

bond parameters to determine key adhesion properties. Based on these properties, we proposed design guidelines for reproducing the catch bond phenomenon in synthetic systems and created a tweezer-shaped mechanical design that mimicked protein ligand interaction and exhibited catch bond behavior reliably and predictably under thermal excitations. After demonstrating the success of our guidelines, we adopted two strategies to implement catch bonds in nanocomposite systems. First, by introducing allosteric pathways, we designed X-shaped nanoparticle that can change shape and transition to a stronger bond state in presence of tensile force. Second, by grafting tethers with tunable lengths to the surface of nanoparticles, we created an interface with two failure modes: one where the load is shared among the tethers and the other where it is not. Both strategies present man-made alternatives to biological catch bond mechanisms and provides insight into how interfaces can be engineered to create nanoparticle networks with force-enhanced linkers.

All-together these studies demonstrate that catch bond functionality can be achieved using simple molecular mechanisms and provides design rules for making catch bond nanoparticles and linkages, which paves the way for engendering emergent force-tunable interfacial kinetics in synthetic materials.

Thesis Advisor:

Dr. Sinan Keten

Department of Civil and Environmental Engineering and Department of Mechanical Engineering

Final Examination Committee:

Dr. Sinan Keten (Chair)

Dr. Horacio Espinosa

Dr. Oluwaseyi Balogun

ACKNOWLEDGEMENTS

I would first like to thank my advisor, Professor Sinan Keten, for his continued support and guidance throughout the entirety of my graduate research. He will always inspire me with his fantastic mentorship and seemingly undying commitment to research. He introduced me to the world of computational modeling, and it has been anything but monotonous 5 years since then.

Next, I would like to acknowledge the support from ONR Director of Research Early Career Award which funded my PhD.

I have been incredibly lucky to be part of an outstanding research lab. Hence, I would like to thank my group members who made the PhD journey an enjoyable experience and were always there to aid me in my research and life. I am particularly grateful for meeting Nitin K. Hansoge, Andrea Giuntoli and Martha Dunbar, who were not just helpful colleagues, but also willing victims of my sense of humor.

Finally, I would like to acknowledge the love and support that has been provided by my parents, Tülay & Ramazan Dansuk, throughout my entire life but especially through graduate school. They have continued to encourage me to go forward in life and have made sacrifices along the way to get me to this point. I just wouldn't be where I am today without their support.

TABLE OF CONTENTS

Chapter 1 – Introduction	9
1.1 Catch bond proteins and their importance	10
1.2 Recent developments and shortcomings in the field of Catch bond systems	12
1.3 Thesis outline	14
Chapter 2 – Computational Method	17
2.1 Markov chain Monte Carlo (MCMC)	17
2.2 Molecular dynamics (MD)	18
2.2.1. Langevin dynamics	22
2.3 Steered molecular dynamics (SMD)	23
Chapter 3 - Investigating the viability of catch bonds as a nanoparticle interface	25
3.1 Mechanical properties of Chaperon-Usher Pili	25
3.2 Simulation setup	28
3.2.1 Catch bond modelling	28
3.2.2 Pilus modelling	31
3.3 Pilus elongation simulations	32
3.4 Conclusion	40
Chapter 4 - Creating simple molecular systems that exhibits catch bond behavior	43
4.1 Key catch bond features	43
4.2 Designing the tweezer with catch bond behavior	46
4.3 Tweezer Lifetime Curves	48
4.4 Energy Landscape Design	53
4.5 Simulation Setup	58
4.6 Catch bond behavior	59
4.7 Conclusion	62

Chapter 5 - Designing nanoparticles with adhesin-inspired interfaces	65
5.1 X-shaped particle design	65
5.2 Simulation parameters	71
5.3 Binding energy landscapes for catch bond behavior	72
5.4 Force history dependence of the system	79
5.5 Self-assembly of nanoparticles	81
5.6 Lifetime scaling of self-assembled fibers	82
5.7 Conclusion	83
Chapter 6 - Establishing catch bond designs through cooperativity of tether links	85
6.1 Two tether geometry	86
6.2 Simulation setup	92
6.3 Catch bond behavior	93
6.4 Estimating catch bond kinetics by an analytical model	95
6.5 Conclusion	99
Chapter 7 – Conclusion	101
7.1 Future look	102
References	105

LIST OF FIGURES

Figure 1-1 Nonbonded interaction lifetime curves	10
Figure 1-2 Schematics of grafted nanoparticles (PGNs) network	12
Figure 1-3 Examples of catch bond models from the literature	14
Figure 2-1 Graph of a Morse potential function	21
Figure 3-1 Notable features of bacterial pili	26
Figure 3-2 Energy landscape representation of a nonbonded interaction	29
Figure 3-3 Slip and catch bond models	29
Figure 3-4 Constant velocity elongation simulations of single pilus with an adhesive tip	34
Figure 3-5 Effects of variation of catch bond rate parameters on the toughness of a single pilus as a function of pulling velocity	37
Figure 3-6 Effects of variation of shaft parameters on the toughness of a single pilus as a function of pulling velocity	39
Figure 4-1 Catch bond models	45
Figure 4-2 Rigid member representation of tweezer geometry in open conformation	47
Figure 4-3 Rates of tweezer/ligand events	50
Figure 4-4 Mean lifetime versus force curves of low affinity unbinding $\langle\tau\rangle_{LA}$ and forward transition $\langle\tau\rangle_{S+}$ events	53
Figure 4-5 Stiffness representation of tweezer system	56
Figure 4-6 Mean lifetime $\langle\tau\rangle$ versus force f curve for tweezer-ligand complex	60
Figure 4-7 Effects of key parameters on mean lifetime $\langle\tau\rangle$ versus force f curve of tweezer-ligand complex	62
Figure 5-1 Schematics of X-shaped nanoparticles	67
Figure 5-2 X-shaped nanoparticle geometry and its dimensions	70
Figure 5-3 Force dependence of the fraction of trials for the dimer to dissociate in the LA state and dimer to transition from the LA to the HA state	74
Figure 5-4 Effects of secondary interaction energy well depth ($D_{o,SBS}$) on mean lifetime $\langle\tau\rangle$ versus force f curve of a nanoparticle dimer	75

Figure 5-5 X-shaped nanoparticles form a biphasic system with two unbinding pathways	78
Figure 5-6 Break force histograms for X-shaped nanoparticle dimer under constant loading rate	80
Figure 5-7 Mean lifetime $\langle \tau \rangle$ versus force f curves for self-assembled fibers at varying degrees of polymerization	81
Figure 6-1 Loop motif in biological and biomimetic systems	87
Figure 6-2 Two tether system	88
Figure 6-3 Force exposure of the individual tethers in sequential and coordinated failure scenarios	90
Figure 6-4 Energy landscape and lifetime graphs for the tether system	92
Figure 6-5 Effects of interaction parameters on mean lifetime versus force f curve of two tether system	95
Figure 6-6 Force dependence of the fraction of trials for the looped tether adhesin breaking before the loop opening event	97
Figure 6-7 Analytical fit for tether lifetime data	98
Figure 7-1 Possible DNA origami design of the X-shaped nanoparticle	103

LIST OF TABLES

Table 3-1 Two-state model parameters	30
Table 3-2 Pilus shaft model parameters	32
Table 4-1 Tweezer Dimensions	48
Table 4-2 Tweezer interaction parameters	57
Table 5-1 Nanoparticle Dimensions	71
Table 5-2 Nanoparticle interaction parameters	74
Table 6-1 Tether interaction parameters	91
Table 6-2 Dissociation parameters from the analytical fit	99

Chapter 1 -Introduction

A major area of current materials research is the investigation of new advanced materials that improve upon the performance and characteristics of traditional engineering materials. One such material, polymer nanocomposites, is a rapidly evolving area of material science research due to the ability of these materials partially overcome strength-toughness trade-offs^{1,2}. It is well known that the performance of nanocomposites depends not only on their constituents but also on how these constituents interact at internal interfaces³⁻⁵. Therefore, there is a push for development of new strategies for altering improving interfacial properties. One of the strategies is to design bioinspired materials by replicating what nature does well in terms of structure. Although different in function than the nanocomposite materials, adhesion and sensing proteins that attach to biotic and abiotic surfaces exhibit intriguing properties that could improve interface properties of nanocomposites⁶. This work focuses on a notable promising feature of proteins, formation special non-covalent interactions called ‘catch bonds’ with their ligand, where dissociation lifetime of ligand-protein complexes is enhanced by mechanical force⁷. While catch bonds have been shown theoretically and computationally to enhance mechanical properties of network nanocomposites⁸⁻¹⁰, integration of catch bonds in materials has not yet been realized as structures with tunable catch bond like characteristics haven’t yet been fabricated.

In this regard, in first part of my Ph.D., I focused on investigating proteins with catch bond properties to determine key adhesion properties. Based on these properties, we proposed design guidelines for reproducing the catch bond phenomenon in synthetic systems. The second part of the dissertation focuses on demonstrating catch bond functionality of simple nanoparticle/interface systems that are created based on our design guidelines. In this introductory chapter, we focus on

describing the properties catch bond proteins, which make them attractive candidates for biomimetic materials, as well as recent developments and shortcomings in the field of catch bond research. We conclude the chapter with an overview of the entire dissertation and how we established design concepts for nanocomposites by studying adhesins.

1.1 Catch bond proteins and their importance

Since early applications of kinetic theory to fracture and adhesion, and subsequent experiments in biological and man-made materials, it has been long known that the lifetime of typical chemical interactions/bonds between of two bodies becomes exponentially shorter when a

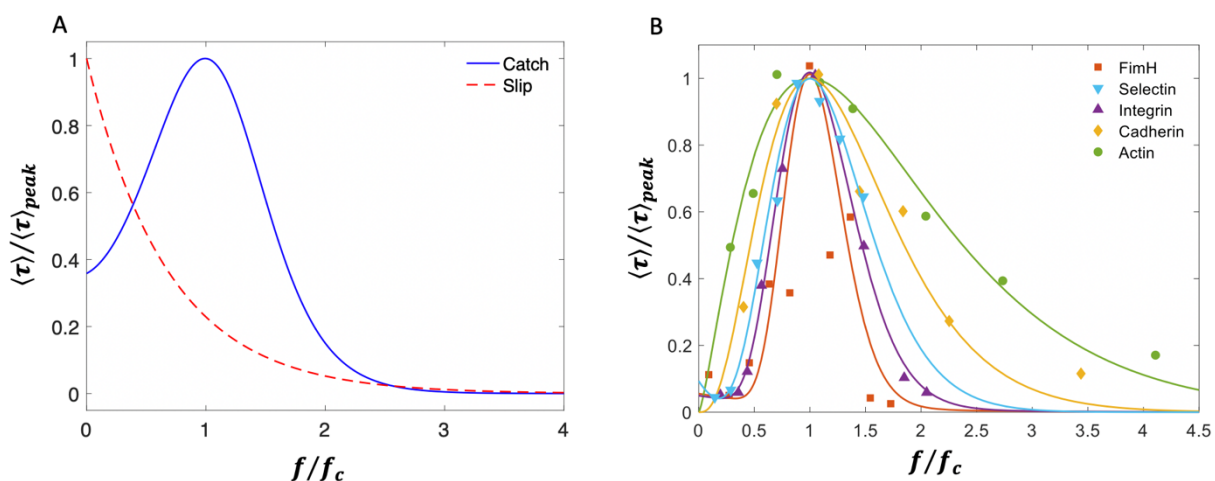


Figure 1-1 Nonbonded interaction lifetime curves A) Archetypal catch vs. slip bond lifetime curves, showing exponential decay (slip) vs. non-monotonic behavior (catch bond). B) Mean lifetime $\langle \tau \rangle$ versus force f curves of several catch bond proteins. Symbols are the data from the force spectroscopy experiments and curves are generated with the fitting function $\langle \tau \rangle(f) = cf^a \exp[-f/b] + d \exp[-f/e]$. $\langle \tau \rangle$ and f are normalized with peak lifetimes ($\langle \tau \rangle_{peak} = 2.51, 0.22, 11.58, 1.3689474, 0.032$ s) and the corresponding critical forces ($f_c = 59.29, 44.49, 24.05, 10.20, 4.52$ pN). Sources of the data are ref. 11-16. The normalization factors and sources follow the legend order.

force is applied to separate the bodies. This type of interaction is referred as “slip bond” in the literature. In this section, we are going to look at various protein-ligand complexes that utilize catch bonds to defy this notion, i.e. they easily break at small forces but have longer lifetimes under larger forces, up to a certain force limit⁷. To date, several proteins including pilus adhesin FimH¹¹, P-selectin/L-selectin¹², integrin¹³, catenin¹⁴, actin¹⁵, and kinetochore¹⁶ have been demonstrated to exhibit catch bond behavior. The catch bond is characterized by a non-monotonic biphasic force versus lifetime curve where the lifetime peaks at a critical force f_c and decreases at larger forces, as shown in Fig. 1-1.

Because of their force-enhanced lifetimes, catch bonds provide practical dynamic features to cells that are often under varying flows/mechanical stresses. Under large stresses, catch bonds can mediate robust adhesion between extracellular matrices/cells and maintain integrity of interfaces. Conversely, under small stresses, catch bonds can easily dissociate and allow cell mobility.^{17,18} These dynamic features inherent to catch bonds have implications for bioinspired material design. As reversible interactions that become stronger with applied force, catch bonds can provide resistance to large mechanical stresses while allowing reconfiguration under small stresses in material systems.

1.2 Recent developments and shortcomings in the field of Catch bond systems

Majority of the catch bond studies had biophysical perspective, which aimed to reproduce or explain a range of biological behaviors. However, there still are works that investigate catch bonds from a material science¹⁹, chemistry perspective²⁰. In particular, catch bonds have been studied, theoretically and computationally^{9,10,21-23} to enhance the mechanical properties of nanoparticle networks in nanocomposites (Fig. 1-2). Certain non-biological molecules have been synthesized to mimic catch bond behavior.^{24,25} These molecules have covalent bonds that become stronger under larger mechanical stress, which can be classified as catch bond behavior without any

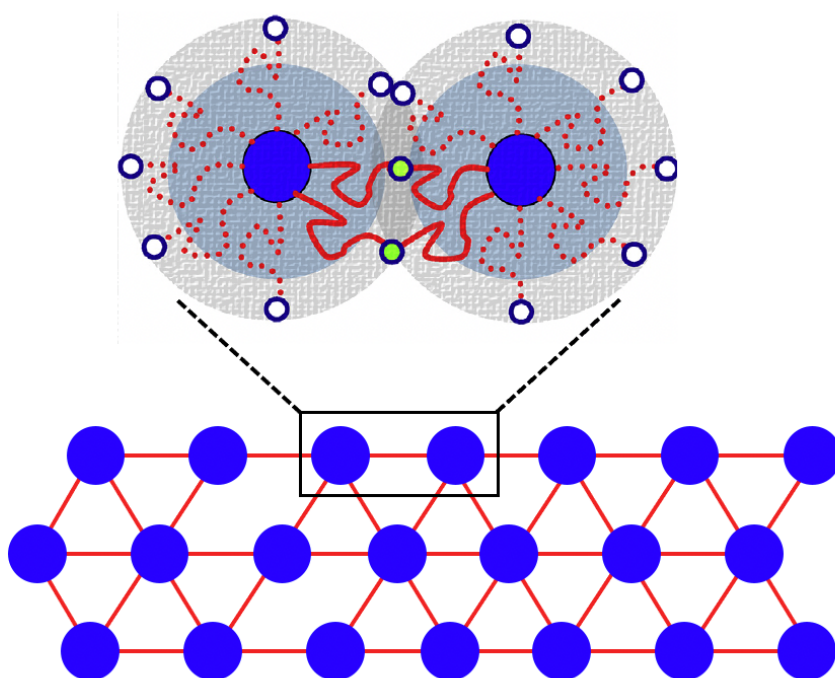


Figure 1-2 Schematics of polymer grafted nanoparticles (PGNs) network. Each PGN consists of solid nanoscopic core (blue) and a corona of chains (red) that are end-grafted to this core. The free ends of the grafted chains (green) are designed geometries with catch bond behavior. Iyer *et al.* perform simulations on PGN networks to show that compared to systems with slip bonds, systems with catch bond interactions have significantly higher toughness and strength.

reversibility. Despite these developments, integration of catch bonds in materials still remains a theoretical concept because synthetic molecules that fully reproduce catch bond characteristics and maintain reversibility haven't yet been fabricated. Challenges in synthesizing molecular systems that exhibit the complex 3D topology, allosteric behavior, and dynamic features seen in proteins also hamper further developments in this field.

Minimalistic design rules for catch bonds are difficult to extract directly from proteins because they are complex multifunctional macromolecules with many structural, chemical, and dynamic constraints. The progress of production of synthetic systems with catch bond like properties necessitates the development of models that capture structural changes in catch bond proteins due to mechanical forces, and how resulting structural changes alter the unbinding kinetics. So far, the catch bond research has led to the development of several theoretical models^{26,27} as shown in Figure 1-3. Phenomenological models, such as the two state model^{28,29} (Figure 1-3A) and the two path model^{30,31}, can accurately represent characteristics of a wide range of experimental data sets, but provide limited information on how one should create a structure and mechanism for catch bonds, which is crucial for the inverse problem of synthetic design. Complementary to these efforts, atomic level analysis of 3D protein crystal structures have elucidated the structural basis of allostery between the domains of the catch bond proteins (Figure 1-3B).^{32,33} However, the exact allosteric mechanisms are quite complex and subject to debate, which makes it challenging to recapitulate protein-based designs directly in polymeric systems. In addition to biophysical models, some early conceptual models³⁴⁻³⁹ combined mechanical principles with the structural knowledge of proteins to explain catch bonds, where higher affinity states could

be achieved by sliding rebinding events, or finger trap-like conformational changes (Figure 1-3C), as reviewed in Thomas *et al.*²⁶

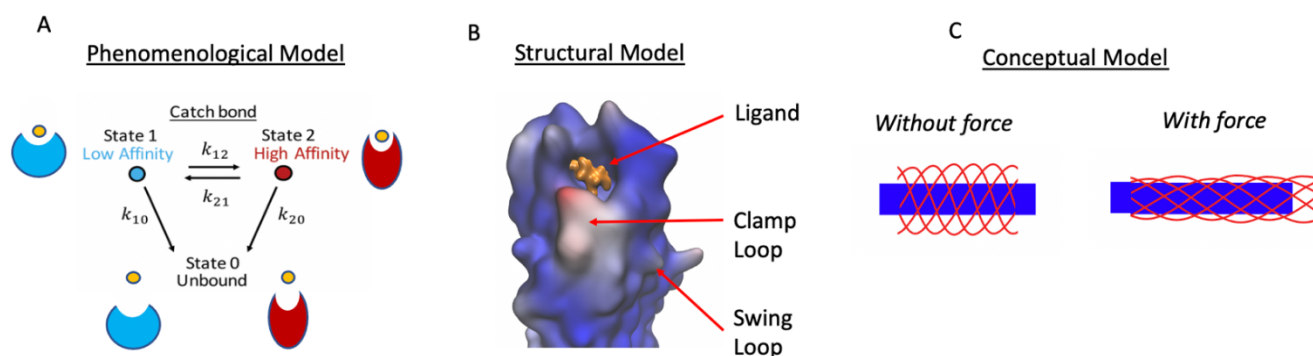


Figure 2-3 Examples of catch bond models from the literature A) Phenomenological model: Two state model. This model has four pathways that it can traverse before unbinding: the forward and reverse transitions between the two states, and unbinding from each of the two states. B) Structural model: The crystal structures of protein FimH. C) Conceptual model: Chinese finger trap. Mechanisms grip more strongly when a force is applied along the length of the system.

1.3 Thesis outline

To take catch bonds beyond the biological milieu, it is necessary to create simple thermomechanical systems that mimic the mechanisms underlying catch bond behavior. Therefore, this research has focused on creating simple design rules for creating catch bond linkages and demonstrated systems based on these rules exhibit catch bond behavior reliably and predictably. Before presenting our results, we summarize many of the simulation techniques used throughout this work in Chapter 2, including an overview of Markov Chain Monte Carlo (MCMC), molecular dynamics (MD) and steered molecular dynamics (SMD).

In the first study presented in Chapter 3, we have modeled the elongation of a catch bond adhesins, Chaperon Usher (CU) pilus and examined its toughness response. Using MCMC

simulations of single pilus elongation, we showed that catch bond adhesins act as a molecular seat belts that exhibit low toughness when pulled slowly and high toughness when pulled rapidly. Furthermore, we found that by systematically varying the catch bond parameters, the seat belt properties can be tuned. The molecular seat belt mechanism presented here provided insight into determining key adhesion properties.

Based on these properties, we proposed design guidelines for reproducing the catch bond phenomenon in synthetic systems and created a tweezer-shaped mechanical design that mimicked protein ligand interaction and exhibited catch bond behavior reliably and predictably under thermal excitations. In Chapter 4, we have demonstrated that a simple mechanical design based on a tweezer-like mechanism can exhibit catch bond characteristics under thermal excitations. The tweezer has a force-sensitive switch which controls the transition of the system to a high-ligand-affinity state with additional ligand-tweezer interactions. Applying kinetic theory to a two-mass-two-spring idealized model of the tweezer, we show that by tuning the shape of the switch and the ligand-tweezer interaction energy landscapes, we can achieve greater lifetimes at larger force levels. We validate our theory with molecular dynamics simulations and produce a characteristic lifetime curve reminiscent of catch bonds.

In Chapter 5, we establish a scissor-type X-shaped particle design for achieving intrinsic catch bonding ability with tunable force-enhanced lifetimes under thermal excitations. MD simulations are carried out to illustrate equilibrium self-assembly and force-enhanced bond lifetime of dimers and fibers facilitated by additional inter-particle interactions that form under tensile force.

Next, in Chapter 6, we present a molecular design that results in catch bonding interfaces between polymer grafted nanoparticles. Our design relies on two equal length polymer tethers that

connect the particles with adhesive interactions, where one tether has a compliant loop stabilized by weak bonds. Molecular dynamics simulations illustrate that making the fold opening kinetics more sensitive to force than the adhesin, simply by tuning its stiffness, results in a transition from sequential to coordinated failure of the adhesive polymer tethers under force.

The dissertation and main findings are summarized in Chapter 7 where we also provide some outlook to the future of synthetic catch bonds.

Chapter 2 - Computational Method

In this chapter, the general simulation techniques used to study biological and synthetic catch bond systems will be discussed. The first section will cover Markov chain Monte Carlo (MCMC) method and how we use it to determine the lifetimes of catch bond events. The second section provides an overview of molecular dynamics (MD) simulations and their theoretical basis. Lastly, we discuss a subset of MD simulations called steered molecular dynamics (SMD), which involve non-equilibrium force pulling simulations. While certain simulation parameters are included in this chapter (such as simulation time, system constraints, etc.), specific details can be found in the chapters for specific studies.

2.1 Markov chain Monte Carlo (MCMC)

Markov chain Monte Carlo is commonly used for obtaining a sequence of random samples from a probability distribution. In this work we used Metropolis algorithm^{40,41} that can draw samples from probability distribution $P(x)$, given that there is a well-defined function $f(x)$ that is proportional to density of P .

The steps of this Monte Carlo simulation can be outlined as follows:

1. Establish an initial configuration $f(x_t)$, where x_t is an arbitrary initial point.
2. Make a random trial change in the configuration, $f(x')$.
3. Calculate the acceptance ratio $\alpha = \frac{f(x')}{f(x_t)}$ which will be used to decide whether to accept or reject the change.
4. Generate a uniform random number $u \in [0,1]$.

5. If $u \leq \alpha$, then accept the candidate by setting $x_{t+1} = x'$, if $u > \alpha$, then reject the change and iterate for a new random trial change.

In short, the algorithm proceeds by randomly attempting to move about the sample space, sometimes accepting the moves and sometimes remaining in place.

It has been shown that at the limit of large statistics, rupture and formation events at nano/macro scale occur in a stochastic fashion due to the presence of thermal motion⁴²⁻⁴⁴. Therefore, transition/unbinding events have no specific lifetime, but rather follow a distribution of lifetimes. Monte Carlo simulation method is commonly used to describe these rupture and formation events^{29,45,46}, by performing iterative acceptance checks for a given probability distribution. In Chapter 3, we will investigate two protein unbinding and rebinding events, (i) elongation of P pili under force and (ii) catch bond behavior at its tip, using MCMC.

The adhesive proteins can be in different structural configurations (states). The transition probability to change the system from one state to another is given by the ratio of the probabilities to be in the two states. As it is explained in the MCMC outline, we can determine the acceptance of the transition by comparison of this probability and a random number. How these transition probabilities are calculated will be explained in Chapter 3.

2.2 Molecular dynamics (MD)

Our primary method of investigating bond kinetics of catch bond will be to use MD simulations. Molecular dynamics is a simulation of the physical movements of particles within a given system, where these particles can represent atoms, molecules, or coarse-grained entities, i.e. multiple atoms are grouped into a single particle. The main objective of MD is to simulate the progression of a system over time in terms of particle positions, velocities, and accelerations and

then use this information to accumulate information about the structural, thermodynamic, and mechanical properties of the system.

MD simulations are conducted by integrating Newton's equations of motion using numerical techniques and updating the positions and velocities of each particle. For a system of N particles, the equation of motion that must be solved is given by Eqn. 2-1

$$m_i \vec{a}_i = -\nabla U(r_1, r_2, \dots, t) + \vec{f}_i, \quad i = 1, 2, \dots, N \quad (2-1)$$

where m_i is the mass of particle i , \vec{a}_i is the acceleration vector of particle i , U is the interatomic potential between particles that is a function of all atom positions and time, and \vec{f}_i is any external force that is added to the system. By integrating these equations in time, the trajectory of the particles (i.e. their position and velocity) within the system can be traced and many properties can be extracted such as temperature, pressure, bond energy, etc. In our simulations, Verlet algorithm⁴⁷ is used to update atom positions and velocities over time. After particle accelerations using Eqn. 2.1, for a time step of δt , the updated positions and velocities are given by Eqn. 2-2 and 2-3, respectively.

$$\vec{r}(t + \delta t) = \vec{r}(t) + \delta t \vec{v}(t) + \frac{1}{2} \delta t^2 \vec{a}(t) \quad (2-2)$$

$$\vec{v}(t + \delta t) = \vec{v}(t) + \frac{1}{2} \delta t [\vec{a}(t) + \vec{a}(t + \delta t)] \quad (2-3)$$

These updated positions and velocities are determined by estimating the time derivatives of velocity and acceleration with a second-order Taylor series expansion around the point $t + \delta t$. Because a numerical technique is employed, an appropriate time step must be chosen to ensure conservation of energy and physically correct motions of particles within the system. MD

simulations in Chapters 4 to 6, 1 *femtosecond* time step is found to be sufficiently small to ensure energy conservation and lifetime accuracy.

As shown in Eqn 2-1, the forces acting on the atoms are calculated from derivative of the interatomic potential between particles $U(r)$. The interatomic potential between particles, i.e. force field is the sum of the individual contributions of interactions between atoms such as bonded potentials (bonds, angles dihedrals, impropers), non-bonded potentials (van der Waals, hydrogen bonds), charges and is given by Eqn. 2-4.

$$U = U_{non-bonded} + U_{Coulombic} + U_{bond} + U_{angle} + U_{dihedral} \quad (2-4)$$

The systems in this work on are simple structures with rigid and freely jointed components, thus we didn't need to utilize angle, dihedral and improper potentials, which are related to capturing the realistic angle bending, bond torsion, and out-of-plane bending angles. However, we defined bond and non-bonded potentials. In general, bond interactions between atoms are represented using harmonic potential

$$U_{bond} = \frac{1}{2}k(r_i - r_j)^2 \quad (2-5)$$

where k is the spring constant and r_i, r_j are the positions of the atoms.

In this work, majority of the non-bonded interactions such as protein ligand hydrogen bonds are represented by Morse potential (Fig. 2-1):

$$U(r)_{morse} = D_0(\exp[-2\alpha(r - \sigma)] - 2 \exp[-\alpha(r - \sigma)]). \quad (2-6)$$

Here, D_0 is the depth of the energy well, σ is the equilibrium bond distance and α is the parameter that controls the width of the well (the smaller α is, the broader the well).

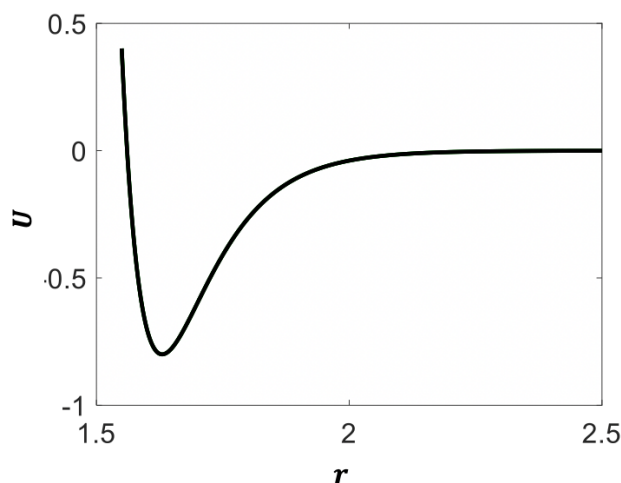


Figure 2-1 Graph of a Morse potential function

In addition to understanding numerical integration techniques and force fields, molecular dynamics simulations also require the use of a statistical ensemble that describes the possible microstates of a mechanical system⁴⁸. In these ensembles, a partition function is used to describe the probability of each specific microstate and is dictated by the quantities that are held fixed in simulation. Molecular ensembles of interest are the microcanonical ensemble (NVE), canonical ensemble (NVT), grand canonical ensemble (μ VT), and isothermal-isobaric ensemble (NPT). The abbreviations that follow the ensemble names indicate the quantities that are held fixed during simulation with N corresponding to the number of particles, V representing the system volume, T being the system temperature, μ being the chemical potential of the system, and P being the system pressure. NVT ensemble is used in our MD simulations, since constant N , V and T is desired for the unbinding analysis.

There are multiple readily available software packages for MD, including LAMMPS⁴⁹, NAMD⁵⁰ and GROMACS⁵¹ among numerous others. These packages offer wide flexibility to

simulate a number of different systems using a wide range of force fields. For our simulations, we chose to employ the LAMMPS molecular dynamics package, as we are not focusing a specific biotic or abiotic system that requires built in force fields, instead we build our systems from scratch where we need to vary the geometries and force field parameters. LAMMPS gives us the flexibility to simulate various geometries and use custom force fields.

2.2.1. Langevin dynamics

Nano/micro scale molecular system that we are investigating are not in a vacuum, but in a solvent. Solvent molecules significantly alter the dynamics of the system by causing frictional drag and random collisions associated with the thermal motions of the solvent molecules⁵². Langevin dynamics attempts to extend molecular dynamics to account for these effects^{53,54}. Langevin dynamics in MD mimics a group of particles which models an interaction with a background implicit solvent, where the total force on each atom i will have the form:

$$f_i = \sum_{ij, i \neq j} f_{ij}^C + f_{ij}^F + f_{ij}^R \quad (2.7)$$

f^C is the conservative force computed via the usual interparticle interactions, which are bonded and non-bonded interactions explained above. f^F is a frictional drag or viscous damping term proportional to the particle velocity v and given by

$$f_F = -\frac{m}{\gamma} v \quad (2.8)$$

where m is the mass of the particle and γ is the damping factor. f^R is a force due to solvent atoms at a temperature T randomly bumping into system particles. Based on fluctuation/dissipation theorem, magnitude of this force is proportional to $\sqrt{k_B T m / \gamma}$, where k_B is the Boltzmann constant, T is the desired temperature, m is the mass of the particle γ is the damping factor. The

temperature of the system and γ vary from system to system and will be reported in relevant chapters.

This technique has been used to study a wide range of systems protein dynamics and polymer nanoparticles and will be used in this study to examine the unbinding dynamics. As we mentioned in section 2.1, it should be reiterated that transition/unbinding events have no specific lifetime, but rather follow a distribution of lifetimes. Thus, similar to MCMC simulations, to obtain the lifetime distributions and characterize the overall behavior, multiple trials need to be performed.

2.3 Steered molecular dynamics (SMD)

Steered molecular dynamics⁵⁵ (SMD) is a simulation technique that can be used to replicate experimental procedures such as atomic force microscopy (AFM) and force measuring optical tweezer (FMOT). In AFM experiments, molecules or other nanoscale structures are pulled via their attachment to a cantilevered tip and the forces/motions of this tip are recorded and used for analysis. These experimental procedures are often used to probe interfacial and mechanical properties of nanoscale materials.

In SMD, a force is applied to the system (or a subset of it) to enhance the sampling of the configurational space. To apply this force to the system, the steered/pulled atoms are tethered to a virtual atom through a harmonic spring. This virtual atom is moved with either a constant velocity or a constant force, and through the harmonic spring consequently causes all the steered particles in the system to move. In constant velocity SMD, the value of the stiffness of the spring is important, since it determines the pulling force on the system. In all our simulations we employ constant force SMD, where stiffness of the spring does not play a role in the pulling force.

The output of SMD simulations is the displacement of the steered atoms and the force applied to these atoms. From these quantities, we calculate the non-equilibrium work done on the system by the SMD potential along the reaction coordinate of interest as given by Eqn 2-9

$$W = \int_A^B F_{smd} \cdot dx \quad (2-9)$$

where A and B are the initial and final states of the system.

In biophysics and specifically catch bond literature, SMD simulations are used predict the effect of force on protein configurations from the static experimental structures^{11,26,32,36}. SMD simulates forces that are added in pulling experiments. It should be noted that SMD can only simulate the structure over tens of nanoseconds, and so the external force in the simulations is higher than physiological levels to speed up any force-induced changes²⁶. In this dissertation, we use this approach to investigate force-lifetime dependence of various systems that are far simpler than all atomistic protein models with tens of thousands of atoms.

In Chapter 4, SMD is used to exert force and separate a system from its ligand. In Chapter 5, it is used to separate nanoparticle fibers. Lastly, in Chapter 6, this technique is used to separate two surfaces connected with tethers. Ranges of forces and pulling locations are different in all applications and will be reported in detail in relevant chapters.

Chapter 3 - Investigating the viability of catch bonds as a nanoparticle interface

This chapter focuses on using Chaperon-Usher (CU) pili as a bio-interface for nanocomposite systems. CU pili are helical protein complexes expressed by bacteria *Escherichia coli* and have unique biomechanical properties that enhance the ability of bacteria to sustain attachment to surfaces under large stresses. We hypothesized that filler interfaces in nanocomposites with features designed after bacterial structural/adhesive biopolymers may lead to bioinspired nanoparticle networks that exhibit unique macroscopic mechanical properties.

First, we focus on modelling work for the elongation of a single CU pilus with catch bond adhesive tip and examine its toughness response. Next, using Monte Carlo simulations (Section 2.1) of single pilus elongation, we show that CU pili with catch bond tip can act as molecular seat belts that exhibit low toughness when pulled slowly and high toughness when pulled abruptly and rapidly. Portions of the text and figures within chapter are reprinted or adapted with permission from Dansuk and Keten, *Soft Matter* 2018²¹.

3.1 Mechanical properties of Chaperon-Usher Pili

Chaperone-Usher (CU) pili, or fimbria are anchored to the outer membrane of bacteria⁵⁶. CU pili carry adhesive proteins (adhesins) on their tip, which bind to specific receptors on the host cells or functional groups on abiotic surfaces. The notable features of pili decorated with tip adhesins are (1) slip/catch bond behavior at the adhesion tip, (2) force plateaus during mechanical unfolding, and (3) logarithmic increase in the unfolding force with the rate of deformation beyond the so-called corner velocity. The combination of these three key features confer interesting

abilities to bacterial cells, which enables strong binding under large shear forces, while simultaneously allowing dynamic functions such as motility.

The structure of the CU pili, which are commonly expressed by uropathogenic *Escherichia coli* (UPEC), is well-studied in the literature⁵⁷. CU pili are composed of over 10^3 protein subunits that are arranged into a micron long helical shaft which is a flexible rod-like structure measuring 6–7 nm in diameter (Fig. 3-1A)^{58,59}. One subfamily of CU pili, called type 1, conveys a special adhesin at the tip of the helical shaft that interacts with receptors/functional groups to form so-called catch bonds, which are molecular interactions that exhibit a longer lifetime with increasing force below a certain threshold (Fig. 3-1B).

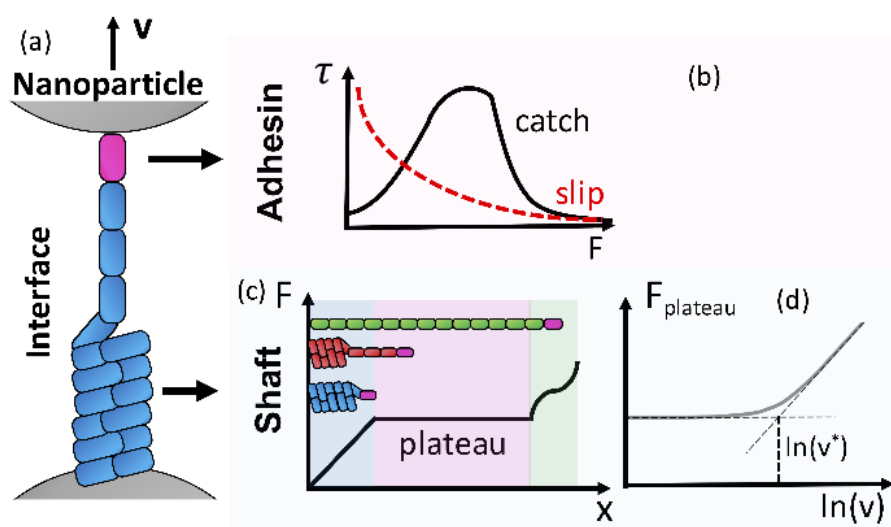


Figure 3-1 Notable features of bacterial pili A) Schematic of two nanoparticles with adhesive biopolymer inspired interface undergoing elongation. The pilus is expressed as a helical shaft (blue subunits) with an adhesin tip (pink subunit). B) The adhesin forms labile bonds with the particle. Labile connection can have a slip bond or a catch bond character. C) Force response of pilus with three elongations regions: linear (blue), plateau (red) and non-linear (green). In the plateau region the helical shaft exhibits large extension at a constant force, which is called the force plateau. D) The plateau force is a function of the elongation velocity.

Optical tweezers (OT) and atomic force microscopy (AFM) experiments have been used to quantify the biomechanical properties of CU pili, such as force extension behavior and adhesion lifetimes^{45,57,60,61}. During elongation, pili exhibit a unique force response, which is composed of three distinct regions (Fig. 3-1C). When the deformation is small, the pilus behaves like a Hookean spring and exhibits a linear force response. Applying greater strains leads to a plateau region, which is characterized by elongation at constant force (plateau force) due to reversible opening of the noncovalent bonds connecting the subunits of the unravelling pilus. Further extension of the pili leads again to a non-linear region, in which the force response is monotonically increasing along an S-shaped curve. In the absence of a force, the elongated pilus can retract to its original helical structure without any noticeable alteration of the mechanical properties⁵⁸. As shown in Fig. 3-1D, the magnitude of the plateau force depends on the elongation velocity, or equivalently the strain rate. For velocities below a certain corner velocity, v^* , the plateau force is independent of the elongation velocity, and is referred to as the steady-state uncoiling force (F_{ss}). For higher elongation velocities, the plateau force increases logarithmically with the velocity.

Lastly, FimH adhesin at the tip of the pilus forms catch bonds because mechanical force acts through a regulatory region to allosterically switch FimH bonds from a short-lived low affinity state to a long-lived high affinity state. In a recent study, it has been shown both by experimental analysis and molecular dynamics simulations that catch bond adhesin of the type 1 pili, FimH, is an allosterically regulated protein with one unbound and two conformational bound (low affinity and high affinity) states³³. High affinity state is sustained by force, since the protein undergoes conformational change as it switches to this state at high force levels.

3.2 Simulation setup

We have constructed our system based on a model of a single pilus under tensile stretching as shown in Fig. 3-1A. The pilus is connected to two nanoparticles with a catch/slip bond. The top particle is displaced to extend the pilus at a constant velocity. The elongation velocities studied are within the range of the experiments^{57,60}. To reproduce the force elongation response and catch bond lifetime of the pilus, the shaft and the tip of the pilus are modeled separately.

3.2.1 Catch bond modelling

In order to model catch bonds, we first need to understand behavior of noncovalent bonds in general. A noncovalent bond can be described in terms of an energy landscape, consisting of a minimum, representing equilibrium state of the bond and an intermediate local maximum, called the transition state. A closed bond can break, only if it “passes” this transition state. The energy of the transition state, E_b , schematically illustrated in Fig. 3-2, thereby represents the activation energy for bond opening.

In contrast to macroscopic systems, rupture (break) strengths for weak biochemical bonds are not constants but instead depend on the rate of force application and duration of loading. An increased rate of bond dissociation under external force, F , was first emphasized by Bell⁴² using a phenomenological model for the off rate, k

$$k = \omega \cdot e^{-\frac{E_b - F \cdot \Delta x}{k_B T}} \quad (3-1)$$

where ω is the natural vibration frequency, of the bond and E_b is the energy barrier, Δx is the transition state distance, and $k_B T$ is the thermal energy respectively. In some instances, natural frequency and exponential of the energy barrier is combined for a thermal off rate k^0 , which is

bond break rate in absence of force. The importance of Bell's insight is the quantification of the role of mechanical force in biological event rates.

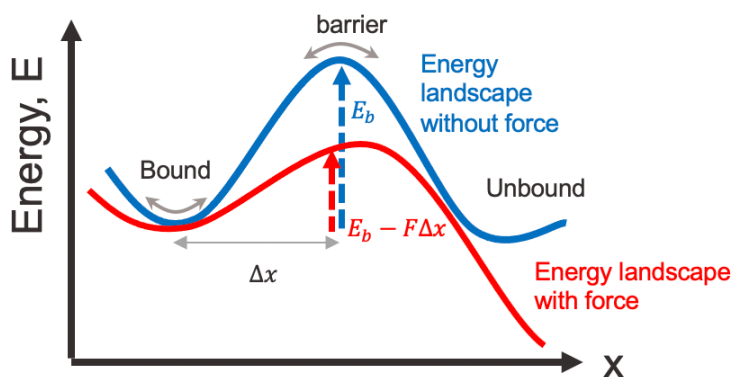


Figure 3-2 Energy landscape representation of a nonbonded interaction. External force acting on the interaction tilts the landscape and reduces the energy barrier

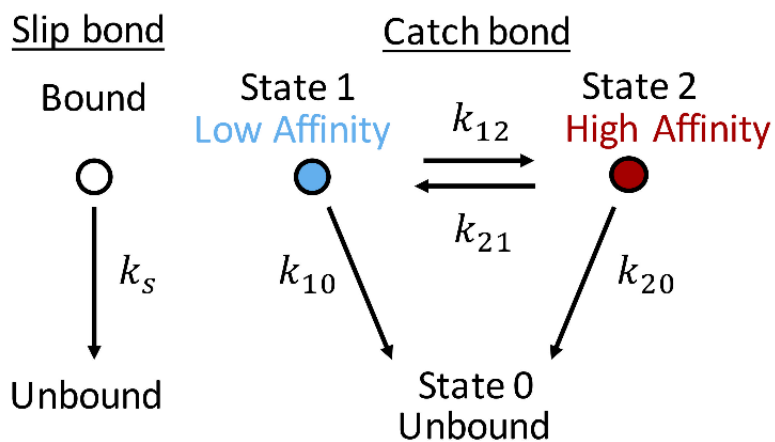


Figure 3-3 Slip and catch bond models. Slip bonds have one bound state; the bond break rate is given by k_s . Catch bonds have the two bound states: low affinity (state 1) and high affinity (state 2). The low affinity break rate and high affinity break rate are given by k_{10} and k_{20} respectively, where the unbound state is assigned as State 0. Catch bonds can switch among different adhesive states with the corresponding switching rates of k_{12} , transition rate from low to high affinity and k_{21} , transition rate from high to low affinity state.

Building upon the fact that pilus tip protein FimH form high and low affinity interactions with its ligand, we use two state model to quantitatively represent two bound states: State 1 (low affinity) and State 2 (high affinity), as shown in Figure 3-3. The unbound state is characterized as State 0. Initially, the pilus is attached to the particle with a catch bond at State 1. A catch bond can switch states according to the transition rates, which is rearranged version of Eqn 3-1:

$$k_{ij} = k_{ij}^0 \cdot e^{\frac{F \cdot \Delta x}{k_B T}} \quad (3-2)$$

The states are represented by indices, where i is 1 or 2 and j is 0, 1, or 2. Specifically, if the bond is in State 1, it can switch to the State 2 according to the corresponding switching rate of k_{12} , transition rate from low to high affinity, or it can break according to k_{10} , low affinity break rate. On the other hand, if the bond is in State 2, it can switch to the State 1 with k_{21} , transition rate from high to low affinity, or it can break with k_{20} , high affinity break rate. The rebinding of a bond is not considered, since bonds are under tensile force when opening, which is large enough to render the rebinding probability negligible⁴⁵. The simulation parameters are listed in Table 3-1 Transition rates originate from the parameter fits of the data from single FimH-mannose AFM pulling experiments, which is examined in Yakovenko et al⁶².

Table 3-1 Two-state model parameters

Symbol	Value
k_{10}^0	1.37 s^{-1}
k_{12}^0	$3.3 \times 10^{-5} \text{ s}^{-1}$
k_{20}^0	$5.1 \times 10^{-6} \text{ s}^{-1}$
k_{21}^0	0.11 s^{-1}
Δx_{10}	2.85 \AA
Δx_{12}	15.1 \AA
Δx_{20}	4.52 \AA
Δx_{21}	3.88 \AA
$k_B T$	$4.14 \times 10^4 \text{ pNnm}$

3.2.2 Pilus modelling

Three regions in the force elongation response of the pilus are represented with a piecewise function with three distinct force regions (Eqn 3-3). The linear response region has a slope k_l , the plateau region has a constant force value at $F_{plateau}$, and the non-linear region is represented by a line with slope k_n , from the linear regression of the top part of the S-shaped curve, i.e. the most likely region where the high affinity catch bonds will break due to high force range.

$$F(x) = \begin{cases} k_l x & \text{at } x \leq x_{lp} \\ F_{plateau} & \text{at } x_{lp} < x \leq x_{pn} \\ k_n x & \text{at } x_{pn} < x \end{cases} \quad (3-3)$$

where F is the force experienced by both the pilus and the tip and x is the elongation of the pilus^{60,62,63}. x_{lp} and x_{pn} are the boundaries between linear-plateau and plateau-nonlinear regions respectively. For the steady state conditions, the x_{lp} is $0.0137 \mu\text{m}$ and x_{pn} is $9.04 \mu\text{m}$ ⁶³. Notably $x_{pn} \sim 6N \text{ nm}$, N being the number of subunits of the pilus, where the factor of 6 is characterized as the elongation in nm due to opening of the noncovalent bonds connecting the subunits of the pilus^{60,64}. As the pilus enters dynamic state, both boundaries increase with the elongation velocity. The velocity dependence of the plateau force is also represented with piecewise function that is constant till the corner velocity, v^* , and increases logarithmically afterwards.

$$F_{plateau}(v) = \begin{cases} F_{SS} & \text{at } v < v^* \\ \alpha \log v - \beta & \text{at } v > v^* \end{cases} \quad (3-4)$$

where F_{SS} is the steady state plateau force and v is the elongation velocity. α and β (12.57 and 4.48 pN respectively) are derived from opening rates and the lengths of bonds between the subunits of the shaft.

Table 3-2 Pilus shaft model parameters

Symbol	Value
F_{SS}	28 pN
v^*	400 nm/s
k_l	2.1 pN/nm
k_n	0.246 pN/nm

3.3 Pilus elongation simulations

In the following simulations, we analyze the mean toughness of pili with different tip characteristics under constant velocity elongation. We first examine a pilus with a tip adhesion that exhibits slip bond behavior to show that the mean toughness of both the strong slip system (red circles, in Fig. 3.4A) and weak slip system (orange squares, in Fig. 3.4A) increase with the logarithm of the elongation velocity, owing to the increase in bond strength with the loading rate⁴⁴. Figure 3.4A also illustrates that the mean toughness of the pilus with strong slip tip is three orders of magnitude greater than the weak slip case for low velocities and a factor of ~ 1.5 times greater for high velocities. This is expected since pili with the weak slip bond tip break earlier than strong slip bonds 99% of the time, due to the six orders of magnitude difference in their break rates. Overall, our results indicate that the toughness of a pilus is highly dependent on catch bond parameters.

Next, we investigate how having catch bond ability in the tip influences the toughness. Interestingly, pilus with catch bond tip exhibits both weak slip and strong slip behavior depending on the pulling velocity (blue diamonds, in Fig. 3-4A). At low pulling velocities, a pilus with catch bond tip has similar toughness to a pilus with a weak slip bond tip and at high pulling velocities it has a similar toughness to a pilus with a strong slip bond tip. After the elongation velocity of 10^3 nm/s, which we will call the critical velocity, there is a surge in toughness that results in

transformation of the pilus from weak slip like behavior to strong slip like behavior. During this surge, the toughness of the pilus increases by a factor of ~ 15 . We didn't provide error bars for the toughness results, since depending on its affinity state, pilus shows two very different responses: pilus exhibits either small or very large elongations before tip unbinding (Fig. 3.4B). It should be noted that although Figure 3.4B shows pilus elongation for 400 nm/s, same two responses are seen in all the elongation velocities.

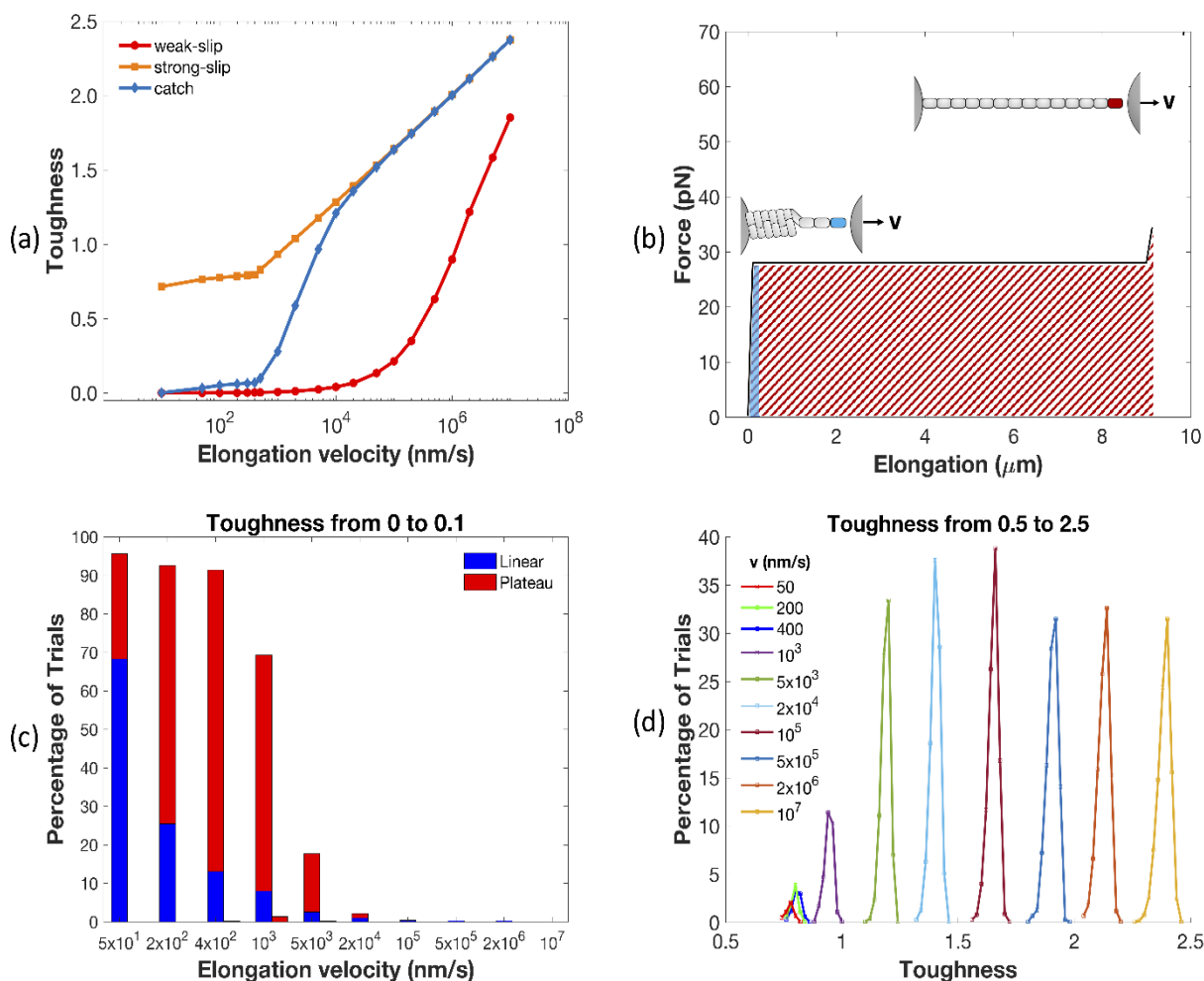


Figure 3-4 Constant velocity elongation simulations of single pilus with an adhesive tip A) Variation of toughness as a function of elongation velocity. The pilus with catch bond adhesion initially behaves similar to a pilus with weak slip bond adhesion. However, exceeding the 10^3 nm/s rate results in a toughness surge, leading to a transition to strong slip like behavior. B) Force-elongation curves and schematics of two trials of the pilus with catch bond adhesion elongated at 400 nm/s. In the first trial (turquoise), the catch bond doesn't switch states, remains in State 1, and the pilus unbinds at $0.22 \mu\text{m}$ (early plateau region). In the second trial (maroon), the catch bond switches from State 1 to 2 and the pilus unbinds at $9.36 \mu\text{m}$ (non-linear region). It is seen that for the entirety of the trials, pili either unbind quickly with small elongations at the low affinity catch bond state or undergo large elongations and unbind at high affinity catch bond state. C-D) Toughness distributions of elongation trials of single pilus with catch bond adhesion. C) Distribution up to 0.1 toughness. Each bar is grouped within the force response regions (linear, plateau) and expressed as the percentage of trials at various pulling velocities. For the highest elongation velocity 107 nm/s there are no trials in the 0-0.1 toughness interval. D) Distribution between 0.5 and 2.5 toughness. All trials break in the non-linear region and at State 2. Both histograms have a bin of 0.05. At low velocities, pili mostly break in the linear region/early plateau region and at State 1. As the velocity increases, more trials break in the non-linear region and at State 2.

for selected velocities in Figure 3-4C and D. For each trial, the toughness of the pilus, elongation region and the catch bond state until the break event are recorded. Figure 3.4C accounts for the pili that break after small elongations (linear and early plateau regions) and shows the toughness distribution up to 0.1. Within each interval the toughness values are grouped according to the force response regions (blue-linear, red plateau). Figure 3.4D accounts for pili that undergo large deformations (non-linear region) before they break. All the trials in Figure 3.4D break in the non-linear region. From the Fig. 3.4C and D, a bimodal distribution is observed, since the breaks are concentrated at the linear region/early plateau region and the nonlinear region, but not along the plateau region. This is expected since experiments show that catch bonds are likely to break easily at low forces (as in linear region) or high forces (as in non-linear region) and are strongest at intermediate forces (as in plateau region)⁶². In addition, all the linear region breaking events and early plateau region breaking events occur at State 1 (turquoise trial, Fig. 3-4B). In contrast, all the non-linear region breaking events occur at State 2 (maroon trial, Fig. 3-4B). This shows that when a pilus is in the plateau region and at State 1, it can still unbind, however, if the tip switches to the State 2, it will elongate without unbinding until it reaches the non-linear region. Thus, for a pilus to show high extensibility, which results in high toughness, its adhesion tip should switch to State 2, the strong affinity state.

Fig. 3-4C and D also reveals the effect of elongation velocity on the toughness distribution. At low velocities, most pili break in the linear region and at State 1. As the elongation velocity increases, the percentage of the linear and early plateau region breaking events decreases and the percentage of bond breaks in the non-linear region increases. The elongation rate dependent switch in the break position distribution is expected for catch bonds, since a slower loading rate would

allow a higher fraction to break before force was increased enough to stabilize them. If a pilus is subject to a faster elongation rate, (1) it will reach the plateau region faster and (2) plateau force will be higher due to corner velocity dependence. The former effect decreases the probability of the break event and the latter effect increases the probability of the shift. This implies that the higher the loading rate, the longer the pilus will have to be elongated before it detaches, which is consistent with findings in the literature⁶¹.

The behavior of a pilus closely resembles a seat belt that allows motion, when pulled slowly and locks/resists motion, when pulled rapidly. Similarly, pilus unbinds quickly and exhibits low toughness at low elongation velocities and has large elongation without unbinding and exhibits high toughness at high elongation velocities (Fig. 3-4A and B), therefore we will refer to pili with catch bond adhesin as “molecular seat belts”. By comparing the toughness response of pilus with slip bond tip to those with catch bond tip in Fig. 3-4A, we have established that the seat belt characteristics originate from the ability of pili to form catch bonds with the surface: the two force induced affinity states give the duality to the toughness response. Furthermore, from Fig. 3-4C and D we find that three regions in force response enhance the seat belt effect further. The linear region allows early breaks before the force is increased enough for a switch from State 1 to 2. These early breaking events govern the low velocity behavior of the interface. Plateau region, on the other hand, provides the optimal range of force for the switch from State 1 to State 2 and keeps the force on the adhesin below 100 pN, where the catch bond exhibits high break frequency⁶². Hence the pilus can elongate significantly while still being attached to the surface. Lastly, non-linear region provides the high force ranges where the break probability of the catch bond is high. In summary, both the pilus deformation and catch bond behavior cooperates to produce the seat belt effect.

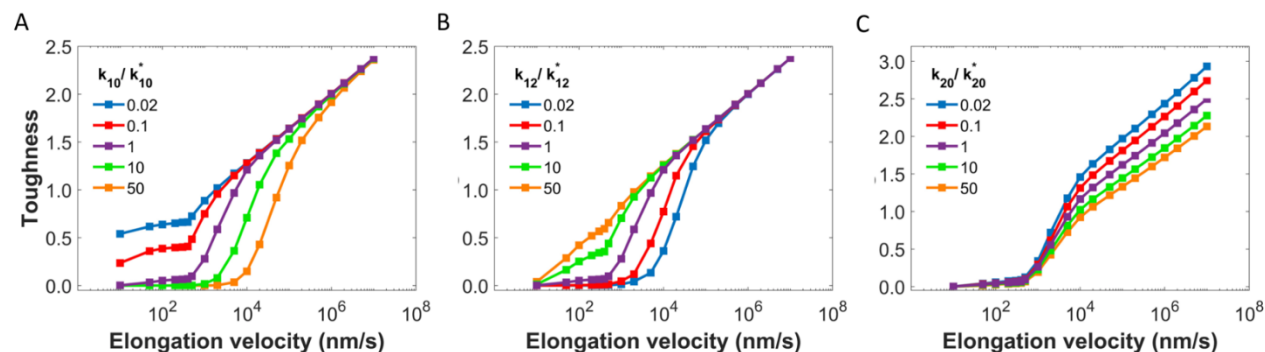


Figure 3-5 Effects of variation of catch bond rate parameters on the toughness of a single pilus as a function of pulling velocity. A) low affinity break rate k_{10} , B) transition rate from low to high affinity k_{12} , C) high affinity break rate k_{20}

After establishing the seat belt behavior in pilus, we systematically vary catch bond and shaft parameters to examine the factors that affect the toughness behavior of a single pilus. Experiments performed on various types of CU pili show that there are indeed variations in shaft and tip properties^{65,66}. From Figure 3-5, it is observed that changes in catch bond rate parameters affect both the critical velocity, i.e. the velocity at the start of the surge, and the sharpness of the surge, i.e. the steepness of the curve that connects the weak slip to the strong slip behaviors. Variations in rates are normalized with respect to the base case parameters listed in Table 1. As shown in Figure 3-5A, the increase in low affinity break rate (k_{10}) increases critical velocity and sharpness of the surge. When the break rate is high, it is easier for the adhesin to be detached. Thus, more trials will detach before switching to the high affinity state, which causes the surge to sharpen and shift to higher velocities. On the other hand, increase in transition rate from low to high affinity (k_{12}), decreases the critical velocity and the sharpness of the surge (Fig. 3-5B). Notably, when k_{12} is significantly reduced, the pili will have weak slip behavior (the toughness response will be very similar to the red line in Figure 3-4A) and when k_{12} is significantly increased,

the pili will have strong slip behavior (the toughness response will be very similar to the orange line in Figure 3-4A) Namely, in the extreme values of k_{12} catch bond effect disappears. Change in the high affinity break rate (k_{20}) does not have a huge impact on the surge, which suggests that the surge is controlled by the ratio between the State 1 to State 2 transition and the State 1 break rate. However, k_{20} strongly influences toughness at high velocities (10^4 - 10^7 nm/s). If k_{20} decreases, the pili which are in State 2 will tend to break at a higher force at the non-linear region, which will result in higher toughness. Unless there is a substantial change in its value, varying the transition rate from high to low affinity (k_{21}) led to small changes the toughness responses, therefore k_{21} simulation results are not included in this work. The switch from high to low affinity is much less probable than other transitions since previous works showed that the high affinity state is stable over some period of time. The transition state distances Δx are also varied in simulations. The results show a trend that is opposite of the rate changes: the increase in Δx_{10} , Δx_{12} and Δx_{20} , have similar effects of decreasing k_{10} , k_{12} , k_{20} . Ideally, the best performing seat belt should have low toughness at low velocities, followed by a very sharp rise in toughness at higher velocities. The plots in Fig. 3-5 reveals that the ideal seat belt behavior can be reached by decreasing k_{20} , k_{12} and increasing k_{10} .

To get a better understanding of the effect of shaft characteristics on the toughness of the pilus, we vary the number of subunits, steady state uncoiling force and the corner velocity. As shown in Figure 3-6A, increasing the number of subunits, N , increases both the sharpness of the surge and the toughness at high velocities (10^4 - 10^7 nm/s), but doesn't change the critical velocity. The slope of the toughness vs $\log(v)$ at high elongation velocities increase by a factor of 4 with increase in N from 500 to 2500. Since the elongation in plateau region results from opening of

noncovalent bonds connecting the subunits of the pilus, increase in N will increase the plateau region elongation ($x_{pn} \sim 6N$). Extra elongation from a higher N pilus at logarithmically increasing

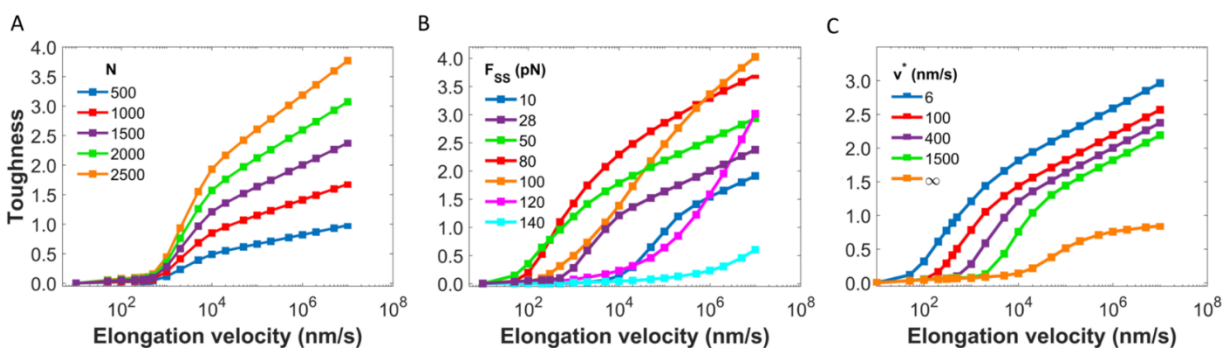


Figure 3-6 Effects of variation of shaft parameters on the toughness of a single pilus as a function of pulling velocity. A) Number subunits (N): Increasing the number of subunits, N , increases both the sharpness of the surge and the toughness at high velocities, however, doesn't change the critical velocity. B) Steady state plateau force (F_{SS}): Increase in F_{SS} initially enhances the seat belt effect, after F_{SS} goes beyond 100 pN, the pilus starts to behave more like it has a slip bond adhesin. C) Corner velocity (v^*): decrease in corner velocity decreases the critical velocity, but increases the overall toughness of the pilus for all pulling velocities.

plateau force will provide additional toughness at high velocities. Therefore, both the sharpness of the surge and the slope of the toughness scaling in the high velocity increase as N goes up.

We next show the effects of varying the steady state uncoiling force in Figure 3-6B. When the steady state uncoiling force F_{SS} increases from 10 pN to 100 pN, magnitude of toughness at high velocities increases. However, when F_{SS} exceeds 100 pN, the pili start to behave as if they have slip bond tips, particularly 120 and 140 pN curves are very similar to weak slip bond tip curve in Fig. 3-4A. Both our simulations and the AFM experiments of single isolated tip adhesin FimH show that when a force above 100 pN is applied to the adhesin, it unbinds frequently. Here, we want to further emphasize the correlation between the mechanical properties of shaft and the catch bond properties of the adhesin. Although increasing F_{SS} initially results in low toughness at low

velocities, followed by a very sharp rise in toughness at higher velocities, i.e. ideal seat belt behavior, due to the increase in high affinity break rate with respect to the force, increasing F_{SS} over 100 pN undermines the seat belt behavior rather than promote it further.

Next, we examine the effect of the corner velocity on the rate dependence of the toughness curve. Fig. 3-6C reveals that increasing the corner velocity increases the critical velocity of the transition and decreases the toughness at high velocities. Notably, corner velocities of 6 nm/s and 400 nm/s and 1500 nm/s are the experimental values for type 1 pili and P pili, F1C pili respectively⁶⁷. If the corner velocity is infinite (orange line, in Fig. 3-6C), i.e. the plateau force is independent of the pulling velocity, the real contribution to the toughness response comes from the long elongation in the plateau region. It is clear from this data that the corner velocity is a key parameter in seat belt behavior, since the magnitude of the toughness in the plateau region is governed by the plateau force, whose transition to velocity dependent behavior is chiefly governed by the value of the corner velocity. Setting the corner velocity to be very high leads to an almost sigmoidal, switch-like behavior. However, setting the corner velocity to be a small value forces the transition to set in earlier and creates a higher toughness response over a broader velocity range. To sum up, by systematically varying the catch bond and shaft parameters in our simulations, we have shown that k_{10} , k_{12} , k_{20} , N , F_{SS} and v^* are key parameters for tuning the performance of the seat belt that may offer flexibility in material interface design.

3.4 Conclusion

In this study, we hypothesize that CU pilus with catch bond adhesin —a bacterial biopolymer with the ability to attach to biotic/abiotic surfaces— can be a good template for nanocomposite design, particularly to its unique biomechanical properties of (1) catch bond

behavior at the adhesion tip, (2) force plateaus during mechanical unfolding, and (3) logarithmic increase in the unfolding force with the rate of deformation beyond the corner velocity. Hence, our challenge was to parametrically explore the toughness of particle interfaces in composites that are inspired from bacterial adhesins. Based on previously developed biomechanical models of CU pili and their tip adhesins, we have presented MC simulations of the pilus response under constant velocity pulling and particle deceleration scenarios.

We showed that the seat belt behavior, which originates from catch bond mechanism, is enhanced by the three-region force response of the CU pili. By tuning the pili parameters, an ideal seat belt behavior with low toughness at low velocities, followed by a very sharp rise in toughness at higher velocities, can be achieved. Notably, this requires increasing the transition rate from high to low affinity k_{12} , the high affinity break rate k_{20} , the number of subunits N , the corner velocity v^* while decreasing the low affinity break rate k_{10} . Finally, we showed that the critical velocity of the low-high toughness transition can be adjusted by using the same parameters, which enables pili to turn the strength on and off at a specific strain rate.

In conclusion, we have highlighted the potential of CU pili with catch bond adhesin as molecular seat belt mechanisms. Even though the results presented in this work apply quantitatively to the CU pilus, we believe that the mechanisms can be transferable to nanocomposite systems such as hairy nanoparticle assemblies or hydrogels⁶⁸⁻⁷¹. By mimicking helix-like shaft and its adhesin, one can build and tune composite interfaces that exhibit seat belt characteristics. However, to coopt adhesion strategies of the CU pili, it will be necessary to discover pathways that reproduces the catch bond, corner velocity and force plateau behavior of pili in synthetic systems^{19,72,73}. Furthermore, cooperativity of the pili in multipili-binding

applications, i.e. nanoparticle networks, needs to be further explored. Prior experiments and simulations show that polymer networks with labile bonds that can break and reform have self-healing capabilities⁷⁴⁻⁷⁶. Pili will provide reversible extensibility to the dynamic-reconfigurable networks due to their unfolding and refolding properties, that may enhance the self-healing mechanism. Multi-pili attachment simulations of Bjornham et al. and *E. coli* rolling behavior simulations of Whitfield et al. showed the pili can cooperatively redistribute external forces among each other, which increases the adhesion lifetime significantly by lowering the load on individual catch bonds^{77,78}. The multiple pili seat belts would require a more detailed model with recoiling of the pilus and reattachment of adhesin tip. Although from this work it can be deduced that redistribution of the force will allow pili tips to have longer lifetime that will increase the toughness of the seat belt system, multi-pili cases should be investigated to generalize our conclusions to more complex interfaces and networks. It is anticipated that the long-term impact of our work will be to design network related to single pilus and multi-pili response models.

Chapter 4 - Creating simple molecular systems that exhibits catch bond behavior

Having characterized catch bond adhesins as a nanoparticle interface in Chapter 3, we move forward to mimic adhesin strategies at the molecular level using simple geometric designs. As mentioned in Section 1.2, many catch bond models have fallen short of providing the quantitative structural and dynamical insight required to explain how allosteric proteins achieve these force-induced lifetime enhancements under thermal motions at the nanoscale. The open question we addressed in this chapter is how to create a simple, Newtonian molecular system that exhibits catch bond behavior reliably and predictably under thermal excitations.

In the first section of this chapter, we will talk about our simple tweezer-like design that exhibits catch bond behavior when simulated under thermal excitations. Next, applying kinetic theory to a two-mass-two-spring idealized model of the tweezer, we show that by tuning the shape of the switch and the ligand-tweezer interaction energy landscapes, we can achieve greater lifetimes at larger force levels. Lastly, we validate our theory with molecular dynamics simulations and produce a characteristic lifetime curve reminiscent of catch bonds. Portions of the text and figures within chapter are reprinted or adapted with permission from Dansuk et al. Matter 2018⁷⁹.

4.1 Key catch bond features

Our approach to this problem is to design simple mechanical systems that can capture (i) structural changes in catch bond proteins due to mechanical forces, and (ii) alterations in unbinding kinetics due to structural changes. Prior experiments and simulations⁸⁰⁻⁸³ have shown that some catch bond proteins including FimH, selectin and cadherin are biphasic, consisting of a conformation with low ligand binding affinity and a conformation with high ligand binding

affinity (Figure 4-1). The crystal structures of its conformations illustrate that FimH has two domains³². The pilin domain (Fig. 4-1A,B, red region) connects FimH to appendages of bacteria. The lectin domain (Fig. 4-1A,B, cyan region) has a binding pocket, allowing attachment of the adhesin to the ligand expressed on cell surfaces. The affinity of the ligand is mediated by the lectin binding pocket and its loop segment³³. When the FimH-ligand complex is in the open conformation, the interaction between the loop segment and the ligand is minimal (Fig. 4-1C). In contrast, in the closed conformation, due to allosteric changes, loop closes on and forms new interactions with the ligand (Fig 4-1D). Both conformations bind to the ligand, but crucially, the ligand lifetime is larger in the closed conformation due to additional interactions formed between the ligand and the loop segment. It should be noted that a very similar biphasic mechanism is observed in P selectin⁸¹ and cadherin proteins⁸⁴. Tensile force applied to the ligand increases the probability of a transition from the open to the closed conformation, which leads to a prolonged lifetime at intermediate levels of tensile force. In short, the key features of the catch bond proteins can be summarized as:

- existence of two discrete conformational states
- force induced transition between the states
- increase in ligand affinity by formation of new interactions between the protein and the ligand as a result of structural changes that happen during transition of states

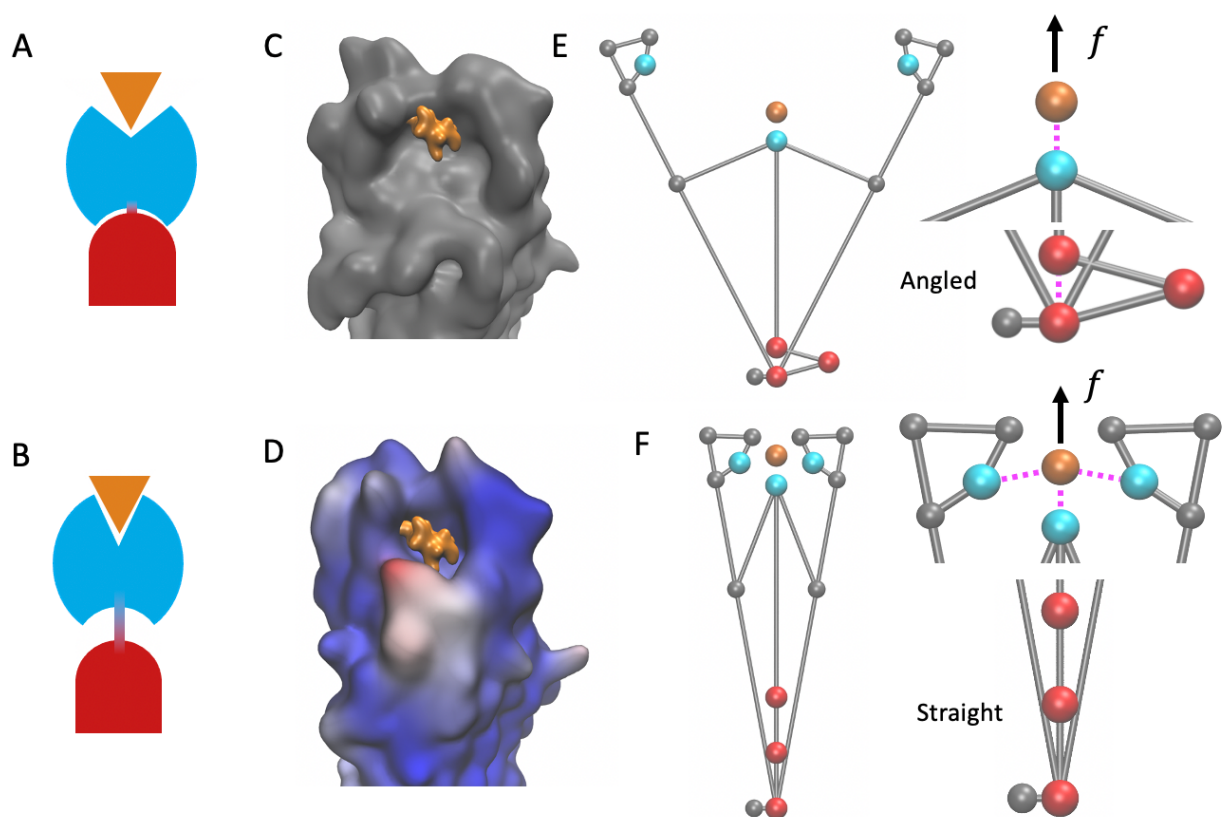


Figure 4-1 Catch bond models. Schematics of A) open and B) closed conformation of FimH protein with lectin (cyan) and pilin (red) domains. Ligand (mannose) is shown in orange. C) Open (PDB 4XOD) and D) closed conformation (PDB 4XOB) of ligand binding pocket, located on the lectin subunit. The closed conformation is colored via a scale (blue=small, white=middle and red=large), which shows the displacement of the atoms relative to the open conformation. As FimH transitions from its open to closed conformation, the loop segment closes on the ligand, forming new interactions. The tweezer design is inspired from FimH and has main and secondary binding sites (cyan) and pairwise switch (red). E) In open conformation ligand forms one interaction with the tweezer and the switch members are angled. F) In closed conformation ligand forms three interactions with the tweezer and the switch members are straight. Interactions and applied external forces are indicated by pink dashed lines and black arrows respectively.

4.2 Designing the tweezer with catch bond behavior

Based on the three key features discussed above, we design a tweezer-like structure that can transition between open and closed conformations. In the open conformation (Fig. 4-1E), the arms of the tweezer are far apart, giving the ligand (orange bead) a clear path to attach to the exposed main binding site (MBS) at the center of the binding pocket (central cyan bead). Located at the arms of the tweezer, there are secondary binding sites (SBS) (lateral cyan beads). When the ligand is attached to the MBS and the tweezer is in its open conformation, the ligand does not interact with the SBS, since they are much further away. In contrast, in the closed conformation (Fig. 4-1F), the arms of the tweezer rotate towards the center and enable interactions between the ligand and SBS. Since the number of interactions increases from 1 to 3 (Fig. 4-1E & F, pink dashed lines), the ligand has higher affinity in the closed conformation. Thus, in context of ligand unbinding, we will refer to open and closed conformations as low affinity (LA) state and high affinity (HA) state respectively.

To enable force-dependent transitions between the two conformations, a switch is added to the tweezer. The switch consists of a two-member hinge with a pairwise interaction between its two free ends (red beads, Fig. 4-1E & F). In the open conformation, the members are angled (Fig. 4-1E), however, when the pairwise interaction between the red beads breaks due to external forces, the members become straight (Fig. 4-1F). A rigid member connects the switch to the MBS. Straightening of the switch moves the MBS upwards and drives the tweezer arms inwards, which leads to the closed conformation. Thus, breaking and reforming of switch interaction controls the transition between the conformations.

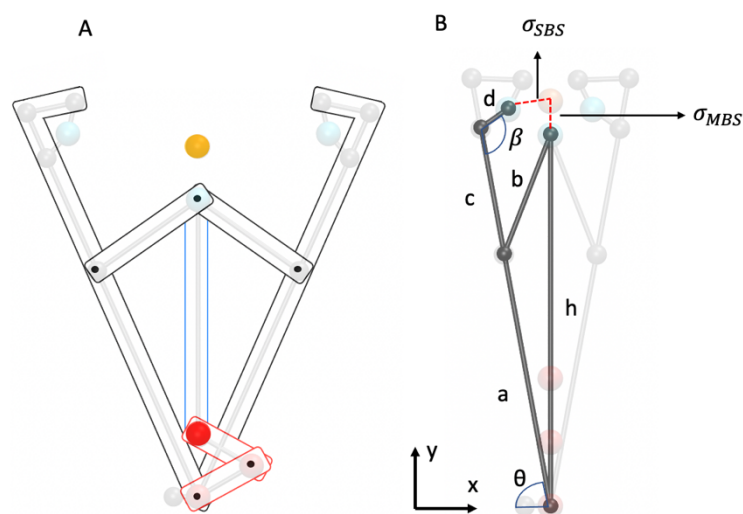


Figure 4-2 Rigid member representation of tweezer geometry in open conformation. Switch (red) and ligand (orange) beads have masses 50 times the other beads B) Dimensions of the tweezer in closed conformation.

The tweezer design consists of rigid members that are connected with hinge joints. As shown in Fig 4-2, the tweezer has 4 members (black), the switch has 2 members (red) and a single member (blue) connects the switch and the tweezer. Mass of the ligand (orange bead) and mass of the switch (read bead) is 500 g/mol. All the other beads are 10 g/mol.

It should be noted that in order to reach an equilibrium state in the closed conformation, equilibrium distances σ of the interactions need to be adjusted according to the dimensions of the tweezer. In Figure 4-2, we refer to important dimensions that are required to determine σ . The dimensions used in this work are listed in Table 4-1.

The x-y coordinates of the secondary binding site (SBS) in the closed conformation are

$$x_{SBS} = (a + c) \cos \theta - d \cos(\beta - \theta), \quad (4-1)$$

$$y_{SBS} = (a + c) \sin \theta + d \sin(\beta - \theta). \quad (4-2)$$

All the parameters in Eqn. 4-1 & 4-2 are constant except θ and h . Their relation is shown as

$$\cos(90^\circ - \theta) = \frac{a^2 + h^2 - b^2}{2ah}. \quad (4-3)$$

In the closed conformation, the distance between the ligand and the SBS should be equal to the equilibrium distance of their interaction potential σ_{SBS} . Thus, the relation between σ_{SBS} , x_{SBS} and y_{SBS} becomes

$$\sigma_{SBS} \cong \sqrt{(h + \sigma_{MBS} - y_{SBS})^2 + x_{SBS}^2}, \quad (4-4)$$

where σ_{MBS} is the equilibrium distance of ligand/main binding site interaction.

Table 4-1 Tweezer Dimensions

Member	Value
a	15 Å
b	7.5 Å
c	7.5 Å
d	2 Å
h	21.75 Å
β	78°

4.3 Tweezer Lifetime Curves

In our setup, a constant force is applied to a ligand that is attached to the tweezer system. Depending on the conformation of the tweezer, four events can be observed (Fig. 4-3). In the open conformation, the ligand may undergo a LA unbinding, or the tweezer may transition to its

closed conformation, which we will call the forward transition (S^+). In the closed conformation, ligand may undergo a HA unbinding, or the tweezer may transition to the open conformation, which we will call the backward transition (S^-). These four events occur in a stochastic fashion due to the presence of thermal motion. Therefore, transition/unbinding events have no specific lifetime, but rather follow a distribution of lifetimes. To characterize the probability of these events as a function of force and obtain the lifetime distributions, multiple trials need to be performed at each force magnitude. Average lifetimes $\langle \tau \rangle$ can then be computed from these lifetime distributions.

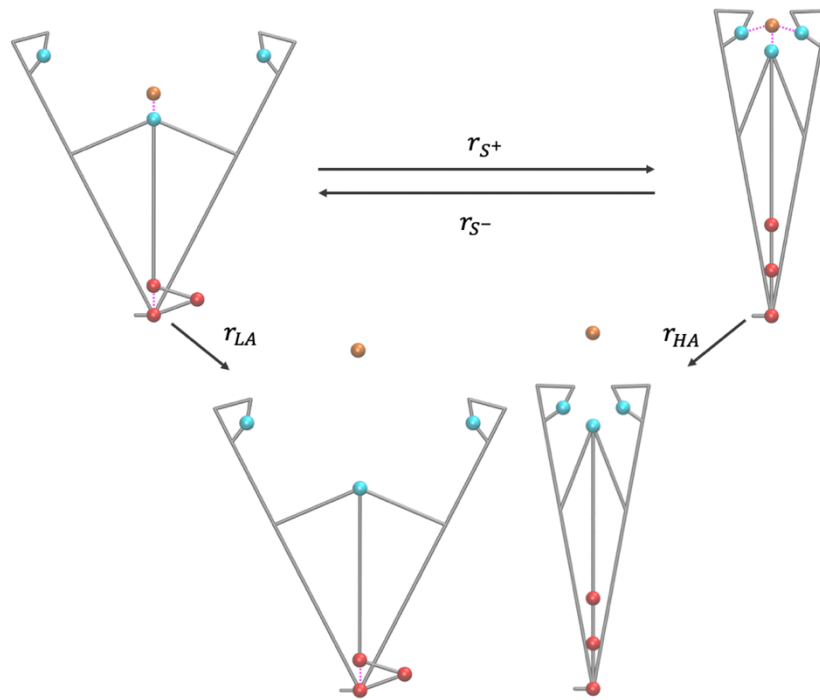


Figure 4-3 Rates of tweezer/ligand events. Forward transition rate r_{S+} , backward transition rate r_{S-} , low affinity unbinding rate r_{LA} , high affinity unbinding rate r_{HA}

In a typical trial, the tweezer will go back and forth between its open and closed conformations and eventually, the ligand will unbind either at the LA or the HA state. Thus, the ligand will have the following lifetime

$$\tau_T = \begin{cases} \sum_{i=0}^N (\tau_{S^+,i}) + \sum_{j=0}^M (\tau_{S^-,j}) + \tau_{LA} & \text{when } M = N, \text{ i. e. LA unbinding} \\ \sum_{i=1}^N (\tau_{S^+,i}) + \sum_{j=0}^M (\tau_{S^-,j}) + \tau_{HA} & \text{when } M = N - 1, \text{ i. e. HA unbinding,} \end{cases} \quad (4-5)$$

where τ 's are the lifetimes of the events and N and M are the number of forward and backward transitions respectively. For example, if the ligand unbinds at the LA state without any transitions

($N=M=0$), then $\tau_T = \tau_{LA}$ and if the ligand unbinds at the HA state after two S^+ and one S^- ($N=2$, $M=1$), then $\tau_T = \tau_{S^+,1} + \tau_{S^+,2} + \tau_{S^-,1} + \tau_{HA}$. To reproduce the characteristic catch bond lifetime curve like the ones in Fig. 1-1B, the mean lifetime of the ligand $\langle \tau \rangle_T$ must increase when a tensile force is applied. For this to happen, there must be force-dependent competition between the open conformation events (S^+ vs. LA) such that at small forces, most trials should result in LA unbinding, and at large forces, most trials should transition to the closed conformation (HA state) before LA unbinding can occur. The second condition is that the mean HA unbinding lifetime $\langle \tau \rangle_{HA}$ must be longer than mean LA unbinding lifetime $\langle \tau \rangle_{LA}$. Satisfying these two conditions will result in a higher percentage of trials unbinding at larger lifetimes, which guarantees the increase in $\langle \tau \rangle_T$.

Right from the start, we can verify that the second condition holds for our system, since ligand has two additional interactions in the closed conformation. Thus, $\langle \tau \rangle_{HA}$ will always be greater than $\langle \tau \rangle_{LA}$. To assess the validity of the first condition, we will define the force-dependent competition between the open conformation events by considering the probability of the LA unbinding preceding the forward transition:

$$P(LA < S^+) = \int_0^\infty P(S^+ > t | LA = t) P(LA = t) dt. \quad (4-6)$$

LA and S^+ are random variables of the corresponding events discussed above. At constant force, i.e. constant unbinding rate r , LA and S^+ will be distributed according to the exponential probability density function $f(t) = r e^{-rt}$. Since the events are independent, we get

$$P(LA < S^+) = \int_0^\infty \exp[-r_{S^+}t] r_{LA} \exp[-r_{LA}t] dt = \frac{r_{LA}}{r_{LA} + r_{S^+}}. \quad (4-7)$$

Considering that the mean of the exponential distribution, r^{-1} , is also $\langle\tau\rangle$, Eqn. 4-7 can be expressed in terms of $\langle\tau\rangle$ as

$$P(LA < S^+) = \frac{\langle\tau\rangle_{S^+}}{\langle\tau\rangle_{LA} + \langle\tau\rangle_{S^+}}. \quad (4-8)$$

In this analysis, we did not account for cases where LA unbinding will occur after one or more S+/S- transitions take place. In reality, these cases can occur, but their contribution to the mean lifetime, $\langle\tau\rangle_T$, is generally negligible. Ideally, we want Eqn. 4.8 to be approximately equal to 1 at small forces and decrease at larger forces. Note that since the interaction lifetimes decrease exponentially with force⁴², to achieve the desired trend (i) $\langle\tau\rangle_{S^+}$ must be greater than $\langle\tau\rangle_{LA}$ at small forces and (ii) $\langle\tau\rangle_{S^+}$ must be more sensitive to force (has a sharper decline) than $\langle\tau\rangle_{LA}$ at larger forces. Hence, we propose that the lifetime-force curves of these two events, $\langle\tau\rangle_{S^+}$ and $\langle\tau\rangle_{LA}$, should converge. Convergence of the curves will favor transition to the HA state for large values of force.

We can follow the same procedure in Eqn. 4-8 to write probability of HA unbinding preceding the backward transition

$$P(HA < S^-) = \frac{\langle\tau\rangle_{S^-}}{\langle\tau\rangle_{HA} + \langle\tau\rangle_{S^-}}. \quad (4-9)$$

Unlike the other three events, mean lifetime of the backward transition $\langle\tau\rangle_{S^-}$ exponentially increases with force. i.e. the force on the ligand creates a moment in tweezer arms towards the center, which stabilizes the closed conformation. Therefore, at larger forces, Eqn. 4-9 will

approach to 1 and M in Eqn. 4-5 will go to 0. The increase in $\langle\tau\rangle_{S^-}$ and decrease in M will also promote the time spent in the HA state.

In conclusion, force-dependent competition between the open conformation events is the origin of the catch bond behavior and closed conformation events enhance this behavior by delaying the unbinding of the ligand. As a result, at large forces, higher percentage of trials unbind at larger lifetimes which will increase mean lifetime, $\langle\tau\rangle_T$.

4.4 Energy Landscape Design

Next, the key question that must be answered is how to tune the force dependencies of the $\langle\tau\rangle$ s of each event. We will refer to the reaction-rate theory, where the unbinding of a particle corresponds to overcoming an energy barrier along a single reaction coordinate x , which describes the particle position along the energy landscape^{43,85}. Here, the dynamic response of the particle can be described by the Langevin equation (Section 2.2.1).

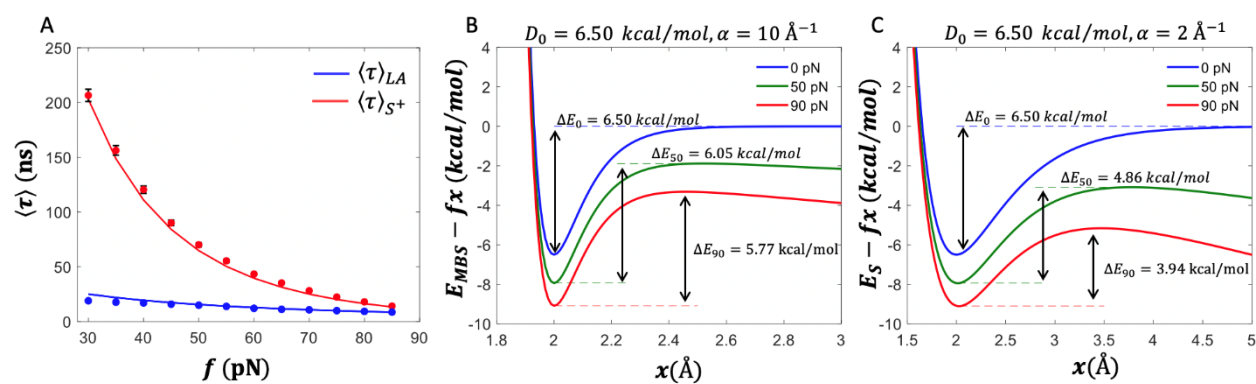


Figure 4-4 Mean lifetime versus force curves of low affinity unbinding $\langle\tau\rangle_{LA}$ (blue) and forward transition $\langle\tau\rangle_{S^+}$ (red) events. At low forces $\langle\tau\rangle_{S^+}$ is greater than $\langle\tau\rangle_{LA}$ and at larger forces, lifetime curves start to converge. The lines are analytical curves from Eqn 4-10 and the symbols are the 1D molecular dynamics simulation results. The error bars represent 95% confidence interval, derived by the bootstrapping method. The shape of the $\langle\tau\rangle_{LA}$ and $\langle\tau\rangle_{S^+}$ curves are governed by B) ligand-MBS energy landscape $E_{MBS} - fx$ and C) switch energy landscape

$E_S - fx$ respectively. External force f applied to the interaction tilts E to $E - fx$, decreasing the energy barrier ΔE . f results in a greater reduction in ΔE for energy landscapes with wider wells, e.g. for $f = 90$ pN, ΔE of E_S is decreased by 39 % compared to ΔE of E_{MBS} , which decreases 11 %.

In this work, Morse potentials (Fig. 4-4B & C, blue) are used to represent the ligand-MBS interaction (E_{MBS}), ligand-SBS interactions (E_{SBS}) and the interaction that makes up the switch (E_S). The form of Morse potential is discussed in Section 2.2 in detail. As shown in Fig. 4-4B and C, applying a constant force f on a pairwise potential tilts its energy landscape and yields to an effective potential of $E(x) - fx$, which modifies the height and location of the energy barrier of transition ΔE ⁸⁶. If the energy landscape of an event is specified, Kramers'^{87,88} theory can be used to predict the force-dependent transition rate $r(f)$ through the following equation

$$r(f) = \frac{\omega^w(f)\omega^b(f)}{2\gamma\pi} \exp[-\Delta E(f)/k_b T], \quad (4-10)$$

where ω^w and ω^b are the effective oscillation frequencies at the well and at the barrier of the tilted potential respectively.

As shown in Fig. 4-5A, E_{MBS} and E_S are serially connected and subjected to f applied to the ligand. Since the mass of the tweezer-ligand complex is concentrated on the two central particles, our system can be approximately modeled as a two-mass/two-spring system. Therefore, to find ω^w and ω^b , we will refer to vibration theory, where the motions of the ligand (L) and the switch (S) are not independent, but coupled by their attachments to the springs (interactions) with the following equations

$$m_L \frac{d^2 x_L}{dt^2} = -k_{MBS} x_L + k_S (x_S - x_L) \quad (4-11)$$

$$m_s \frac{d^2 x_s}{dt^2} = -k_s(x_s - x_L), \quad (4-12)$$

where m_L and m_s are the masses of the ligand and the switch (in our case $m_L = m_s$) and k represents the stiffness/curvatures of the springs/energy landscapes. The linear spring constants can be obtained by using the harmonic approximation for the tilted Morse energy landscapes $E_{MBS} - fx$ and $E_S - fx$ (Fig. 4-5B). Note that $E_{MBS} - fx$ and $E_S - fx$ have two stiffness values, k^w and k^b , which will be significant in calculating ω^w and ω^b . Since the solution to the equations of motion will take the form $x = A \exp[i\omega t]$, Eqn. 11-12 can be written in matrix form as

$$\begin{bmatrix} k_{MBS} + k_s - m\omega^2 & -k_s \\ -k_s & k_s - m\omega^2 \end{bmatrix} \begin{bmatrix} A_L \\ A_S \end{bmatrix} = \begin{bmatrix} 0 \\ 0 \end{bmatrix}. \quad (4-13)$$

Setting the determinant equal to zero to find the eigenvalues gives two positive solutions for ω , which are frequencies of the normal modes of the two-degree-of-freedom system. In our case, ligand-MBS interaction will be considerably stiffer than the switch interaction, since k is proportional to α^2 and $\alpha_{MBS} > \alpha_S$ (the rationale for this choice will be explained later). Thus, the first normal mode, in which the two masses move in phase, will govern the activation of the switch and second normal mode, in which masses move out of phase, will govern the unbinding of the ligand. ω^w values are found by using k_{MBS}^w and k_S^w , ω_{MBS}^b is found by using k_{MBS}^b and k_S^w and ω_S^b is found by using k_{MBS}^w and k_S^b in Eqn. 4-13. Hence, if the interaction parameters (D_0, α) and masses are prescribed, we can calculate the dissociation rate and $\langle \tau \rangle$ (inverse of the rate) of the two interactions that are serially connected.

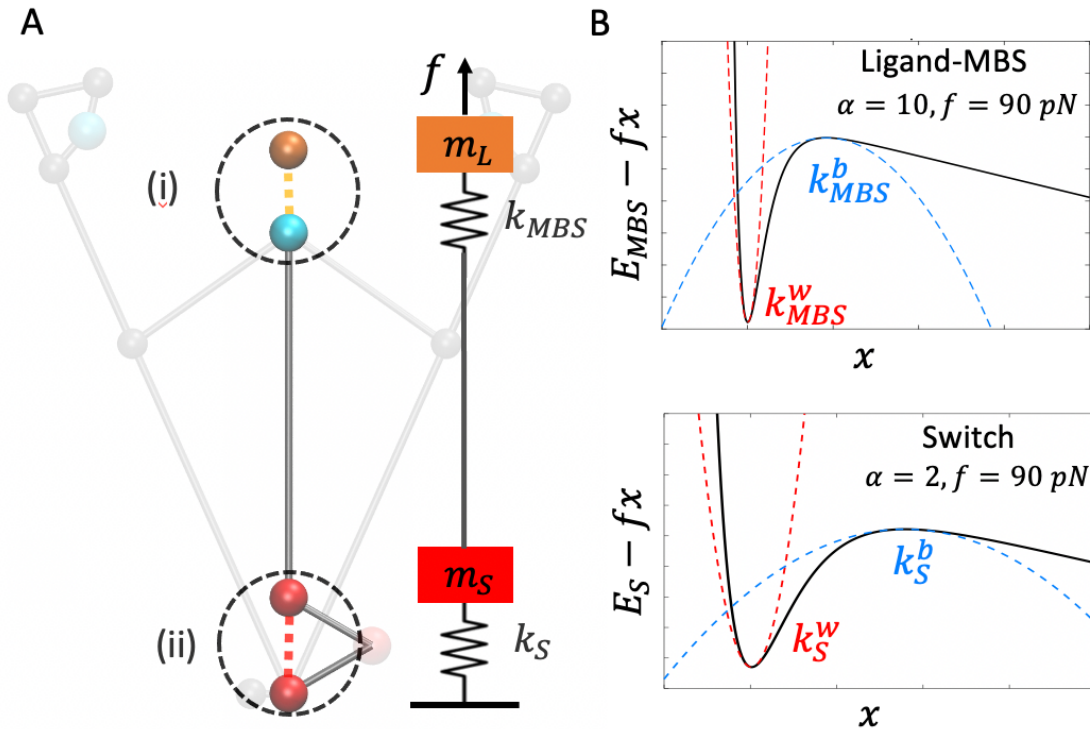


Figure 4-5 Stiffness representation of tweezer system A) The tweezer-ligand complex can be modelled as a two-mass/two-spring system, since (i) ligand-MBS interaction and (ii) switch interaction are serially connected and bead masses besides the ligand (m_L) and the switch (m_S) are low. B) By using harmonic approximation for the well (red) and the barrier (blue) regions, well stiffness k^w and barrier stiffness k^b of the tilted Morse energy landscapes of the ligand and the switch are obtained.

Now that we have the necessary tools to predict $\langle \tau \rangle$, we revisit the two conditions we have determined with Eqn. 4-6 to generate a catch bond behavior: (i) $\langle \tau \rangle_{S^+}$ must initially be longer than $\langle \tau \rangle_{LA}$ and (ii) $\langle \tau \rangle_{S^+}$ must have a sharper decline than $\langle \tau \rangle_{LA}$. By using Eqn. 4-10, we can find various combinations of $D_{0,MBS}$, α_{MBS} , $D_{0,S}$ and α_S that satisfy the condition (i). To satisfy condition (ii), we will refer to Fig 4-4B & C, where we have established that the width of the energy well, which can be tuned by varying α , dictates how much the energy landscape tilts. Based on this observation, we propose that E_S must have lower α (broader well) compared to E_{MBS} while having a similar

D_o , which will result ΔE of the switch landscape to decrease more when f is applied. Since $\langle \tau \rangle$ is directly proportional to $\exp[\Delta E]$ (Eqn 4-10), $\langle \tau \rangle_{S^+}$ will have the sharper decline due to force compared to $\langle \tau \rangle_{LA}$. Consequently, we have determined the interaction parameters that will give us $\langle \tau \rangle_{LA}$ and $\langle \tau \rangle_{S^+}$ curves in Fig. 4-4A. For ligand-SBS interaction E_S , we don't have a strict design constraint, thus we select $D_{0,SBS}$ and α_{SBS} so that E_S has a similar stiffness to E_{MBS} . Interaction parameters are listed in Table 4-2.

Table 4-2 Tweezer interaction parameters

Interaction	D_o , kcal/mol	α , \AA^{-1}	σ , \AA
Ligand-MBS	6.5	10	2
Ligand-SBS	3	10	2.52
Switch	6.5	2	2

To validate the theory, we performed 1D constant force simulations, with the set of parameters in Table 4-2, for two serially connected potentials, harmonic and Morse, and measure the dissociation lifetimes $\langle \tau \rangle_{LA}$ and $\langle \tau \rangle_{S^+}$ (Fig. 4-5A). Note that we are not specifically simulating two serial Morse potentials but instead convert one of the Morse potentials to harmonic ($k_{Morse} = 2D_o\alpha^2$), making the converted interaction permanent. Since LA unbinding and S^+ events have exponentially distributed lifetimes, the trials with high lifetimes will be sampled less than their actual frequency. This conversion is necessary to improve sampling and prevent low lifetime trials of one event to hinder the sampling of high lifetime trials of the another. This way we still can observe the effects of a serial connection and yet sample the lifetime of the other potential (Morse) accurately. The simulation results mostly agree with the theory, except $\langle \tau \rangle_{LA}$ at small forces, where

the theory overpredicts the mean lifetime. We attribute this deviation to the harmonic approximation that we use to find k^b of E_{MBS} . The barrier of E_{MBS} has greater anharmonicity than the other three well/barrier curves (Fig. 4-5B), which will give us a slightly inaccurate measure of ω_{MBS}^b .

Unlike the open conformation events, HA unbinding and backward transition cannot be explained by a simple 1D potential like Morse, i.e. they have more complex 2D energy landscapes with contributions from E_S , E_{MBS} and moments created by f . Since Eqn. 4-10 can't be used to predict $\langle\tau\rangle$ from such a landscape, we extracted $\langle\tau\rangle_{S^-}$ and $\langle\tau\rangle_{HA}$ from the simulations by using Bell's theory.

4.5 Simulation Setup

To predict the lifetime of interactions in our model, MD simulations were carried out. In 2D tweezer model simulations, the initial configuration was such that the ligand was bound to the main binding site and the tweezer structure was in the open conformation. To describe intermolecular interactions, Morse potentials were used as summarized in Table 4-2. Tweezer members were treated as rigid and connected with harmonic springs, with $5000 \text{ kcal}/(\text{mol}\text{\AA}^2)$ stiffness, at their hinge points. To match the 1D energy landscapes in Fig 4-4B & C, the horizontal motion of the ligand was restricted. The base of the tweezer was fixed and a constant load in the vertical direction was applied to the ligand. In each simulation, the interaction energy between the ligand and the MBS was monitored. When the distance between them passed the cutoff distance, the simulation was terminated.

The simulations were run in the NVT ensemble at 300 K using a Langevin thermostat with a damping factor of 100 time steps. The adopted time step of 2 fs was found to be sufficiently small to ensure energy conservation. Force was applied after the equilibration of 5000 time steps. To obtain meaningful statistics, for each force value, 10000 1D and 5000 2D trials were performed.

4.6 Catch bond behavior

In the following simulations, we have adopted the interaction parameters predicted by the theory to yield catch bond behavior. A constant force, ranging from 5 to 200 pN, is applied on the ligand bonded to the tweezer and dissociation time of the ligand is recorded. As in Fig. 1.1, we will use the mean peak lifetime $\langle\tau\rangle_{peak}$ and corresponding critical force f_c to characterize our lifetime curve. Figure 4-6 shows that $\langle\tau\rangle_T$ starts from 28 ns and peaks at $f_c = 55\text{ pN}$ with $\langle\tau\rangle_{peak} = 63.5\text{ ns}$. After the peak, $\langle\tau\rangle_T$ monotonically decreases at larger forces. We can explain this behavior with the change in the probability of occurrence of each event at different force values. At small forces, most trials unbind at the LA state, exhibiting short lifetimes. At larger forces, the unbinding is delayed because more trials switch to the HA state and the backward transition becomes less likely, which prolongs τ_T of the individual trials. Note that $\langle\tau\rangle_T$ becomes greater despite $\langle\tau\rangle_{HA}$ decreasing with f . This is possible since S^+ transitions increase the probability of the system to be in the HA state, where $\langle\tau\rangle_{HA}$ is greater than $\langle\tau\rangle_{LA}$. However, when $f > f_c$, the probability of LA unbinding and S^+ events become comparable. The lifetime boost that comes from switching to the HA state becomes increasingly diminished as $\langle\tau\rangle_{HA}$ becomes smaller while S^+ probability remains roughly constant. The exponential decay of $\langle\tau\rangle_{HA}$ governs

the $\langle\tau\rangle_T$ curve for $f > f_c$, resulting in the decay in average lifetime. This is in line with experimental observations as shown in Fig. 1-1. To connect the simulation findings with existing models for catch bonds, the two-state model is used to fit the $\langle\tau\rangle_T$ curve, which has very good agreement with the simulation data. It should be noted that compared to the experimental data, lifetimes recorded in our simulations are shorter in magnitude. This is not a concern, since our aim here is not to match any specific experimental data set from biological systems. Rather, our goal here is capture the catch bond behavior quantitatively, in an artificial system loosely representing design features proposed for proteins.

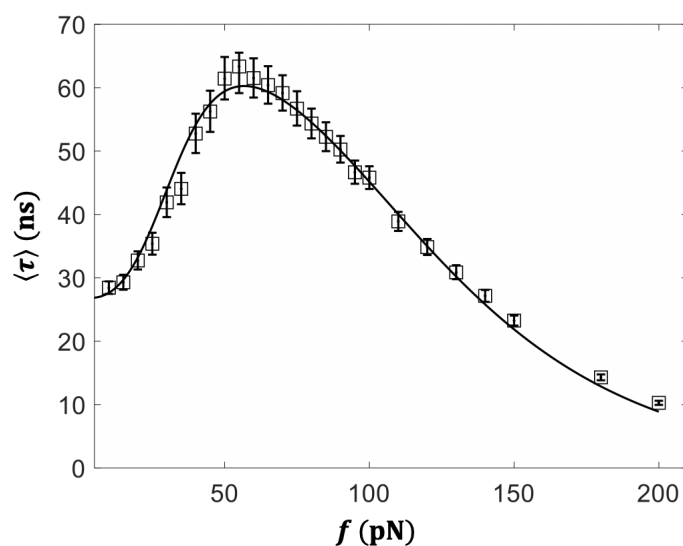


Figure 4-6 Mean lifetime $\langle\tau\rangle$ versus force f curve for tweezer-ligand complex. Symbols are from MD simulations and solid line is the corresponding curve from the two state model. The error bars represent 95% confidence interval, derived by the bootstrapping method.

In addition to the qualitative description of catch bond behavior, we now have a better understanding of the key parameters that control the shape of the $\langle\tau\rangle_T$ curve. For example, $\langle\tau\rangle_{peak}$ can be increased by increasing $D_{0,MBS}$ or $D_{0,SBS}$. Decreasing the temperature of the system, increasing the masses of the components or the damping coefficient would also result in

similar effects. In addition, increasing $D_{0,SBS}$ will decrease the slope of the $\langle\tau\rangle_T$ decay after f_c and increasing $D_{0,MBS}$ will shift the lifetime curve $\langle\tau\rangle_T$ upwards particularly in the low force regime, $f < f_c$. The location of f_c can be shifted to the right by increasing α_{SBS} , since this will decrease the steepness of the $\langle\tau\rangle_{HA}$ curve. Changes in $D_{0,S}$ and α_S are highly dependent on the shape of $\langle\tau\rangle_{HA}$ curve, therefore can shift f_c either way depending on the ligand-MBS interaction parameters.

In addition to the qualitative description of catch bond behavior, we now have a better understanding of the key parameters that control the shape of the $\langle\tau\rangle_T$ curve. It can be inferred from Eqn. 4-10, that the transition rates depend exponentially on energy barriers and temperature. Thus, we predict $\langle\tau\rangle_{peak}$ can be increased by increasing $D_{0,MBS}/D_{0,SBS}$, or decreasing the temperature of the system. We validated these predictions with related simulations. As shown in Figure 4-7, increasing $D_{0,SBS}$ and decreasing temperature result in larger $\langle\tau\rangle_{peak}$. Increasing the masses of the components or the damping coefficient would also have similar effects. There are two additional things to note in Fig. 4-7A. First, we do not observe a lifetime peaks for the curves with $D_{0,SBS} = 1$ and 1.5 kcal/mol. This indicates that the delay in unbinding created by the trials that switch to HA state does not compensate the exponential decay of the lifetime of the rest of the trials with LA unbinding. Second, the location of f_c is same for curves with a peak. This is expected since the location of f_c is primarily governed by the convergence of $\langle\tau\rangle_{LA}$ and $\langle\tau\rangle_{S^+}$, which does not depend on secondary interaction parameters. The location of f_c can be shifted to the right by increasing α_{SBS} , since this will decrease the steepness of the $\langle\tau\rangle_{HA}$ curve. Moreover,

changes in $D_{0,S}$ and α_S are highly dependent on the shape of $\langle\tau\rangle_{HA}$ curve, and therefore can shift f_c either way depending on the ligand-MBS interaction parameters.

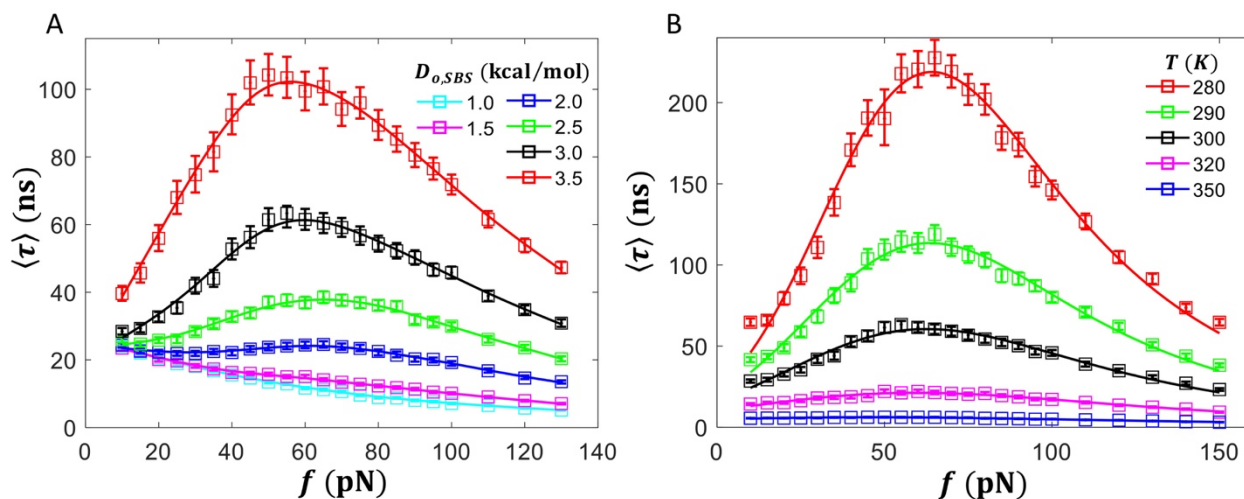


Figure 4-7 Effects of key parameters on mean lifetime $\langle\tau\rangle$ versus force f curve of tweezer-ligand complex
 A) ligand-SBS interaction energy well depth ($D_{0,SBS}$) and B) temperature. Symbols are from MD simulations and the curves are generated with the fitting function $\langle\tau\rangle(f) = cf^a \exp[-f/b] + d \exp[-f/e]$. The error bars represent 95% confidence interval, derived by the bootstrapping method. Black represents simulations and the corresponding curve fit with the set of parameters in Table 4-2.

4.7 Conclusion

In this study, we have demonstrated that a simple mechanical design based on a tweezer-like mechanism can exhibit catch bond characteristics under thermal excitations. The essential feature of our tweezer systems is the design of the switch, which has different force-dependent kinetics relative to the ligand unbinding. By using kinetic theory combined with theory of vibrations, we found that when energy landscapes of the switch interaction E_S and the ligand-MBS interaction E_{MBS} are carefully tuned, the ligand lifetime will increase with greater applied force, which constitutes the counterintuitive feature of catch bonds. The increase in lifetime

occurs, because switch landscape tilts more strongly under force relative to the ligand-main binding site landscape, which brings together the transition and the unbinding lifetime-force curves and results in greater dwell time in the closed conformation, that is, the high-affinity state. MD simulations based on this design verified the theoretical arguments, although some differences in the quantitative results were observed owing to the more complex, nonlinear nature of the dynamic model.

The tweezer design provides a basic structural explanation for the catch bond behavior. However, we can reach to broader design guidelines that can be applied to other geometries, if we analyze our design in the context of allostery. At a glance, the minimal nature the serial two-degree-of-freedom system, with two vibration modes alone may not seem particularly relevant to proteins. However, it can be argued that the “switch” is analogous to a soft vibrational mode associated with low frequency conformational dynamics governed by large modal masses and low modal stiffness, whereas ligand interactions relate to a high frequency vibrational mode stemming from a light-weight molecule bound tightly to a binding site. Indeed, it has been shown that elastic networks that exhibit allostery have a single soft region constrained by rigid regions ⁸⁹⁻⁹³. Moreover, displacements in the soft region of allosteric materials initiates conformational changes, which alters the function and dynamics of the structure. The tweezer design meets both of these specifications, since it has a low stiffness switch that is connected to rigid members and the motion of the switch controls the conformational transitions of the tweezer. Thus, implementing a soft region linked to rigid regions in geometries is a valid method to achieve desired force induced strains that lead to conformational changes. The soft “switch” regions would likely employ material (e.g. Morse-like molecular linkages) or geometric nonlinearities (e.g. snap through

instabilities⁹⁴) to trigger large displacements beyond a certain stress level. Most importantly, for the system to exhibit catch bond behavior, these changes must be the part of the mechanism that increases the ligand affinity, e.g. formation of new interactions in the tweezer design. With these guidelines, catch bond geometries that are templates for synthetic polymer design can be created. A promising building block for such geometries may be DNA linkers, since their shape and interactions can be engineered to a wide range of structures seen in and beyond nature ⁹⁵. DNA bricks ⁹⁶ or origami ⁹⁷ that is used in many 2 and 3D structures is a possible direction for future work in manufacturing a catch bond mechanism.

We believe that synthesis of tunable catch bond linkages between molecules will have major implications in material science, especially in addressing the trade-off between strength and reconfiguration ⁹⁸, two diametric material properties that are primarily governed by intermolecular interactions ⁹⁹. A reversible interaction that becomes strong when it is under large mechanical stresses might be the key to manufacture materials systems that resist deformation under impact, yet offer self-healing and greater processability at low force levels.

Chapter 5 - Designing nanoparticles with adhesin-inspired interfaces

In this chapter, we talk about our X-shaped nanoparticle design with intrinsic catch bonding ability under thermal excitations. These nanoparticles self-assemble via weak bonds and form fibers via their primary binding sites. In presence of tensile force, the particles can change shape and transition to a high-affinity state fostered by additional interactions between their originally buried secondary binding sites. Based on the energy landscape insights from the previous chapter, the transition between the equilibrium and high-affinity states is controlled by a precisely calibrated Morse potential based switch, which can open/close in presence/absence of the tensile force on the system. We present MD simulations of tensile pulling on a nanoparticle dimer to demonstrate catch bond functionality. We then illustrate fiber formation via self-assembly, where we show that archetypal catch bond feature is retained, with fibers exhibiting greater lifetime upon application of larger tensile force. Portions of the text and figures within chapter are reprinted or adapted with permission from Dansuk and Keten, *Nature Comm.* 2021¹⁰⁰.

5.1 X-shaped particle design

To achieve intrinsic catch bonds between particles, we propose a design that incorporates an X-shaped nanoparticle with a hidden binding site that becomes exposed upon application of tensile force, and a switch that controls the likelihood of this conformational transition. The X-shaped nanoparticle is a symmetric structure consists of rigid members that are connected with hinge joints as shown in Fig. 5-1A. The nanoparticle has four binding sites at the ends of its arms (red beads) and two binding sites along the central vertical axis (blue beads). In this work, we will refer to red beads as primary binding sites (PBS) and the blue beads as secondary binding sites

(SBS). Grey beads have steric repulsion with all the beads to create inaccessible volume determining the shape of the nanoparticles, which influences the morphologies formed via self-assembly by providing shear resistance to the fiber and enabling correct attachment during the self-assembly process. Arms of the structure can rotate about the center, thus the two halves of the structure have open and closed conformational states. It should be noted that there is no angle constraint between the halves, thus they can open and close independently from each other.

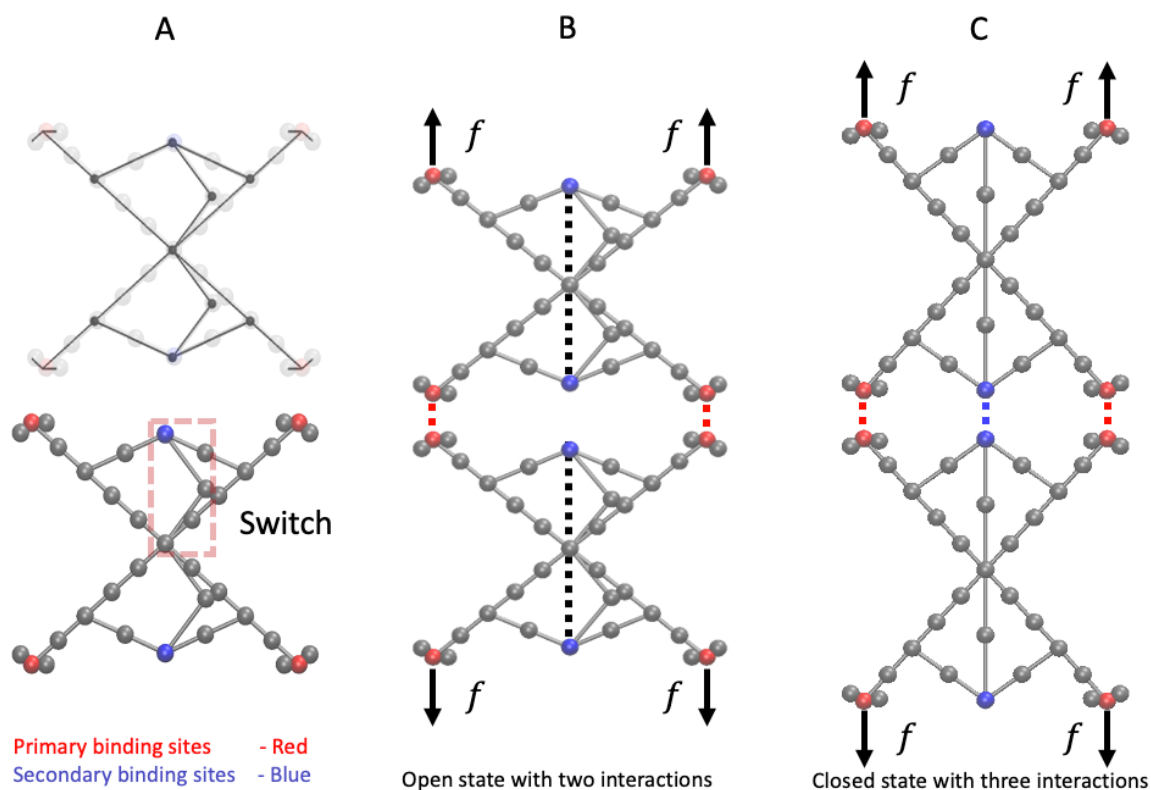


Figure 5-1 Schematics of X-shaped nanoparticles. A) Each nanoparticle is formed by rigid members connected with hinge joints (grey nodes). Each nanoparticle has primary binding sites (PBS, red), secondary binding sites (SBS, blue) and switch mechanisms. The hinge-like switch is highlighted with a dashed box. Grey beads have steric repulsion to create inaccessible volume determining the shape of the nanoparticles. B) When two nanoparticles are in the open state, their switch members are angled and they can form a dimer via two intermolecular interactions (red dashed lines). C) When two nanoparticles transition to the closed state, the switch members become straight and the dimer forms an additional intermolecular interaction (blue dashed line). The switch interactions and applied external forces are indicated by black dashed lines and black arrows respectively.

To better understand how X-shaped nanoparticles interact with each other in different conformational states, we focus on a preassembled dimer. As shown in Figure 5-1B, when nanoparticles are in the open conformation, complementary PBS are connected by non-bonded interactions (red dashed lines). In this equilibrium bound state, SBS interaction is negligible, since

the intermolecular distance between SBS is large. The force-dependent transition between the two conformations is controlled by switches in both the upper and lower halves of the nanoparticle. The switch consists of a two-member hinge with a pairwise interaction between its two free ends (blue SBS bead and black bead at the symmetry axes). In the open conformation, the switch members are angled due to the pairwise interactions as shown with black dashed lines in Fig. 5-1B. However, these pairwise interaction can break due to external forces. In that case, since there is no other force between the members, system elongates in the direction of the force and the switch members straighten and become linear (Fig. 5-1C). Straightening of the switch moves the SBS upwards and drives the arms inwards, enabling interaction between the complementary SBS (blue dashed line). The new interaction increases the total binding energy between the nanoparticles, giving the dimer a higher affinity in the closed conformation. Thus, in context of unbinding, dimers in the open conformation are in their low affinity (LA) state and dimers in the closed conformation are in their high affinity (HA) state. In conclusion, these X-shaped nanoparticles have all three key catch bond features established earlier: they have two (open and closed) conformations, force regulates the breaking and reforming of switch interactions controlling the transition between the conformations, and SBS interaction formed upon transition to the closed conformation increases the affinity of the particles.

The X-shaped nanoparticle consists of 10 members that are connected with hinge joints. In Fig. 5-2, member types a,b and c indicate the structure members and type d indicate the switch members. The bonded interactions between the beads are modelled as harmonic springs, with $5000 \text{ kcal}/(\text{mol}\text{\AA}^2)$ stiffness. To ensure that the members are straight, a harmonic angle

potential with a spring coefficient of $1000 \text{ kcal}/(\text{mol radian}^2)$ is used. Each bead has a mass of 100 g/mol .

We described that in the open conformation, the SBS are closer to the center of the particle compared to the PBS. In closed conformation, both PBS and SBS are on the same horizontal line. Here, we will describe how we determine the dimensions of the members to satisfy this relation. In the open conformation, the switch is angled and in equilibrium, thus the distance h between the SBS and the center of the particle equals to $x_{o,S}$, the equilibrium distance of the switch interaction. The intramolecular angle in the open conformation, θ_{LA} should satisfy the following relation

$$\cos(\theta_{LA}) = \frac{a^2 + x_{o,S}^2 - b^2}{2ah}. \quad (5-1)$$

When $\theta = \theta_{LA}$, The difference in vertical distance of PBS and SBS with respect to the center of the particle is given by

$$\Delta x = (a + b) \cos \theta_{LA} - x_{o,S}. \quad (5-2)$$

When two nanoparticles interact in their open state, complementary PBS of the dimer are at the equilibrium distance of the PBS interaction $x_{o,PBS}$ and the SBS are at a distance of $x_{o,PBS} + 2\Delta x$.

During the open to closed conformation transition, the interaction of the switch breaks, and the switch members become straight. At this point, h equals to $2d$, i.e. the length of the two switch members. The intramolecular angle at the closed conformation, θ_{HA} should satisfy the following relation

$$\cos(\theta_{HA}) = \frac{a^2 + (2d)^2 - b^2}{2ah}. \quad (5-3)$$

Hence, for PBS and SBS to be on the same horizontal plane, the following relation must be true at θ_{HA}

$$h = (a + b) \cos \theta_{HA} = 2d. \quad (5-4)$$

The dimensions used in this work are listed in Table 5-1. In conclusion, by varying the dimensions, we can control the changes in the intermolecular interactions between the conformational states.

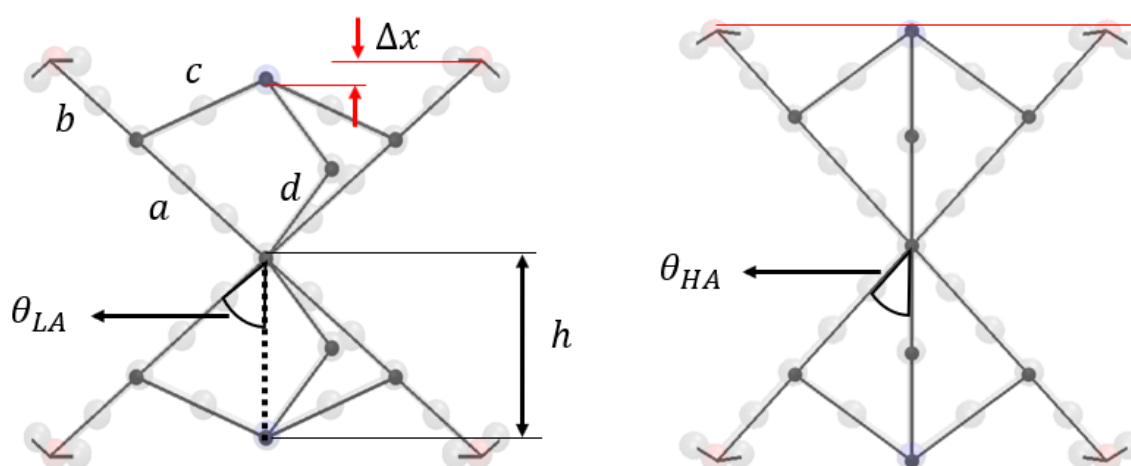


Figure 5-2 X-shaped nanoparticle geometry and its dimensions A) Open conformation B) Closed conformation

Table 5-1 Nanoparticle Dimensions

Member	Value
a	3.6 Å
b	2.4 Å
c	3.0 Å
d	2.24 Å

5.2 Simulation parameters

The MD simulations were run in the NVT ensemble at 150 K using a Langevin thermostat with a damping factor of 100 time steps. The adopted time step of 2 fs was found to be sufficiently small to ensure stability. For tensile test simulations, force was applied after an equilibration of 5000 time steps. In each simulation, constant forces ranging from 140 to 280 pN is applied to the end points of the dimer at LA state (as shown in Figure 1B) and the interaction energies between the nanoparticles were monitored. To obtain meaningful statistics for each force value, 10,000 trials were performed.

We used replica-exchange MD simulations (REMD) to study the self-assembly of 100 open conformation particles in a 200x200 nm² periodic boundary box. First, nanoparticles are considered as circles and placed randomly inside the simulation box without any overlaps. Next, they are given a random rotation. Multiple simulations (10 replicas) covering a temperature range of 150 to 180 K are performed in parallel. Simulations were run for 10⁷ time steps. Exchanges between adjacent replicas were attempted every 10⁴ time steps. The temperature distribution was chosen such that a constant acceptance ratio of 20% occurred between all replicas. The analysis of

the simulations was carried out over frames the baseline trajectory, i.e. replica corresponding to 150 K.

5.3 Binding energy landscapes for catch bond behavior

In our study, Morse potentials are used to represent the primary binding site interactions (E_{PBS}), secondary binding site interactions (E_{SBS}) and the interactions that makes up the switch (E_{S}).

To reproduce the characteristic catch bond lifetime curve, the mean lifetime of the dimer $\langle\tau\rangle_2$ must increase when a tensile force is applied. In our previous work with a stationary mechanical model¹⁰¹, we have identified two conditions that result in the force-enhanced lifetimes seen in catch bonds. First, at small forces most trials should result in LA unbinding of the dimers, and at large forces, most trials should transition to the HA state before LA unbinding can occur. Second, the mean HA unbinding lifetime $\langle\tau\rangle_{\text{HA}}$ must be longer than the mean LA unbinding lifetime $\langle\tau\rangle_{\text{LA}}$. Satisfying these two conditions will result in a higher percentage of trials unbinding at larger lifetimes, which guarantees the increase in $\langle\tau\rangle_2$ as the pulling force increases.

To satisfy the first condition, we determined that the switch should have a deeper and a broader energy landscape than the binding site landscape¹⁰². At zero or small forces, the switch lifetime should be longer than the LA unbinding lifetime to have the majority of the pulling trials result in dimers separating in the LA state before transitioning to the HA state. According to Kramer's theory⁴³, $\langle\tau\rangle$ is directly proportional to $\exp[D_0]$, thus by selecting the depth of the energy well of the switch ($D_{0,\text{S}}$) to be greater than depth of the energy well of the primary binding sites ($D_{0,\text{PBS}}$), we obtain a higher switch lifetime at small forces. Note that in catch bonds, conformational changes occur over relatively long time scales in the absence of force, which is also why they are

difficult to observe with MD simulations^{11,33}. This suggests that there is a large barrier to these conformational changes, which is in qualitative agreement with our choice for $D_{0,S}$. On the other hand, the LA unbinding lifetime should be longer than the switch lifetime to have majority of the pulling trials result in HA state transition at large forces. This transition between the relative lifetimes will be controlled via tuning the width of the energy landscapes of the system. Note that the tilting of the energy landscape by force is sensitive to the distance to the transition state, or the width of the landscape when well depth is kept constant. Therefore, E_S must have lower α (broader well) compared to E_{PBS} , which will result in the energy barrier of the switch landscape to decrease rapidly when greater tensile force is applied. Hence, the switch lifetime declines more sharply when subjected to force compared to the LA unbinding lifetime. Based on this condition, we have determined the parameters for E_S and E_{PBS} , which are listed in Table 5-2. For an improved understanding of this response, we performed molecular dynamics simulations of tensile pulling of the dimer. The simulations were terminated (i) when the particles dissociate (LA unbinding event) or (ii) when the switch interactions dissociate (LA to HA state transition event). Figure 5-3 shows fraction of these two events at various forces. At low forces, the majority of the trials result in dimers separating in the LA state before the HA state transition, e.g. 90% of the trials at 140 pN. This fraction decreases monotonically as the constant pulling force is increased, e.g. to 3% at 280 pN. The decrease from 90% to 3% agrees with the first catch bond condition listed above.

Table 5-2 Nanoparticle interaction parameters

Interaction	D_0 , kcal/mol	α , \AA^{-1}	x_0 , \AA
Primary, E_{PBS}	2.8	10	1.5
Switch, E_S	3.4	3	3.5

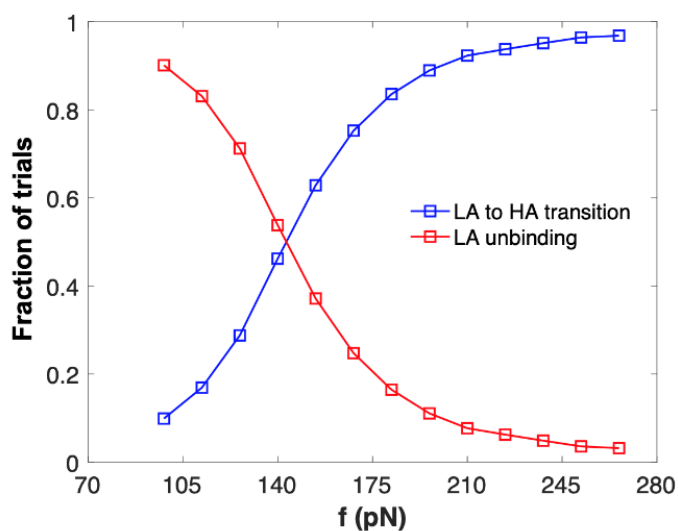


Figure 5-3 Force dependence of the fraction of trials for the dimer to dissociate in the LA state and dimer to transition from the LA to the HA state. LA unbinding is shown in red and LA to HA transition is shown in blue.

The second condition we have specified is based on the notion that the formation of the SBS interaction increases the unbinding energy barrier. Since the unbinding barrier is higher, $\langle\tau\rangle_{\text{HA}}$ will be greater than $\langle\tau\rangle_{\text{LA}}$. In the following simulations, we perform tensile pulling on nanoparticle dimer to analyze the effect of secondary interaction (E_{SBS}) on dimer lifetime. We select α and x_0 of E_{SBS} to be the same as the primary interaction parameters, but varied $D_{0,\text{SBS}}$ between 0 to 1 kcal/mol. The simulations were terminated when the particles dissociate (LA and HA unbinding event) and dissociation lifetimes of the dimers are recorded. As seen in Figure 5-4, in the absence

of secondary interactions ($D_{0,SBS} = 0$), the lifetime of the dimer exponentially decreases with force (dashed line), which is expected for typical chemical interactions/bonds¹⁰³. For all the nonzero $D_{0,SBS}$ cases, we use peak lifetime $\langle \tau \rangle_{\text{peak}}$ and corresponding critical force f_c to characterize the lifetime simulation results. Figure 5-4 shows that $\langle \tau \rangle_2$ of all the solid curves have peaks around $f_c = 175$ pN. After the peak, $\langle \tau \rangle_2$ monotonically decreases at larger forces. As expected, when the E_{SBS} is increased, the overall lifetime for the dimer increases, i.e. the higher the secondary interaction energy, the higher the increase in unbinding energy barrier.

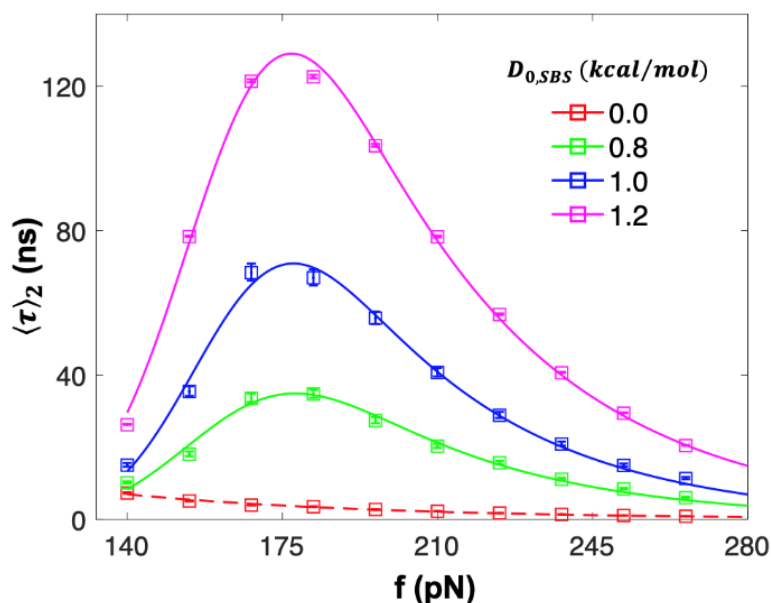


Figure 5-4 Effects of secondary interaction energy well depth ($D_{0,SBS}$) on mean lifetime $\langle \tau \rangle$ versus force f curve of a nanoparticle dimer. Symbols are from MD simulations and the curves are generated using an exponentially modified Gaussian distribution fitting function. The error bars represent the 95% confidence intervals, derived by the bootstrapping method.

HA and LA unbinding pathways described above can be represented as a multidimensional energy landscape that depends on interparticle distance x and intraparticle angle θ . Figure 5-5A displays selected snapshots from the simulations which show the unbinding (green, orange) and

switch (black) pathways. Since the upper and lower halves of the nanoparticle can rotate independently, interaction of the dimer pair will be governed by the halves forming the interface. Thus, two switches, each having energy of E_S , control the change in θ . The transition energy landscape (black curve in Fig. 5-5B) has two local minima, demonstrating the biphasic nature of the dimer. When θ decreases to 42° , switch members are straight and any force to deform the nanoparticle will be carried by these members, which are fairly rigid and thus prohibit further variations in the geometry. Deforming the system beyond this point requires a large energy input, thus, there is a big surge in the transition energy below 42° . Similarly, above 50° since the distance between switch elements is less than the Morse interaction equilibrium distance of E_S ; short range repulsion term of the potential dominates, and we see an increase in energy. Moreover, the force-induced decrease in θ brings SBS closer and a new interaction is formed (red curve). The binding energy between the particles is defined as $2E_{PBS} + E_{SBS}$, incorporating the three possible interactions between the particles. The energy landscapes for the unbinding pathways are shown in Figure 5-5C. Since E_{SBS} increases in the HA state, HA unbinding has a higher energy barrier than LA unbinding.

In the end, the two conditions we specified result in catch bond behavior at the nanoparticle interface. At small forces, most trials unbind in the LA state, exhibiting short lifetimes. At larger forces, the unbinding is delayed because more trials switch to the HA state with the associated additional interactions and the backward transition becomes less likely, which prolongs τ_2 of the individual trials. It should be noted that the temperature and the force ranges used in the simulations are arbitrary and do not aim to reproduce any particular experimental setup. Our goal here is to demonstrate the catch bond behavior in generic nanoparticle systems. As long as the two

conditions we have specified are satisfied, it is possible to tune the system to exhibit a lifetime peak at arbitrary forces ¹⁰¹.

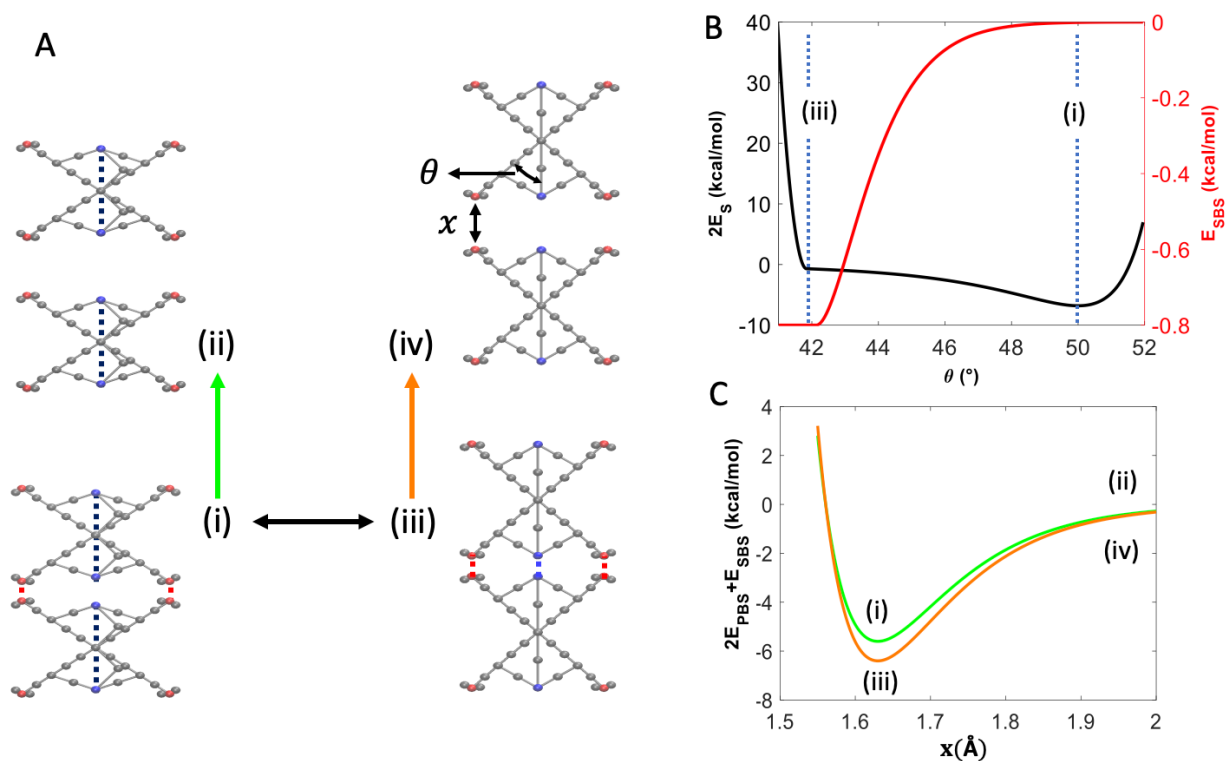


Figure 5-5 X-shaped nanoparticles form a biphasic system with two unbinding pathways. **A)** Snapshots (i) and (iii) are the LA state and HA state respectively. Snapshots (ii) and (iv) are the unbound dimers. The black line indicates the transition pathway of the dimer between its LA and HA states. The green line is the LA unbinding pathway and the orange line is the HA unbinding pathway. The reaction coordinates, namely interparticle distance x and intraparticle angle θ are marked in the snapshot (iv). **B)** Energy landscapes for the LA to HA state transition as a function of intraparticle angle θ . The transition energy landscape (black curve) is between the complementary halves of two nanoparticles and is the sum of two switch interactions. E_{SBS} (red curve) shows that in the LA state, SBS has no contribution to the interaction between the particles, however, in the HA state complementary SBS's interact. **C)** Energy landscapes for the LA to HA unbinding as a function of interparticle distance x . The curves follow the same color code as the pathways. HA unbinding has a larger barrier due to E_{SBS} contributions.

5.4 Force history dependence of the system

Since the dimer can switch between and unbind at different conformations depending on the instantaneous value of the force, the catch bond lifetime depends on the loading history. Indeed, effects of loading history on catch bond lifetimes are investigated in FimH and P-selectin proteins via force-ramp experiments, where a probe is used to pull apart the protein-ligand pair under constant loading rate^{104,105}. These experiments show that protein-ligand interactions break at low or high forces but are strongest at an intermediate range of force. It is also observed that as the loading rate is increased, the breaking events occur more frequently at higher forces, thus at faster loading rates low-force rupture events are less likely to occur. To investigate these effects, we performed simulations where the tensile force on the dimer is increased at a constant loading rate, and we record the magnitude of the force when the bond breaks, F_b . The histogram of F_b for different loading rates is shown in Fig. 5-6. The curves exhibit a bimodal distribution, with one peak at low forces and another at high forces. This shows that, for our system, majority of the pulling trials break at low and high forces, but not at in between intermediate range, which is in agreement with force-ramp experiments. Similar to the experiments, we observe that as we increase the loading rate, we observe an increase in the high force peak in the histogram and decrease in the low force peak. Lastly, overall curves shift to the left with the increasing loading rate. This is expected since bond strengths are generally increased by the loading rate¹⁰⁶.

It should be noted that the simulation loading rates are five orders of magnitude higher than the experimental loading rates of single molecule force spectroscopy experiments on catch bond systems. In our system, due to computational time restrictions, we have chosen the energy barriers of the particle interactions to be lower than the energy barriers of protein-ligand complexes to

efficiently sample bond breaking events. Moreover, to reduce the noise, these simulations are performed at a lower temperature than the single molecule force spectroscopy experiments. As a result, our event lifetimes are significantly shorter than catch bond lifetimes seen in experiments. Consequently, higher loading rates have to be used to reach the critical force governing low to high affinity transition.

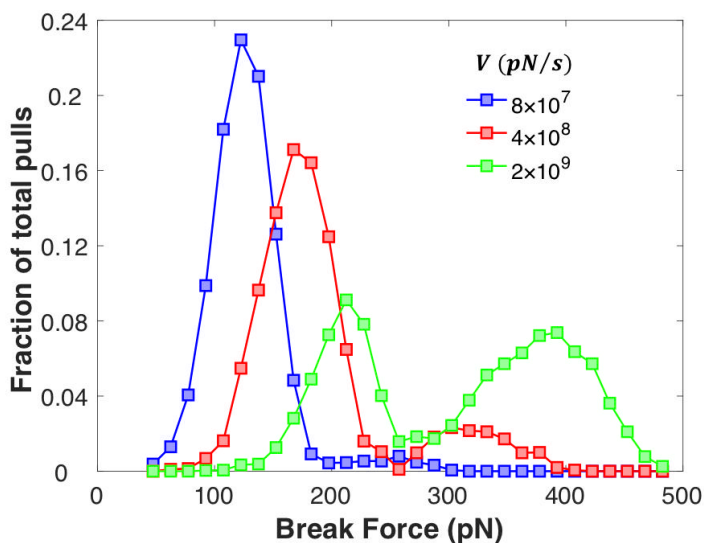


Figure 5-6 Break force histograms for X-shaped nanoparticle dimer under constant loading rate. The data points are expressed as fractions of total pulls (10,000 trials) for each of the three loading rates V (blue, red and green).

5.5 Self-assembly of nanoparticles

In order to investigate the self-assembly of the nanoparticles, we have generated unbiased random initial configurations for 100 open conformation particles and ran simulations to sample fiber formation trajectories. Replica exchange method is used to perform the self-assembly simulations, which enables us to increase the effective simulation time of MD simulations by improving sampling of relevant areas of the assembly path. In the simulations, nanoparticles interact from PBS and successfully form fibers with lengths ranging from 2 to 10 particles. None of the nanoparticles transition to closed conformation because the timescale of the open to closed conformation transition in the absence of force is remarkably longer than unbinding and self-assembly lifetimes. Note that during the trajectory, the simulation temperature varies over time as swaps take place between replicas.

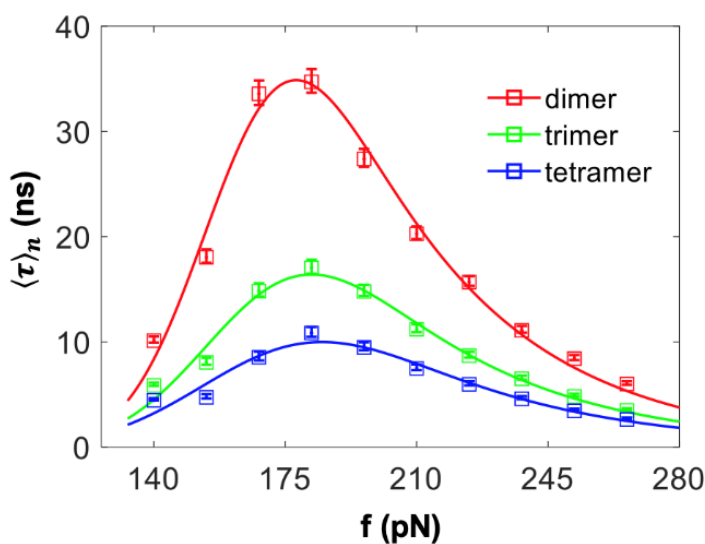


Figure 5-7 Mean lifetime $\langle \tau \rangle$ versus force f curves for self-assembled fibers at varying degrees of polymerization. Symbols are from MD simulations and the curves are generated with an exponentially modified Gaussian distribution fitting function. The error bars represent 95% confidence interval, derived by the bootstrapping method.

5.6 Lifetime scaling of self-assembled fibers

With the aim of determining whether the catch bond behavior that we observed in dimers is retained in longer self-assembled fibers, we run tensile pulling simulations of fibers with various number of particles. For the simulations, D_0 of the E_{SBS} is chosen to be 0.8 kcal/mol. Figure 5-7 shows that catch bond behavior is present regardless of fiber length. There are lifetime peaks at $f_c = 175 \text{ pN}$ for all lengths, even though $\langle \tau \rangle_{\text{peak}}$ of the fiber decreases as the number of subunits increases. The following observation can be explained with probability theory considering a serial arrangement of interactions. The probability that a dimer exposed to a constant force f is still intact after a time t is given by

$$P_2(F) = e^{-r(f)t}, \quad (5-5)$$

where $r(f)$ is the rate of dissociation of the dimer. The expected lifetime can be calculated using

$$\langle \tau \rangle = - \int_0^{\infty} \frac{dP}{dt} t dt. \quad (5-6)$$

At a constant pulling force, r will be constant, thus the lifetime of the dimer $\langle t \rangle_2$ is $1/r$ using Eqn. 5-6. Note that r , P and $\langle t \rangle$ are all functions of pulling force. Similarly, we can calculate the probability of the three-particle fiber (trimer) being intact, P_3 . Here, we make two assumptions. First, the dissociation events (unbinding of particles 1, 2 or 3) are independent from each other. Therefore, P_3 will be a product of the probability of interaction between first and the second subunit being intact and probability of interaction between second and the third subunit being intact. Second, the force along the fiber, i.e. tilting on all the energy landscapes, is the same. Therefore, probability of unbinding is the same for all subunits, giving us the relation

$$P_3 = P_2 \cdot P_2 = e^{-2rt} \quad (5-7)$$

Using Eq. 5.6, the lifetime of the trimer is found to be

$$\langle \tau \rangle_3 = \frac{1}{2r} = \frac{\langle t \rangle_2}{2}. \quad (5-8)$$

The following relation can be expanded for n-mer structure, therefore the expected lifetime of n-mer fiber will be

$$\langle \tau \rangle_n = \frac{\langle t \rangle_2}{n-1}. \quad (5-9)$$

With $\langle \tau \rangle_2$ known, we predict the lifetimes of trimer and tetramer fibers using Eqn. 5-9, which match with the curves in Figure 5-7. Thus, we have shown that, we can predict the fiber lifetime at any arbitrary degree of oligomerization.

5.7 Conclusion

Inspired by the mechanical behavior of biological catch bonds, we developed a model to probe how introduction of such catch bonds into nanoparticles could lead to fibers with intrinsic self-strengthening properties when subject to extreme stresses. Our analysis proves that nanoparticles with intrinsic catch bonds will exhibit force-enhanced lifetimes when self-assembled into fibers, and in dimer state exhibit stronger binding under larger mechanical stresses. Shape changing, or shape-shifting nanoparticles are mostly used in medical applications, such as drug delivery, and their potential in mechanical applications remains to be realized. This work is a demonstration of not only a shape-changing nanoparticle, but also a synthetic catch bond system as a new class of building block for the fabrication of ordered structures. While the structure we study is specific, the concept and our analysis methodology are broadly applicable to assemblies where buckling, snap-through or breaking of weak internal bonds (e.g. in foldamers) can facilitate shape-changes that alter interparticle interactions. We hope that this work serves as a starting point for synthetic chemists aiming to design such architected nanoparticles to generate emergent

functional materials through self-assembly. We also note that shape-changing colloids are another scalable system where the concept of biphasic particles may be utilized to tune interparticle interaction strengths with force¹⁰⁷.

As our nanoparticle model is conceptual, we shall end our discussion by presenting a possible path, scaffolded DNA origami⁹⁷, to expand this model into synthetic systems. In these DNA structures, stiff double-stranded DNA (dsDNA) and flexible single-stranded DNA (ssDNA) components are integrated to create mechanical devices capable of precise motions¹⁰⁸. Molecular machines fabricated in literature, i.e. hinges and sliders and especially scissors, share many structural similarities with our X-shaped nanoparticle¹⁰⁹. In Chapter 7, while discussing future work we will have a provide compatible DNA origami structure based on X-shaped particle design. Lastly, we note that this is only one of the paths to make catch bonds; any thermalized microparticle or granular system with constituents having shape-shifting or contact modulation capability can in principle exhibit catch bonding interfaces when properly tuned.

Chapter 6 - Establishing catch bond designs through cooperativity of tether links

In this chapter we will present an alternative mechanism for the catch bond behavior that specifically addresses the question of how catch bonding interfaces may be realized in nanoparticles interconnected with polymeric tethers. Indeed, this has been the setup envisioned in earlier papers that looked at the properties of particle networks forming catch bonds, but how polymeric tethers must be designed to achieve this feature has remained obscure^{110–112}. In Chapter 4 and 5, we look at designs with intrinsic catch bonding ability, where there is an allosteric pathway for structure to change conformation to attain higher affinity binding. Here, we will focus on a polymer grafted nanoparticle interface, which differs from previous systems in that the nanoparticle core is rigid and the adhesion itself does not form catch bonds. We will show that it is possible to recapitulate catch bond behavior by controlling coordination between the grafted elements.

In the first section, we present our molecular design that results in catch bonding interfaces between polymer grafted nanoparticles. Our design relies on two polymer tethers with equal contour length that attach to one of the particles with adhesive interactions, where one tether has a compliant loop stabilized by weak bonds. Next, we present results of molecular dynamics simulations of tensile pulling of particles to illustrate that addition of a loop with tuned stiffness results in a transition from uneven load distribution to shared load distribution on the adhesive polymer tethers under increasing force^{113,114}. Shared load distribution has longer lifetime, thus the system demonstrates catch bond behavior. Lastly, we discuss our attempt to analytically represent the catch bond behavior of the two tether system.

6.1 Two tether geometry

In this work, we take a minimalistic approach to designing interfaces that replicate the feat of catch bonds. Instead of employing complicated folded macromolecules, we utilize linear polymer tethers covalently grafted onto a nanoparticle and interacting with another particle with weak adhesive interactions that we call an *adhesin* interaction. Each interface consists of a linear chain and a sister chain of the same contour length, having the same degree of polymerization. One of these chains forms a short *loop* due to weak self-interactions of the chain, whereas the other is devoid of such interactions. These design elements, consisting of weak adhesin and loop interactions, are quite universal. An adhesin interaction can be formed simply from any non-covalent secondary interaction, such as hydrogen bonds or electrostatics. Loops are ubiquitously employed in biomolecules for creating complex 3D tertiary structures. Examples of biomolecular and polymeric loop structures that can reversibly unfold under thermal excitations or mechanical force are illustrated in Figure 6-1. Functionally, loops facilitate sacrificial bonds and hidden length in proteins like titin, which is vital for muscle elasticity¹¹⁵. In DNA, looping is accomplished by means of two DNA binding domains per Lac repressor molecule, allowing it to bind two of its specific DNA sites simultaneously, with the intervening DNA adopting a looped conformation¹¹⁶. RNA molecules can assemble a simple hairpin that can switch between two distinct folded and unfolded conformations¹¹⁷. Recent experimental advances in synthesizing foldamer¹¹⁸ and DNA containing gels¹¹⁹ also make it possible to synthesize looped polymers. Most notably, modular polymers that mimic the unfolding and refolding of the protein titin have been synthesized and were demonstrated to exhibit enhanced mechanical properties^{120,121}.

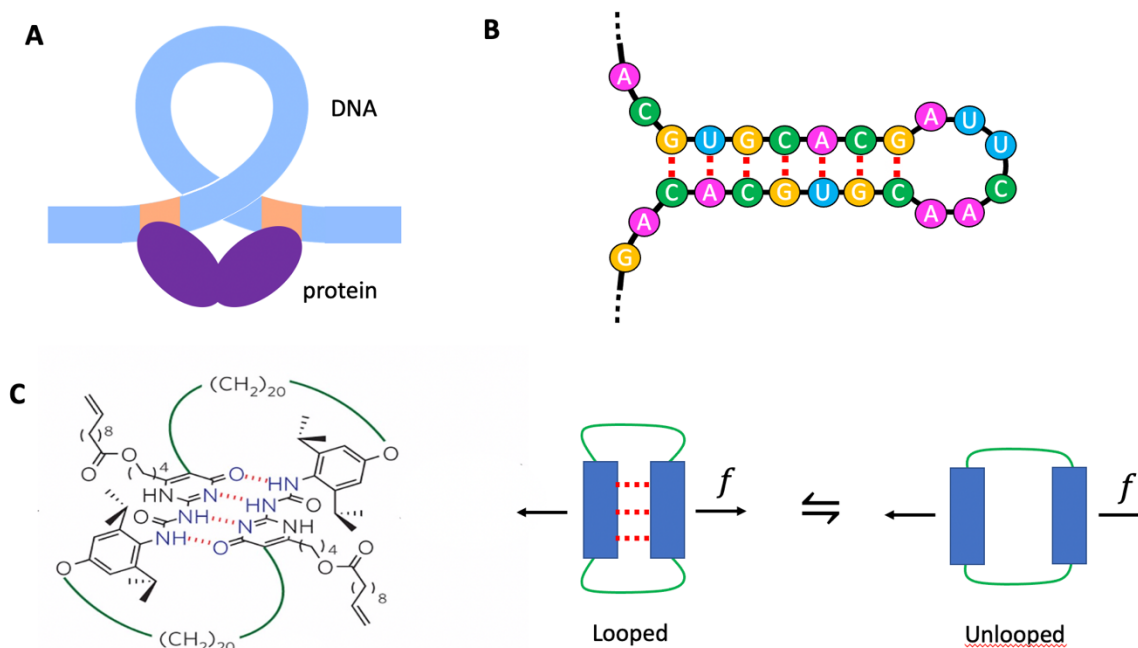


Figure 6-1 Loop motif in biological and biomimetic systems A) protein-mediated DNA looping B) mRNA hairpin loop C) biomimetic design of a modular polymer that is inspired by titin and can reversibly unfold. Red dashed lines represent hydrogen bonds.

With these two universal elements in mind, we envisioned a molecular construct where two surfaces (e.g. representing particles) would be connected together via two flexible, adhesive tethers, as shown in Figure 6-2A. A coarse-grained representation of the system is shown in Figure 6-2B. Tethers are covalently grafted onto one surface, and they weakly attach to the other surface with an adhesin interaction in the form of a regular slip bond. While both tethers have the same contour length ($L_I = L_{II}$), one of the tethers can form a loop that will ‘store’ some of its length. The loop is also stabilized by ordinary weak slip bonds. In equilibrium, the minimum energy configuration of this system is such that the folded tether is taut and exerts greater force that keeps the two surfaces together under thermal undulations, while the tether without the loop has slack and carries much less force. In our design, the tethers are short and entropic elasticity is expected

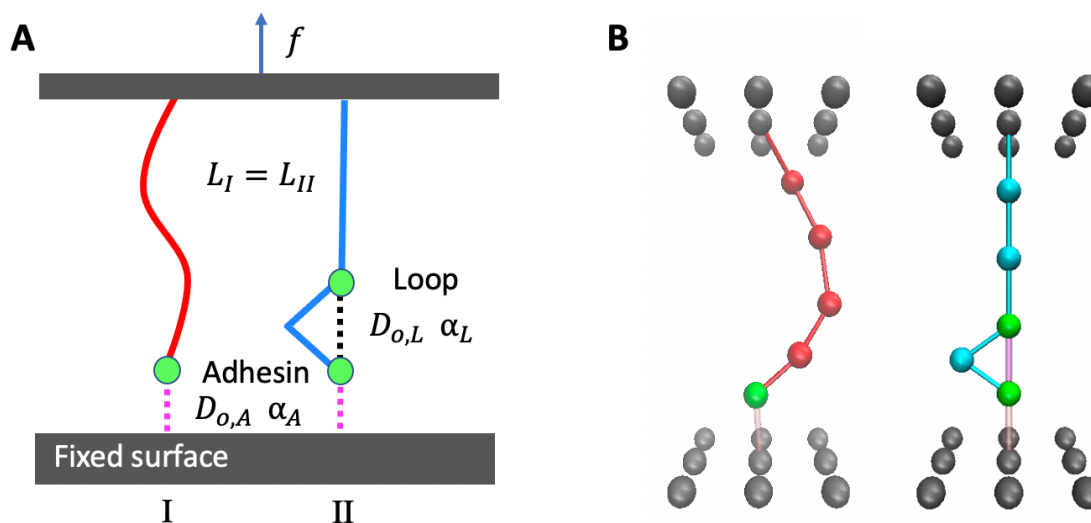


Figure 6-2 Two tether system A) Schematics of two surfaces interlinked by two tethers: looped and non-looped. Adhesive parts are represented with green circles. The adhesin and the loop interactions are represented with purple lines. B) Simulated looped tether.

to be inconsequential to our observations at the force levels studied. When a force is applied to pull two surfaces apart while remaining in a parallel arrangement, the shorter tether with the loop becomes taut and carries most of the load. Conceptually, there are two primary ways that the interface can fail. If the loop does not unfold, the short tether bears greater load and its lifetime is diminished, and its failure will most probably result sequential rupture of the adhesin interactions. Alternatively, if the loop does open, the load is shared, and the overall lifetime will be greatly extended as the adhesins will work together.

Whether sequential or coordinated failure occurs depends critically on the relative strength and stiffness of the adhesin and the loop interactions, or more generally, the energy landscape of these interactions. This is because these bonds are loaded in series and subject to the same force, and stiffness of the interaction dictates how much work is done on the bond, where mechanical work

reduces the energy barrier to separation and shortens the interaction lifetime. For instance, were these two interactions to have same bond energy or well depth, the stiffness of the bond would be lower for the interaction that has a greater distance to the transition state, in the context of the classical Arrhenius model. Sequential failure is the predominant failure mode if the tip of the folded chain detaches first, followed by the loose tether becoming taut and quickly rupturing as it carries the full load while the other chain remains folded. This would be the mode of failure if the loop interaction is too strong or too stiff relative to the adhesin, as little work is done on the bond when it is serially loaded with the softer, weaker adhesin bond. Conversely, coordinated failure should occur if the loop is much softer than the tip interaction, where the force does greater work on the loop, which will unfold to reveal its stored length, resulting in load sharing. This should yield prolonged lifetimes in coordinated failure compared to sequential failure. These failure mechanisms are schematically illustrated in Figure 6-3, showing also the load distribution between the tethers. It should be noted that the existence of these two failure mechanisms is analogous to low and high affinity states of proteins, or failure pathways of different resistance often described in phenomenological models of catch bonds. The central question that must be

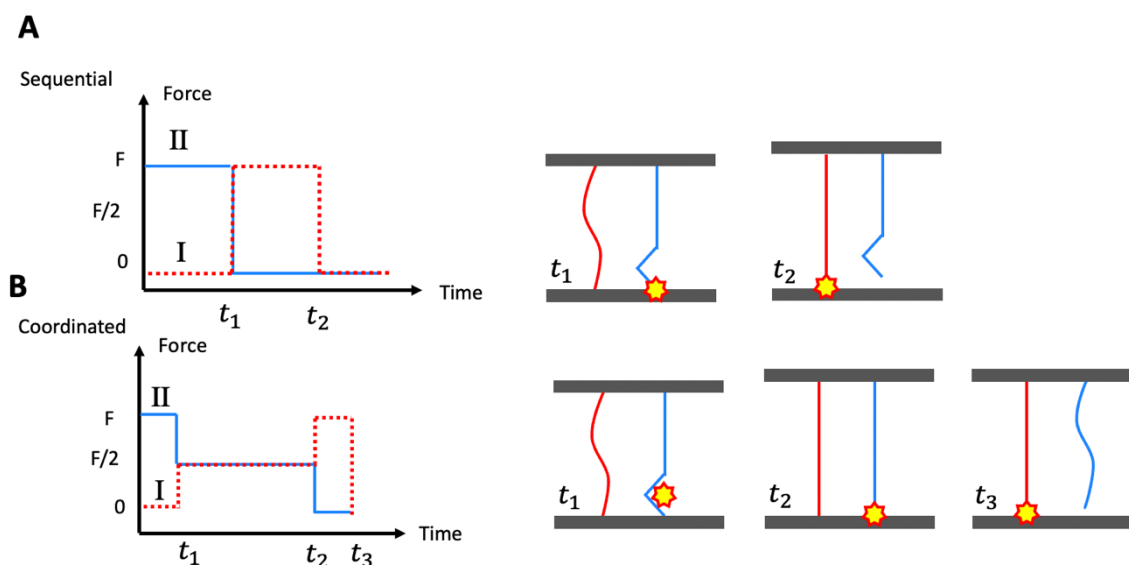


Figure 6-3 Force exposure of the individual tethers in A) sequential and B) coordinated failure scenarios. Solid line represents the looped and dashed line represents the non-looped tether. In sequential failure, t_1 and t_2 mark adhesin detachments. In coordinated failure, t_1 marks the unfolding of the loop, t_2 and t_3 mark adhesin detachments

addressed is how the energy landscapes should be designed to facilitate a transition from one failure mode to the other as the magnitude of the force increases.

To answer this question, we generically represent the energy landscape of the adhesin (E_A) and the loop interactions (E_L) with Morse potentials. In line with the two-state model representation of catch bonds (Section 3.2.1), the mean lifetime of the system $\langle \tau \rangle$ must increase when a tensile force is applied, which occurs if the force facilitates a propensity for the system to transition into the high-affinity state. At small forces, most trials should result in failure in the low-affinity state, which in this study corresponds to the sequential failure path. At large forces, most trials should result in transition to a high-affinity state, which in this study corresponds to the coordinated failure path, which hinges on the loop opening prior to adhesin bond failure. The mean lifetime under

coordinated failure $\langle\tau\rangle_C$ is also longer than the lifetime of the two-tether sequential system $\langle\tau\rangle_S$, in line with a two-state representation.

Following the same design path in Chapters 4 & 5, we determined that E_A should have a broader energy landscape than E_L . This is because the work done on the bond tilts the energy landscape, and the resulting reduction in the energy barrier (ΔE) is sensitive to the distance to the transition state, or the width of the landscape when well depth is kept constant. Therefore, ensuring that E_A has a lower α compared to E_L results in the ΔE of the folded interaction to be reduced greatly when the applied force is adequately large. According to Kramer's theory⁴³, $\langle\tau\rangle$ is directly proportional to $\exp[\Delta E]$, thus the loop lifetime declines more sharply when subjected to force compared to the adhesin lifetime. Based on this condition, we proposed the original parameters for E_A and E_L , which are listed in Table 6-1. As will be discussed later, a wide range of parameter combination that at a minimum satisfy the condition $\alpha_A > \alpha_L$ will result in catch bond-like characteristics, but the peak lifetime and the force at which it occurs will depend on all the parameters. The potentials are shown in Figure 6-4A, where it can be seen that the loop interaction has a deeper but broader energy well. Consequently, it can be predicted that its lifetime should be greater than the adhesin in the absence of force but should crossover and become shorter beyond a threshold force value. This should facilitate the transition to coordinated failure through loop opening at large forces.

Table 6-1. Tether interaction parameters

Interaction	D_o , kcal/mol	α , \AA^{-1}	x_o , \AA
Adhesin, E_A	1.2	10	2
Loop, E_S	2.8	2	2

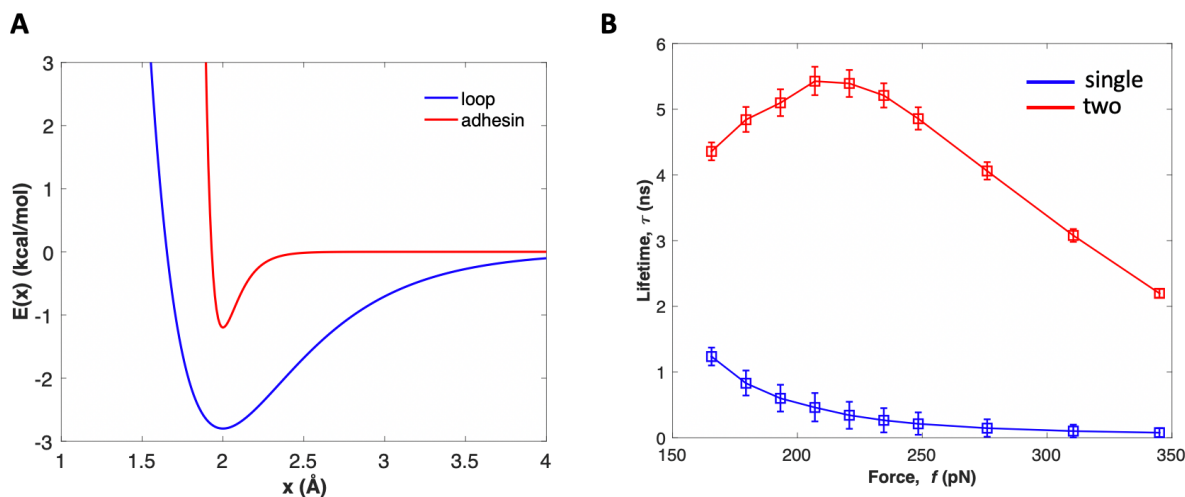


Figure 6-4 Energy landscape and lifetime graphs for the tether system A) Loop E_L and adhesin E_A energy landscapes are represented by Morse potential. B) Mean lifetime $\langle \tau \rangle$ versus force f curve for tether systems. Red line represents two tether system with one having loop and the blue line represents single tether system without a loop. Symbols are from MD simulations and solid line is the corresponding curve from the two state model. The error bars represent 95% confidence interval, derived by the bootstrapping method.

6.2 Simulation setup

MD simulations were run in the NVT ensemble at 50 K using a Langevin thermostat with a damping factor of 100 time steps. A lower temperature is used to reduce noise while ensuring thermal fluctuations give rise to stochastic bond breaking events. The adopted time step of 1 fs was found to be sufficiently small to ensure accuracy of the lifetime measurements. For tensile test simulations, force was applied after an equilibration of 50,000 time steps, which is adequate given the simple nature and small size of our systems. In each simulation, constant forces ranging from 160 to 380 pN is applied to the top plate and the interaction energies between the adhesins and the bottom plate are measured. Both surfaces are treated as rigid bodies that are constrained to move only in the direction normal to their planes. To obtain meaningful statistics for each force value,

10,000 trials were performed. The mass of the polymer beads and the plate beads are set as 1000 g/mol. The harmonic bond stiffness of tethers is 1000 kcal/molÅ² and each section has an equilibrium length of 2 Å.

6.3 Catch bond behavior

We performed molecular dynamics simulations with constant force applied to one of the surfaces while the other is held stationary. The force was ranged from 160 to 350 pN and the interface lifetime was recorded when both of the adhesion interactions were dissociated. The flexible polymer tethers consist of harmonic bond interactions with no angle terms.

To characterize the lifetime curves, we use the mean peak lifetime $\langle\tau\rangle_{peak}$ and corresponding critical force f_c . Figure 6-4B shows that $\langle\tau\rangle$ starts from ~ 4.3 ns and peaks at $f_c = 250$ pN with $\langle\tau\rangle_{peak} = 5.4$ ns. After the peak, $\langle\tau\rangle$ monotonically decreases at larger forces, exhibiting a transition to slip behavior. Also shown in Figure 3B is a single tether system, which exhibits the classical exponential decay across all force values. These results confirm catch bond behavior in our system. It should be noted that the temperature and the force ranges used in the simulations are arbitrary and do not aim to reproduce any particular experimental setup. Our goal here is to demonstrate the catch bond behavior in an artificial system, not to match any specific experimental data set.

Next, we explore how the lifetime curve characteristics depend on the molecular design parameters that determine the energy landscapes. Systematic variation of E_A and E_T parameters, specifically $D_{0,L}$, $D_{0,A}$, α_A , α_L reveals vast tunability of the lifetime curves with small changes in the parameter values. For interpreting these curves, we specify two quantities of interest, which is the value of the peak lifetime, τ^* , and the force at which it occurs, f^* . Here it should be noted that

in some of the curves the rise of the lifetime can be seen at small forces. This triphasic slip-catch-slip behavior is also seen in biological catch bonds. For the typical functions of catch bonds and our purposes τ^* is defined to be the maximum lifetime the interface takes after the initial slip regime, when it is present. Figure 6-5A demonstrates the effect of $D_{0,L}$, where it can be seen that increasing its value lowers τ^* and shifts f^* to the right. This means that overly stable and stiff loops will require a larger force to be opened, and that naturally causes a reduction in the lifetime at both low and high force levels. Figure 6-5B shows the impact of α_L when all other parameters are held constant. It is evidently clear that stiffer loops, even if not stronger, will lower τ^* and shift f^* to the right. Conversely, Figure 6-5C shows that increasing $D_{0,A}$ brings the whole lifetime curve up considerably, given the exponential dependence of the lifetimes on the adhesin strength. It is remarkable that τ^* increases without a major shift in f^* in this case. Increasing α_A has a similar effect, since stiffer adhesin interactions concentrate the work more greatly on the loops, triggering a transition to the coordinated failure more readily.

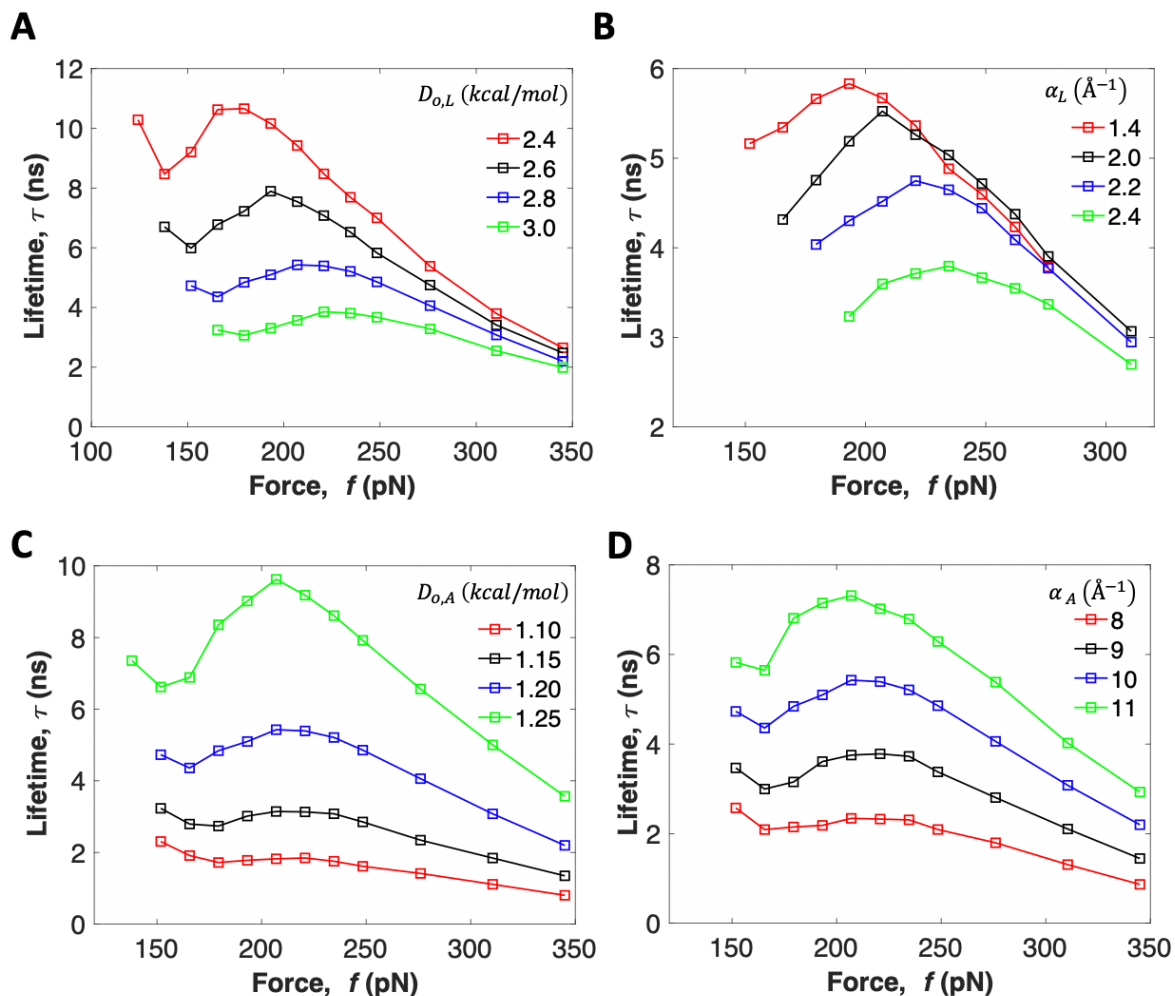


Figure 6-5 Effects of interaction parameters on mean lifetime versus force f curve of two tether system.

A) $D_{o,L}$ B) α_L C) $D_{o,A}$ D) α_A .

6.4 Estimating catch bond kinetics by an analytical model

With the aim of formulating general criteria for catch bond behavior beyond the sets of energy parameters tested in MD, we represent the lifetime of the system analytically using the kinetic theory. As we shown in Section 6.1, the system has two failure pathways: sequential or coordinated. Two dissociation events determine which failure pathway a single pulling trial will

follow, which are adhesion of the looped tether breaking and loop opening events. If looped tether adhesion breaks before loop opening, the load is not shared, and the system eventually fails sequentially under force. However, if loop opens before adhesion the load is shared between two tethers and the system will fail in coordinated fashion. Hence, the probability of adhesion breaking before loop opening, or vice versa, is crucial for the system lifetime. If we call average sequential lifetime as LT_S and average coordinated lifetime as LT_C , the average lifetime of the system will have a form of

$$LT = P(LT_S) + (1 - P)(LT_C) \quad (6-1)$$

Where P is the probability of adhesion breaking prior to loop opening and can be written as

$$P(A < L) = \int_0^{\infty} P(L > t | A = t) dt \quad (6-2)$$

Since both dissociation events are independent, Eqn. 6-2 can be simplified to

$$P(A < L) = \int_0^{\infty} P(L > t) P(A = t) dt \quad (6-3)$$

Based on Bell's theory, these adhesion breaking rate r_A and loop opening rate r_L have the following forms

$$\begin{aligned} r_A &= r_A^0 \exp(-F \Delta x_A) \\ r_L &= r_L^0 \exp(-F \Delta x_L) \end{aligned} \quad (6-4)$$

The probability that a loop exposed to a constant force f is still intact after a time t is given by

$$P(L > t) = \exp(-r_L t) \quad (6-5)$$

and using Kolmogorov forward equation we determine that $P(A = t)$ has a form of

$$P(A = t) = \frac{dF}{dt} = \frac{d}{dt} [1 - \exp(-r_A t)] = r_A \exp(-r_A t) \quad (6-6)$$

Plugging Eqn. 6-5 and 6-6, Eqn. 6-3 becomes

$$P(A < L) = \int_0^{\infty} r_A \exp(-(r_A + r_L)) dt = \frac{r_A}{r_L + r_A} \quad (6-7)$$

As seen in the Fig. 6-2, the sequential and coordinated failure events can be divided into 2 and 3 sub events respectively. Given that expected lifetime can be calculated using

$$LT = - \int_0^{\infty} \frac{dP}{dt} t dt, \quad (6-8)$$

sequential and coordinated lifetimes are calculated as

$$LT_S = \frac{1}{r_A(F)} + \frac{1}{r_A(F) + r_L(F)} \quad (6-9)$$

$$LT_C = \frac{1}{r_A(F) + r_L(F)} + \frac{1}{2r_A(F/2)} + \frac{1}{r_A(F)}$$

If we plug Eqn. 6-7 and Eqn. 6-9 in Eqn 6-1, we get

$$LT = \frac{r_A(F)}{r_A(F) + r_L(F)} \left(\frac{1}{r_A(F)} + \frac{1}{r_A(F) + r_L(F)} \right) + \frac{r_L(F)}{r_A(F) + r_L(F)} \left(\frac{1}{r_A(F) + r_L(F)} + \frac{1}{2r_A(F/2)} + \frac{1}{r_A(F)} \right) \quad (6-10)$$

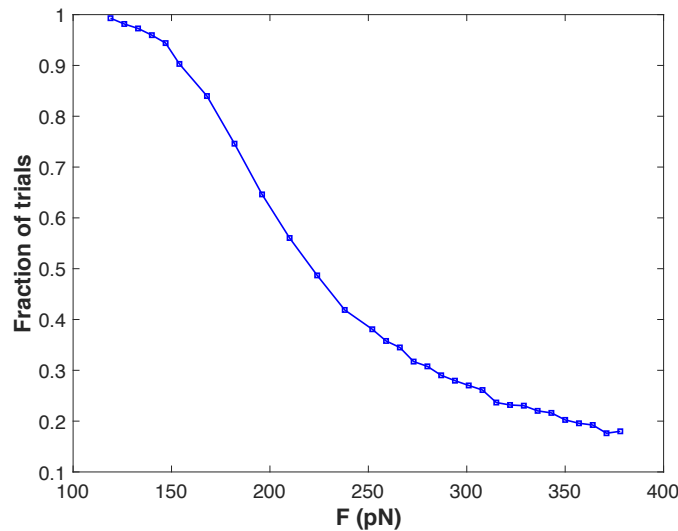


Figure 6-6 Force dependence of the fraction of trials for the looped tether adhesin breaking before the loop opening event. Each force value simulation is performed for 10,000 trials.

We will use Eqn. 6-10 to fit simulation data from Fig. 6-5. Figure 6-6 shows the fraction of trials, which looped tether adhesin breaks before loop opening. This graph corresponds to $P(A < L)$ and when we look at forces ranging from 100-150 pN, we saw that very small fraction of trials end with coordinated failure. Hence, around these force values overall lifetime in Eqn. 6-10 can be approximated as

$$LT = \frac{2}{r_A(F)}. \quad (6-11)$$

To obtain dissociation parameters r_A^0 and Δx_A for Eqn. 6-4, we will fit Eqn. 6-11 for simulation lifetime data for the range 100-150 pN. Then using probability curve in Fig. 6-6, we can fit Eqn. 6-7, to obtain r_L^0 and Δx_L . The fitting parameters are listed in Table 6-2. Based on these parameters we plot LT, LT_S, LT_C in Figure 6-7. Our model captures the catch bond behavior, i.e. there is an peak lifetime at 270 pN; however theoretical lifetime curve does not match with the simulation results. As seen in Fig. 6-7, the analytical equation underpredicts the coordinated lifetime (orange

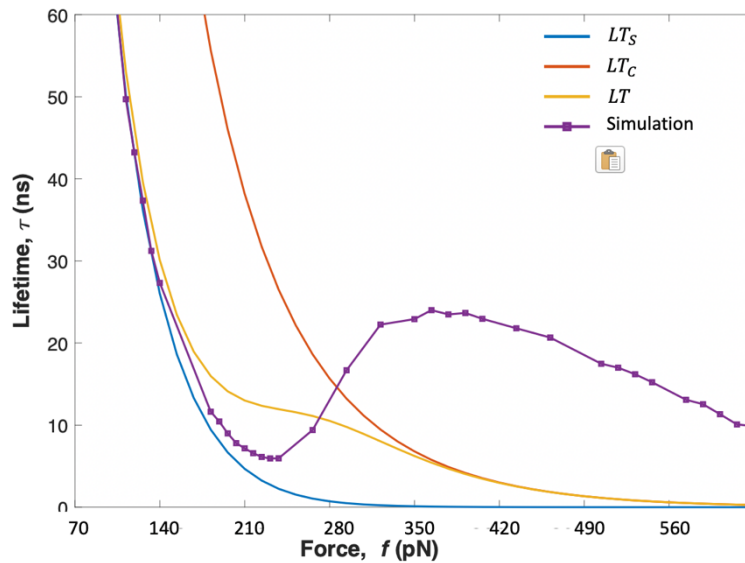


Figure 6-7 Analytical fit for tether lifetime data. Total, sequential and coordinated lifetime curves are plotted based on parameters in Table 6-2.

curve). We believe that the reason behind is the nonlinearity of the energy landscape or additional rebinding events that we have not considered in this iteration of the analytical model. In particular, the model does not account for adhesin rebinding to occur, and in the MD simulations a non-negligible number of cases do exhibit rebinding, which would explain the higher lifetimes observed at higher forces. Even though the analytical curve is not a match, it can still provide guidance to narrow down the parameter space for further simulations.

Table 6-2 Dissociation parameters from the analytical fit

Interaction	r^0 , (1/ns)	Δx , (pN/k _b T)
Loop	1.8×10^{-7}	6.72
Adhesin	5.95×10^{-4}	3.22

6.5 Conclusion

In conclusion, this work demonstrated a novel catch bond mechanism based on polymer tether grafted onto nanoparticles. Using molecular dynamics simulations, we generated reproducible lifetime curves reminiscent of highly complex catch bond proteins, networks of over 10,000 particles, with a minimalistic system that has only a few components. The essential feature of our system is the tailoring of the stiffness and strength of a loop in one of the tethers to achieve sequential vs. coordinated failure of the adhesive tethers, which facilitates a catch bond lifetime curve. Tuning the energy landscapes clearly revealed that a target peak lifetime can be programmed to occur at a given force level, which has major implications for mechanosensitive materials, nanocomposites, and drug delivery systems that could utilize mechanical cues for tailoring interfacial strength. While our design is unprecedented and distinct from biological catch

bonds, the lessons learned can also be used to study if catch bonds can occur through load-sharing and programmed unfolding of multiple adhesion proteins where soft fold and stiff ligand interactions might hold the key to achieving force enhanced lifetimes in diverse biomolecular systems.

Chapter 7 - Conclusion

Throughout this dissertation, I have presented a design procedure for nanocomposites with adhesin-inspired interfaces. In Chapter 3, we begin with investigating chaperone-usher (CU) pilus—a bacterial adhesive protein with catch bond properties. Based on previously developed biomechanical models of CU pili and their tip adhesins, we have presented MC simulations of the pilus response under constant velocity pulling and particle deceleration scenarios. We have highlighted the potential of CU pili with catch bond adhesin as molecular seat belt mechanisms. By outlining adhesin properties determined by previous experimental investigations, we modeled the protein and systematically vary its catch bond parameters to determine key adhesion properties. Based on these properties, in Chapter 4, we proposed design guidelines for reproducing the catch bond phenomenon in synthetic systems and created a tweezer-shaped mechanical design that mimicked protein ligand interaction and exhibited catch bond behavior reliably and predictably under thermal excitations.

Next, we adopted two strategies to implement catch bonds in nanocomposite systems: (i) in Chapter 5, by introducing allosteric pathways, we designed X-shaped nanoparticle that can change shape and transition to a stronger bond state in presence of tensile force, (ii) in Chapter 6, by grafting tethers with tunable lengths to the surface of nanoparticles, we created an interface with two failure modes: one where the load is shared among the tethers and the other where it is not. Both strategies present man-made alternatives to biological catch bond mechanisms and provides insight into how interfaces can be engineered to create nanoparticle networks with force-enhanced linkers.

7.1 Future outlook

The strategies investigated in this work should serve as a starting point for synthetic chemists aiming to design an actual synthetic option for catch bonds which can later be implemented in nanocomposites. Throughout the course of my graduate work, I focused on theory and simulation side of catch bond designs. However, I believe another the simulation work can be complemented by demonstration of our models as physical systems. One path to move forward can be to reproduce catch bond designs in macroscopic settings to qualify mechanical advantages we predict in the simulations. Physical system makes it possible to test hypotheses connecting geometry and binding lifetime, rapidly and conveniently. To best of our knowledge stochastic test of catch bonds in macroscale have never been considered experimentally before, thus there are no established protocols for these experiments. Random motion generator systems, i.e. shaking tables¹²² or granular systems^{123–125} in a highly accelerated container, might be the systems to simulate thermal noise. Morse interactions we defined can be recreated using panels with different patterns of magnetic dipoles that are capable of specific binding as shown in Niu *et al*¹²¹. Since the ratios of the different panel-binding energies are scale-invariant, this approach can, in principle, be applied down to the nanometer scale.

Another way one might go about creating various components of the nanoparticle similar to the structure in Chapter 5 is taking the versatile framework of DNA origami as an example. As shown in Figure 7-1, we highlight four main components of the nanoparticle: stiff members, hinges, switch and the interaction sites¹²⁶. Stiff members can be created from a bundle of interconnected double-stranded DNA helices organized in a honeycomb configuration. These

members can be connected from both ends by several flexible single-stranded DNA (ssDNA) scaffold connections arranged in a line to form the hinge rotation axis. Moreover, it has been shown in various DNA origami structures that ssDNA hinge can rotate flexibly over a range of angles¹⁰⁸.

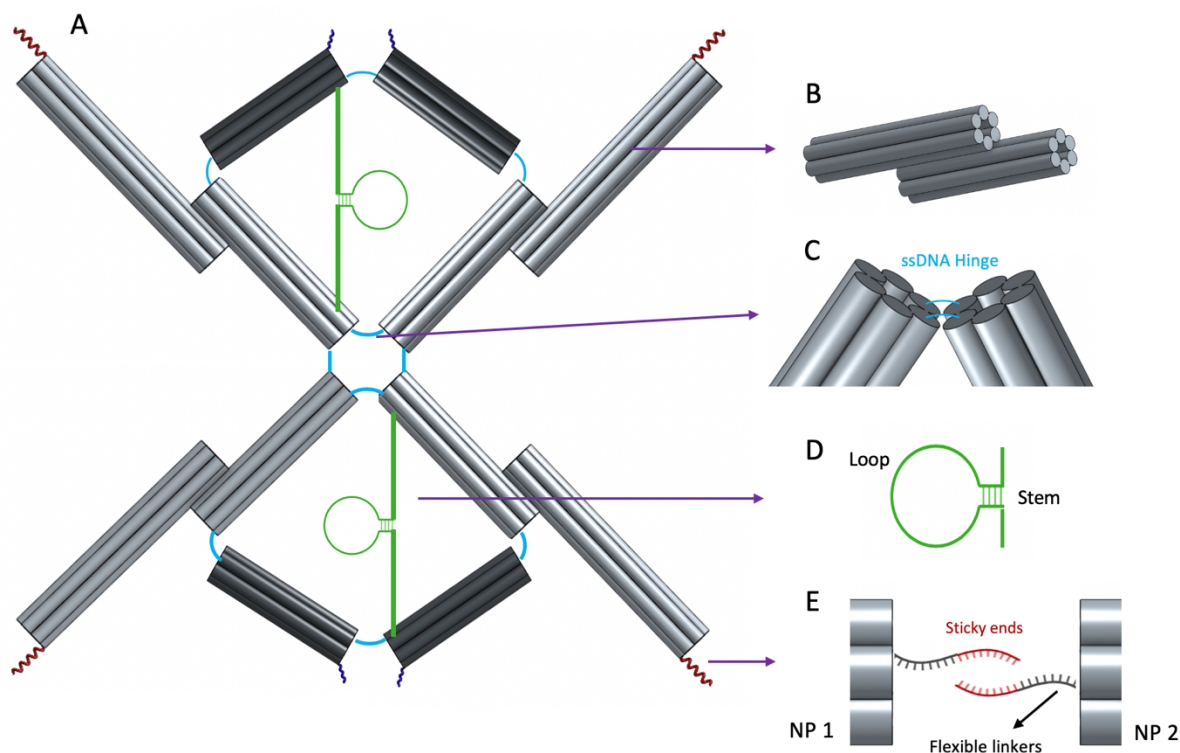


Figure 7-1 Possible DNA origami design of the X-shaped nanoparticle. A) Four main components of the nanoparticle are stiff members, hinges, switch and the interaction sites. These components can be created with B) double-stranded DNA helix bundles, C) single-strand DNA hinges, D) DNA hairpins, E) DNA overhangs with sticky ends.

We envision that novel materials based on this molecular mechanism can address trade-offs between strength and reconfiguration, two diametric material properties that are primarily governed by the strength of intermolecular interactions and may benefit from the biphasic behavior

of nanoparticles. The design approach we propose based on engineering the energy landscape should spur investigations into other shape-changing building blocks.

REFERENCES

1. Libonati, F., Nair, A. K., Vergani, L. & Buehler, M. J. Mechanics of collagen–hydroxyapatite model nanocomposites. *Mech. Res. Commun.* **58**, 17–23 (2014).
2. Zhu, H. *et al.* Anomalous scaling law of strength and toughness of cellulose nanopaper. *Proc. Natl. Acad. Sci.* **112**, 8971–8976 (2015).
3. Hu, K., Gupta, M. K., Kulkarni, D. D. & Tsukruk, V. V. Ultra-robust graphene oxide-silk fibroin nanocomposite membranes. *Adv. Mater.* **25**, 2301–2307 (2013).
4. Terrones, M. *et al.* Interphases in Graphene Polymer-based Nanocomposites: Achievements and Challenges. *Adv. Mater.* **23**, 5302–5310 (2011).
5. Madhukar, M. S. & Drzal, L. T. Fiber-Matrix Adhesion and Its Effect on Composite Mechanical Properties: IV. Mode I and Mode II Fracture Toughness of Graphite/Epoxy Composites. *J. Compos. Mater.* **26**, 936–968 (1992).
6. Linke, D. & Goldman, A. Bacterial Adhesion: Chemistry, Biology and Physics. *Adv. Exp. Med. Biol.* **715**, (2011).
7. Dembo, M., Torney, D. C., Saxman, K. & Hammer, D. The Reaction-Limited Kinetics of Membrane-to-Surface Adhesion and Detachment. *Proc. R. Soc. London. Ser. B. Biol. Sci.* **234**, 55–83 (1988).
8. Iyer, B. V. S. *et al.* Ductility, toughness and strain recovery in self-healing dual cross-linked nanoparticle networks studied by computer simulations. *Prog. Polym. Sci.* **40**, 121–137 (2014).
9. Iyer, B. V. S., Yashin, V. V. & Balazs, A. C. Harnessing biomimetic catch bonds to create

- mechanically robust nanoparticle networks. *Polym. (United Kingdom)* **69**, 310–320 (2015).
10. Zhang, T., Mbang, B. L., Yashin, V. V. & Balazs, A. C. Tailoring the mechanical properties of nanoparticle networks that encompass biomimetic catch bonds. *J. Polym. Sci. Part B Polym. Phys.* **56**, 105–118 (2018).
 11. Thomas, W. E., Trintchina, E., Forero, M., Vogel, V. & Sokurenko, E. V. Bacterial adhesion to target cells enhanced by shear force. *Cell* **109**, 913–923 (2002).
 12. Sarangapani, K. K. *et al.* Low Force Decelerates L-selectin Dissociation from P-selectin Glycoprotein Ligand-1 and Endoglycan. *J. Biol. Chem.* **279**, 2291–2298 (2004).
 13. Kong, F., García, A. J., Mould, A. P., Humphries, M. J. & Zhu, C. Demonstration of catch bonds between an integrin and its ligand. *J. Cell Biol.* **185**, 1275–1284 (2009).
 14. Buckley, C. D. *et al.* The minimal cadherin-catenin complex binds to actin filaments under force. **346**, (2014).
 15. Guo, B. & Guilford, W. H. Mechanics of actomyosin bonds in different nucleotide states are tuned to muscle contraction. *Proc. Natl. Acad. Sci.* **103**, 9844–9849 (2006).
 16. Sarangapani, K. K. & Asbury, C. L. Catch and release: How do kinetochores hook the right microtubules during mitosis? *Trends Genet.* **30**, 150–159 (2014).
 17. Rakshit, S. & Sivasankar, S. Biomechanics of cell adhesion: how force regulates the lifetime of adhesive bonds at the single molecule level. 2211–2223 (2014) doi:10.1039/c3cp53963f.
 18. McEver, R. P. & Zhu, C. Rolling Cell Adhesion. *Annu. Rev. Cell Dev. Biol.* **26**, 363–396 (2010).
 19. Chen, H. & Alexander-Katz, A. Polymer-based catch-bonds. *Biophys. J.* **100**, 174–182 (2011).

20. van Galen, M., van der Gucht, J. & Sprakel, J. Chemical Design Model for Emergent Synthetic Catch Bonds. *Front. Phys.* **8**, 361 (2020).
21. Dansuk, K. C. & Keten, S. Tunable seat belt behavior in nanocomposite interfaces inspired from bacterial adhesion pili. *Soft Matter* **14**, 1530–1539 (2018).
22. Mbanga, B. L., Iyer, B. V. S., Yashin, V. V. & Balazs, A. C. Tuning the Mechanical Properties of Polymer-Grafted Nanoparticle Networks through the Use of Biomimetic Catch Bonds. *Macromolecules* **49**, 1353–1361 (2016).
23. Chen, X., Mao, Z. & Chen, B. Probing time-dependent mechanical behaviors of catch bonds based on two-state models. *Sci. Rep.* **5**, 7868 (2015).
24. Konda, S. S. M. *et al.* Molecular catch bonds and the anti-hammond effect in polymer mechanochemistry. *J. Am. Chem. Soc.* **135**, 12722–12729 (2013).
25. Groote, R. *et al.* Strain-induced strengthening of the weakest link: The importance of intermediate geometry for the outcome of mechanochemical reactions. *Macromolecules* **47**, 1187–1192 (2014).
26. Thomas, W. E., Vogel, V. & Sokurenko, E. Biophysics of Catch Bonds. *Annu. Rev. Biophys.* **37**, 399–416 (2008).
27. Chakrabarti, S., Hinczewski, M. & Thirumalai, D. Phenomenological and microscopic theories for catch bonds. *J. Struct. Biol.* **197**, 50–56 (2017).
28. Barsegov, V. & Thirumalai, D. Dynamics of unbinding of cell adhesion molecules: Transition from catch to slip bonds. *Proc. Natl. Acad. Sci.* **102**, 1835–1839 (2005).
29. Thomas, W. *et al.* Catch-bond model derived from allostery explains force-activated bacterial adhesion. *Biophys. J.* **90**, 753–764 (2006).

30. Pereverzev, Y. V., Prezhdo, O. V., Forero, M., Sokurenko, E. V. & Thomas, W. E. The two-pathway model for the catch-slip transition in biological adhesion. *Biophys. J.* **89**, 1446–1454 (2005).
31. Bullerjahn, J. T. & Kroy, K. Analytical catch-slip bond model for arbitrary forces and loading rates. *Phys. Rev. E* **93**, 1–8 (2016).
32. Le Trong, I. *et al.* Structural Basis for Mechanical Force Regulation of the Adhesin FimH via Finger Trap-like β Sheet Twisting. *Cell* **141**, 645–655 (2010).
33. Sauer, M. M. *et al.* Catch-bond mechanism of the bacterial adhesin FimH. *Nat. Commun.* **7**, (2016).
34. Bartolo, D., Derényi, I. & Ajdari, A. Dynamic response of adhesion complexes: Beyond the single-path picture. *Phys. Rev. E - Stat. Physics, Plasmas, Fluids, Relat. Interdiscip. Top.* **65**, 4 (2002).
35. Isberg, R. R. & Barnes, P. Dancing with the host: Flow-dependent bacterial adhesion. *Cell* **110**, 1–4 (2002).
36. Lou, J. & Zhu, C. A Structure-Based Sliding-Rebinding Mechanism for Catch Bonds. **92**, (2007).
37. Pereverzev, Y. V. & Prezhdo, O. V. Force-induced deformations and stability of biological bonds. *Phys. Rev. E - Stat. Nonlinear, Soft Matter Phys.* **73**, 1–4 (2006).
38. Pereverzev, Y. V., Prezhdo, O. V. & Sokurenko, E. V. Allosteric role of the large-scale domain opening in biological catch-binding. *Phys. Rev. E - Stat. Nonlinear, Soft Matter Phys.* **79**, 1–7 (2009).
39. Chen, H. & Alexander-Katz, A. Polymer-based catch-bonds. *Biophys. J.* **100**, 174–182

- (2011).
40. Rubinstein, R. Y. *Simulation and the Monte Carlo Method*. (John Wiley & Sons, Inc., 1981).
 41. Metropolis, N., Rosenbluth, A. W., Rosenbluth, M. N., Teller, A. H. & Teller, E. Equation of State Calculations by Fast Computing Machines. *J. Chem. Phys.* **21**, 1087–1092 (1953).
 42. Bell, G. I. Models for the specific adhesion of cells to cells. *Science (80-.)*. **200**, 618–627 (1978).
 43. Kramers, H. A. Brownian Motion in a Field of Force and the Diffusion Model. 284–304 (1940).
 44. Evans, E. Probing the Relation Between Force—Lifetime—and Chemistry in Single Molecular Bonds. *Annu. Rev. Biophys. Biomol. Struct.* **30**, 105–128 (2001).
 45. Björnham, O., Axner, O. & Andersson, M. Modeling of the elongation and retraction of Escherichia coli P pili under strain by Monte Carlo simulations. *Eur. Biophys. J.* **37**, 381–391 (2008).
 46. Zakrisson, J., Wiklund, K., Axner, O. & Andersson, M. The Shaft of the Type 1 Fimbriae Regulates an External Force to Match the FimH Catch Bond. *Biophys. J.* **104**, 2137–2148.
 47. Tuckerman, M., Berne, B. J. & Martyna, G. J. Reversible multiple time scale molecular dynamics. *J. Chem. Phys.* **97**, 1990–2001 (1992).
 48. Frenkel, D. & Smit, B. Chapter 6 - Molecular Dynamics in Various Ensembles. in (eds. Frenkel, D. & Smit, B. B. T.-U. M. S. (Second E.) 139–163 (Academic Press, 2002). doi:<https://doi.org/10.1016/B978-012267351-1/50008-0>.
 49. Plimpton, S. & National, L. S. Fast Parallel Algorithms for Short-Range Molecular

- Dynamics. *J. Comput. Phys.* **117**, 1–42 (1995).
50. Phillips, J. C. *et al.* Scalable molecular dynamics with NAMD. *J. Comput. Chem.* **26**, 1781–1802 (2005).
 51. Berendsen, H. J. C., van der Spoel, D. & van Drunen, R. GROMACS: A message-passing parallel molecular dynamics implementation. *Comput. Phys. Commun.* **91**, 43–56 (1995).
 52. Mörters, P. & Peres, Y. *Brownian Motion. Cambridge Series in Statistical and Probabilistic Mathematics* (Cambridge University Press, 2010). doi:DOI: 10.1017/CBO9780511750489.
 53. Dünweg, B. & Paul, W. Brownian Dynamics Simulations Without Gaussian Random Numbers. *Int. J. Mod. Phys. C* **2**, 817–827 (1991).
 54. Grønbech-Jensen, N. & Farago, O. A simple and effective Verlet-type algorithm for simulating Langevin dynamics. *Mol. Phys.* **111**, 983–991 (2013).
 55. Park, S., Khalili-Araghi, F., Tajkhorshid, E. & Schulten, K. Free energy calculation from steered molecular dynamics simulations using Jarzynski's equality. *J. Chem. Phys.* **119**, 3559 (2003).
 56. Korea, C.-G., Ghigo, J.-M. & Beloin, C. The sweet connection: Solving the riddle of multiple sugar-binding fimbrial adhesins in *Escherichia coli*. *BioEssays* **33**, 300–311 (2011).
 57. Andersson, M., Fällman, E., Uhlin, B. E. & Axner, O. Dynamic Force Spectroscopy of *E. coli* P Pili. *Biophys. J.* **91**, 2717–2725.
 58. Epler Barbercheck, C. R., Bullitt, E. & Andersson, M. Bacterial adhesion pili. *Subcell. Biochem.* **87**, 1–18 (2018).
 59. Hahn, E. *et al.* Exploring the 3D molecular architecture of *Escherichia coli* type 1 pili. *J.*

- Mol. Biol.* **323**, 845–857 (2002).
60. Ehlers, S. & Klinth, J. Fast uncoiling kinetics of F1C pili expressed by uropathogenic *Escherichia coli* are revealed on a single pilus level using force-measuring optical tweezers. 305–316 (2011) doi:10.1007/s00249-010-0648-1.
 61. Björnham, O., Nilsson, H., Andersson, M. & Schedin, S. Physical properties of the specific PapG-galabiose binding in *E. coli* P pili-mediated adhesion. *Eur. Biophys. J.* **38**, 245–254 (2009).
 62. Forero, M., Yakovenko, O., Sokurenko, E. V., Thomas, W. E. & Vogel, V. Uncoiling mechanics of *Escherichia coli* type I fimbriae are optimized for catch bonds. *PLoS Biol.* **4**, 1509–1516 (2006).
 63. Aprikian, P. *et al.* The bacterial fimbrial tip acts as a mechanical force sensor. *PLoS Biol.* **9**, (2011).
 64. Miller, E., Garcia, T., Hultgren, S. & Oberhauser, A. F. The Mechanical Properties of *E. coli* Type 1 Pili Measured by Atomic Force Microscopy Techniques. *Biophys. J.* **91**, 3848–3856 (2006).
 65. Castelain, M. *et al.* Fast uncoiling kinetics of F1C pili expressed by uropathogenic *Escherichia coli* are revealed on a single pilus level using force-measuring optical tweezers. *Eur. Biophys. J.* **40**, 305–316 (2011).
 66. Andersson, M. *et al.* A Structural Basis for Sustained Bacterial Adhesion – Biomechanical Properties of CFA/I Pili. *J. Mol. Biol.* **415**, 918–928 (2012).
 67. Axner, O. *et al.* Unraveling the Secrets of Bacterial Adhesion Organelles Using Single-Molecule Force Spectroscopy. in *Single Molecule Spectroscopy in Chemistry, Physics and*

- Biology: Nobel Symposium* (eds. Gräslund, A., Rigler, R. & Widengren, J.) 337–362 (Springer Berlin Heidelberg, 2010). doi:10.1007/978-3-642-02597-6_18.
68. Fernandes, N. J., Koerner, H., Giannelis, E. P. & Vaia, R. A. Hairy nanoparticle assemblies as one-component functional polymer nanocomposites: opportunities and challenges. *MRS Commun.* **3**, 13–29 (2013).
 69. Schmitt, M. *et al.* Processing fragile matter: effect of polymer graft modification on the mechanical properties and processibility of (nano-) particulate solids. *Soft Matter* **12**, 3527–3537 (2016).
 70. Sun, J.-Y. *et al.* Highly stretchable and tough hydrogels. *Nature* **489**, 133–136 (2012).
 71. Zhang, T., Yuk, H., Lin, S., Parada, G. A. & Zhao, X. Tough and tunable adhesion of hydrogels: experiments and models. *Acta Mech. Sin.* **33**, 543–554 (2017).
 72. Yashima, E. *et al.* Supramolecular Helical Systems: Helical Assemblies of Small Molecules, Foldamers, and Polymers with Chiral Amplification and Their Functions. *Chem. Rev.* **116**, 13752–13990 (2016).
 73. Davis, D. A. *et al.* Force-induced activation of covalent bonds in mechanoresponsive polymeric materials. *Nature* **459**, 68–72 (2009).
 74. Tuncaboylu, D. C., Sari, M., Oppermann, W. & Okay, O. Tough and Self-Healing Hydrogels Formed via Hydrophobic Interactions. *Macromolecules* **44**, 4997–5005 (2011).
 75. Rose, S., Dizeux, A., Narita, T., Hourdet, D. & Marcellan, A. Time Dependence of Dissipative and Recovery Processes in Nanohybrid Hydrogels. *Macromolecules* **46**, 4095–4104 (2013).
 76. Dai, X. *et al.* A mechanically strong, highly stable, thermoplastic, and self-healable

- supramolecular polymer hydrogel. *Adv. Mater.* **27**, 3566–3571 (2015).
77. Björnham, O. & Axner, O. Multipili attachment of bacteria with helixlike pili exposed to stress. *J. Chem. Phys.* **130**, (2009).
 78. Whitfield, M., Ghose, T. & Thomas, W. Shear-stabilized rolling behavior of *E. coli* examined with simulations. *Biophys. J.* **99**, 2470–2478 (2010).
 79. Dansuk, K. C. & Keten, S. A Simple Mechanical Model for Synthetic Catch Bonds. *Matter* **1**, (2019).
 80. Thomas, W. Catch Bonds in Adhesion. *Annu. Rev. Biomed. Eng.* **10**, 39–57 (2008).
 81. Waldron, T. T. & Springer, T. A. Transmission of allostery through the lectin domain in selectin-mediated cell adhesion. *Proc. Natl. Acad. Sci. U. S. A.* **106**, 85–90 (2009).
 82. Adhikari, S., Moran, J., Weddle, C. & Hinczewski, M. Unraveling the mechanism of the cadherin-catenin-actin catch bond. *PLOS Comput. Biol.* **14**, e1006399 (2018).
 83. Thomas, W. E., Vogel, V. & Sokurenko, E. Biophysics of Catch Bonds. *Annu. Rev. Biophys.* **37**, 399–416 (2008).
 84. Adhikari, S., Moran, J., Weddle, C. & Hinczewski, M. Unraveling the mechanism of the cadherin-catenin-actin catch bond. *PLoS Comput. Biol.* **14**, 1–17 (2018).
 85. Hanggi, P., Talkner, P. & Borkovec, M. Reaction-rate theory : fifty years after Kramers. **62**, (1990).
 86. Evans, E. & Ritchie, K. Dynamic Strength of Molecular Adhesion Bonds. *Biophys. J.* **72**, 1541–1555 (1997).
 87. Dudko, O. K., Filippov, A. E., Klafter, J. & Urbakh, M. Beyond the conventional description of dynamic force spectroscopy of adhesion bonds. *Proc. Natl. Acad. Sci.* **100**,

- 11378–11381 (2003).
88. Dudko, O. K., Hummer, G. & Szabo, A. Intrinsic rates and activation free energies from single-molecule pulling experiments. *Phys. Rev. Lett.* **96**, 1–4 (2006).
 89. Mitchell, M. R., Tlusty, T. & Leibler, S. Strain analysis of protein structures and low dimensionality of mechanical allosteric couplings. (2016) doi:10.1073/pnas.1609462113.
 90. Rocks, J. W. *et al.* Designing allostery-inspired response in mechanical networks. **114**, 2520–2525 (2017).
 91. Flechsig, H. Design of elastic networks with evolutionary optimised long-range communication as mechanical models of allosteric proteins. 1–3 (2017).
 92. Yan, L., Ravasio, R., Brito, C. & Wyart, M. Architecture and coevolution of allosteric materials. *Proc. Natl. Acad. Sci. U. S. A.* **114**, 2526–2531 (2017).
 93. Yan, L., Ravasio, R., Brito, C. & Wyart, M. Principles for Optimal Cooperativity in Allosteric Materials. *Biophys. J.* **114**, 2787–2798 (2018).
 94. Bažant, Z. P. & Cedolin, L. *Stability of structures*. (Dover Publications Inc., 2003).
 95. Rogers, W. B., Shih, W. M. & Manoharan, V. N. Using DNA to program the self-assembly of colloidal nanoparticles and microparticles. *Nat. Rev. Mater.* **1**, (2016).
 96. Ke, Y., Ong, L. L., Shih, W. M. & Yin, P. Three-dimensional structures self-assembled from DNA bricks. *Science (80-.)*. **338**, 1177–1183 (2012).
 97. Douglas, S. M. *et al.* Self-assembly of DNA into nanoscale three-dimensional shapes. *Nature* **459**, 414–418 (2009).
 98. Creton, C. 50th Anniversary Perspective : Networks and Gels : Soft but Dynamic and Tough. 8297–8316 (2017) doi:10.1021/acs.macromol.7b01698.

99. Hoogenboom, R. Hard autonomous self-healing supramolecular materials—A contradiction in terms? *Angew. Chemie - Int. Ed.* **51**, 11942–11944 (2012).
100. Dansuk, K. C. & Keten, S. Self-strengthening biphasic nanoparticle assemblies with intrinsic catch bonds. *Nat. Commun.* **12**, 1–8 (2021).
101. Dansuk, K. C., Keten, S., Dansuk, K. C. & Keten, S. A Simple Mechanical Model for Synthetic Catch Bonds A Simple Mechanical Model for Synthetic Catch Bonds. *Matter* 1–15 doi:10.1016/j.matt.2019.06.005.
102. Dansuk, K. C., Keten, S., Dansuk, K. C. & Keten, S. A Simple Mechanical Model for Synthetic Catch Bonds A Simple Mechanical Model for Synthetic Catch Bonds. *Matter* 1–15 doi:10.1016/j.matt.2019.06.005.
103. Bell, G. I. Models for the specific adhesion of cells to cells. *Science (80-.)*. **200**, 618–627 (1978).
104. Evans, E., Leung, A., Heinrich, V. & Zhu, C. Mechanical switching and coupling between two dissociation pathways in a P-selectin adhesion bond. **101**, 11281–11286 (2004).
105. Yakovenko, O. *et al.* FimH forms catch bonds that are enhanced by mechanical force due to allosteric regulation. *J. Biol. Chem.* **283**, 11596–11605 (2008).
106. Evans, E. Probing the Relation Between Force—Lifetime—and Chemistry in Single Molecular Bonds. *Annu. Rev. Biophys. Biomol. Struct.* **30**, 105–128 (2001).
107. Youssef, M., Hueckel, T., Yi, G. R. & Sacanna, S. Shape-shifting colloids via stimulated dewetting. *Nat. Commun.* **7**, 1–7 (2016).
108. Marras, A. E., Zhou, L., Su, H. & Castro, C. E. Programmable motion of DNA origami mechanisms. **112**, 713–718 (2015).

109. Castro, Carlos E. and Su, Hai-Jun and Marras, Alexander E. and Zhou, L. & Johnson, J. Mechanical design of DNA nanostructures. *Nanoscale* **7**, 5913–5921 (2015).
110. Iyer, B. V. S., Yashin, V. V, Kowalewski, T., Matyjaszewski, K. & Balazs, a C. Strain recovery and self-healing in dual cross-linked nanoparticle networks. *Polym. Chem.* **4**, 4927–4939 (2013).
111. Kolmakov, G. V, Matyjaszewski, K. & Balazs, A. C. Harnessing Labile Bonds between Nanogel Particles to Create Self-Healing Materials. *ACS Nano* **3**, 885–892 (2009).
112. Iyer, B. V. S., Yashin, V. V & Balazs, A. C. Harnessing biomimetic catch bonds to create mechanically robust nanoparticle networks. *Polymer (Guildf)*. **69**, 310–320 (2015).
113. Qin, Z. & Buehler, M. J. Molecular Dynamics Simulation of the α -Helix to β -Sheet Transition in Coiled Protein Filaments : Evidence for a Critical Filament Length Scale. **198304**, 1–4 (2010).
114. Sun, L., Cheng, Q. H., Gao, H. J. & Zhang, Y. W. Effect of loading conditions on the dissociation behaviour of catch bond clusters. *J. R. Soc. Interface* **9**, 928–937 (2012).
115. Kellermayer, M. S. Z., Smith, S. B., Granzier, H. L. & Bustamante, C. Folding-unfolding transitions in single titin molecules characterized with laser tweezers. *Science (80-.)*. **276**, 1112–1116 (1997).
116. Chen, Y. J., Johnson, S., Mulligan, P., Spakowitz, A. J. & Phillips, R. Modulation of DNA loop lifetimes by the free energy of loop formation. *Proc. Natl. Acad. Sci. U. S. A.* **111**, 17396–17401 (2014).
117. Hyeon, C. & Thirumalai, D. Mechanical unfolding of RNA hairpins. *Proc. Natl. Acad. Sci. U. S. A.* **102**, 6789–6794 (2005).

118. Adhikari, R. & Makarov, D. E. Mechanochemical Kinetics in Elastomeric Polymer Networks : Heterogeneity of Local Forces Results in Nonexponential Kinetics. (2017) doi:10.1021/acs.jpcc.6b12758.
119. Cangialosi, A. *et al.* DNA sequence–directed shape change of photopatterned hydrogels via high-degree swelling. *Science (80-.)*. **357**, 1126–1130 (2017).
120. Chung, J., Kushner, A. M., Weisman, A. C. & Guan, Z. Direct correlation of single-molecule properties with bulk mechanical performance for the biomimetic design of polymers. *Nat. Mater.* **13**, 1055–1062 (2014).
121. Niu, R. *et al.* Magnetic handshake materials as a scale-invariant platform for programmed self-assembly. *Proc. Natl. Acad. Sci.* **116**, 24402–24407 (2019).
122. Reches, M., Snyder, P. W. & Whitesides, G. M. Folding of electrostatically charged beads-on-a-string as an experimental realization of a theoretical model in polymer science. *Proc. Natl. Acad. Sci.* **106**, 17644–17649 (2009).
123. Leconte, M. & Garrabos, Y. Collision statistics in a dilute granular gas fluidized by vibrations in low gravity Collision statistics in a dilute granular gas fluidized by vibrations in low gravity. (2006) doi:10.1209/epl/i2005-10589-8.
124. Goldhirsch, I. Apid ranular lows. (2003) doi:10.1146/annurev.fluid.35.101101.161114.
125. Aranson, I. S. Patterns and collective behavior in granular media : Theoretical concepts. **78**, 641–692 (2006).
126. Ban, E. & Picu, C. R. Strength of DNA Sticky End Links. (2014) doi:10.1021/bm401425k.